Supercavitating Vehicle Modeling and Dynamics for Control

A DISSERTATION
SUBMITTED TO THE FACULTY OF THE GRADUATE SCHOOL
OF THE UNIVERSITY OF MINNESOTA
BY

Hamid Mokhtarzadeh

IN PARTIAL FULFILLMENT OF THE REQUIREMENTS
FOR THE DEGREE OF
MASTERS OF SCIENCE

Gary Balas and
Roger Arndt, Advisers

May 2010

Contents

List of Tables

List of Figures

Chapter 1

Introduction

The speed of underwater vehicles is significantly limited due to the skin friction drag associated with traveling in water. A vehicle can be designed such that the nose of the vehicle creates a significant pressure drop and induces cavitation. Such a vehicle's nose feature is called the *cavitator*. At high enough speeds and with intelligent application of ventilation physics, the cavitator can induce a single elongated cavitation bubble, referred to as *supercavitation*, which can engulf the majority of the vehicle. The immediate benefit of supercavitation is the reduced contact area between the vehicle and the surrounding fluid. The reduced drag allows for very high speeds underwater, often exceeding 150 knots [1]. The cavitation number, σ is used to define the likelihood of cavitation to occur in a flow [2]. Supercavitation occurs at very low cavitation numbers, $\sigma < 0.1$. Onset of supercavitation changes the vehicle dynamics and introduces an interesting dynamics and control problem. During supercavitation, interaction between the vehicle and the cavity wall is referred to as planing. Planing typically occurs at the tail of the vehicle and complicates the dynamics of the vehicle as it travels.

This thesis presents a study of the dynamics and control challenges associated with a supercavitating vehicle. What separates this work from previous studies is the focus on control implications when modeling and analyzing the vehicle dynamics.

The linear dynamics of the vehicle in non-planing and planing conditions are analyzed. Comparisons of the effects of different cavitator shapes and fin geometries are conducted with special consideration to the control design implications. This basic intuitive understanding connecting the dynamics observed through simulation to the parameters of the physical vehicle can greatly simplify the design and execution of future vehicle control experiments.

The organization of this thesis is as follows:

- Chapter 1 introduces the supercavitating vehicle, and the benefits and challenges associated with supercavitation.
- Chapter 2 models the longitudinal dynamics of a supercavitating vehicle, including discussions of the various force and moment contributing components.
- Chapter 3 is organized into two sections. In the first section, the observed dynamics of the non-planing vehicle is analyzed. In the second section, the planing vehicle is analyzed and the dynamics linked back to the physical characteristics of the vehicle.
- Chapter 4 presents a trade-off study comparing planing to fins for supporting the aft end of the vehicle as well as discussions of fin geometry. A comparison is also conducted comparing different cavitator shapes and their affect on the vehicle dynamics.
- Chapter 5 presents a final discussion of the analyses presented in the thesis as well as recommendations for future research.

1.1 Purpose of each Model

A series of nonlinear and linear models will be presented and utilized for different purposes in this thesis. The following is a short description of the various models and their purpose.

1.1.1 Nonlinear Two State Model

Chapter 2 presents a derivation of a nonlinear two state (α, q) longitudinal model for a supercavitating vehicle. Expressions for each of the model's terms are derived, thus providing a closed form nonlinear expression for the model. The closed form expression is important because subsequent simplified and linear models are obtained symbolically, in terms of the various vehicle and environmental parameters. Among the goals of this thesis is to connect the observed dynamics to the physical characteristics of the vehicle. The closed form two state nonlinear model is mathematically complex, thus masking any insight connecting the model dynamics to the parameters of the physical vehicle. This is overcome by simplifying the nonlinear expressions through applying small angle approximations and other assumptions when appropriate. Subsequent to deriving the nonlinear force and moment expressions for the vehicle hydrodynamic components, the simplified nonlinear force and moment expressions are also presented. Modeling the vehicle environment also requires simplified closed form expressions which will later be embedded within the symbolic linear models. The primary example of this is the expression for the vehicle planing immersion depth $\frac{h}{D_{body}}$. A polynomial approximation for the immersion depth as a function of the vehicle states is presented in Section 2.4.4. This allows for the symbolic linear planing model to include the dynamics of the changing immersion depth. Using a more accurate and complicated planing depth algorithm would not lend itself for symbolic linearization.

The two state nonlinear model with simplified force and moment expressions is used for the symbolic linearization.

1.1.2 Linear Two State Model

The nonlinear two state model with simplified force, moment, and planing immersion expressions is used for symbolic linearization. The non-planing and planing linear models of the vehicle are presented symbolically in Section 2.8 and Section 2.9, respectively. The symbolic linear models are later computed at specific vehicle trim conditions, resulting in numerical non-planing and planing linear models. The symbolic linear models provide the opportunity to find the source of a specific observed dynamic behavior of a linear model at a specific trim condition.

The nonlinear and linear two state model are the models derived and analyzed in the main body of this thesis. A more complicated six degree of freedom model was also used for validation purposes, and is presented in the appendix for reference only.

1.1.3 Nonlinear Six State Model

The appendix includes a derivation of a six degree of freedom nonlinear model. This model is derived in a modular fashion for implementation in Simulink software, and contains more accurate environmental models. For example, the cavity time delay is accounted for and more complex algorithms are used to detect planing. This nonlinear model was used to check the two state nonlinear and the resulting linear models. The complexity of the model makes it difficult to connect the observed dynamics to the vehicle physical characteristics, nevertheless this model was instrumental in verifying the derived nonlinear and linear models.

1.2 Notation and Units

Many variables, subscripts, and occasionally superscripts are used to express the various vehicle states, geometries, and reference frames. A genuine effort is made to preserve common variable notations as well as coherent choices for variable names. Section 1.2 defines the majority of variables used throughout this thesis and can be referenced to clarify notation. Subscripts and superscripts are used to further specify the meaning of a variable. In general, superscripts specify the coordinate frame in which the variable is expressed. For example, F_c^{body} is the force vector of the cavitator expressed in the vehicle body frame. Subscripts specify the specific source of the variable. For example, subscripts of c and p specify the cavitator and planing as sources of the specific variable. Furthermore, subscripts on subscripts, for example the x in $Force_{p_x}$, further specify a specific component of the force vector. Any additional variables are defined upon being used for the first time within the thesis.

List of Symbols

A	Area defined for nondimensionalizing coefficients	(m^2)
C_D, C_L	Drag and Lift coefficient	
cg	Center of gravity	
cp	Center of pressure	
D, L	Drag and Lift	(N)
D_{body}	Vehicle diameter	(m)
d_c	Disk cavitator diameter	(m)
d_m	Cavity maximum diameter	(m)
DCM_{ij}	Transformation matrix from $j-frame$ to $i-frame$	
g	Gravitational acceleration	(m/s^2)
h	Immersion depth of vehicle tail when planing	(m)
I_{xx}, I_{yy}, I_{zz}	Moments of inertia	(kgm^2)
L	Vehicle length	(m)
L_{cavity}	Cavity length	(m)
l_c	Distance from vehicle cg to cavitator cp	(m)
l_p	Distance from vehicle cg to planing cp	(m)
p, q, r	Vehicle angular rates	(rad/s)
$\bar{q}$	Dynamic pressure $1/2\rho V^2$	(Pa)
T_x, T_z	Thrust vector x_b and z_b components	(N)
u, v, w	Vehicle velocity components expressed in body frame	(m/s)
V	Vehicle Speed	(m/s)
X, Y, Z	Inertial coordinates	(m)
x_b, y_b, z_b	Body reference frame coordinates	(m)
x_c, y_c, z_c	Cavitator reference frame coordinates	(m)
x_p, y_p, z_p	Planing reference frame coordinates	(m)
ψ, θ, ϕ	Yaw, pitch, roll, Vehicle Euler angles	(rad)
δ_c	Cavitator deflection angle	(rad)
σ	Cavitation number	
$\omega_x, \omega_y, \omega_z$	Vehicle angular rates	(rad/s)

Chapter 2

Longitudinal Modeling

The equations of motion of a supercavitating vehicle can be derived from Newton's second law of motion, which can be expressed in vector form as

$$\bar{F} = m(\frac{d}{dt}\bar{v}_{cg} + \omega \times \bar{v}_{cg}) \tag{2.1}$$

and

$$\bar{M}_G = \frac{d}{dt}\bar{H}_G + \omega \times \bar{H}_G \tag{2.2}$$

where $\bar{H}_G$ is angular momentum and both equations are written about the vehicle body frame, or *b-frame*. An overview of the coordinate system used is shown in Figure 2.1. There are several assumptions which simplify the derivation:

1. The *b-frame* is selected as the principal axes of the vehicle. Thus the off diagonal inertia terms (I_{xy}, I_{yz}, I_{zx}) are assumed to be zero.

2. The vehicle is a rigid body and thus any hydroelasticity effects are neglected. Note that in higher fidelity modeling of supercavitating vehicles, the hydroelas-

tic effects may be important because of the long and slender vehicle structure.

3. The mass of the vehicle remains constant. The vehicle's changing mass throughout its operational cycle can have a considerable effect on the dynamics. The goal of the current modeling effort is understanding short term dynamics under supercavitating conditions, and thus the constant mass assumption can be safely applied.

4. The earth is taken as an inertial reference.

The vector form of Newton's equations can be expanded into individual linear and rotational components. The resulting complete equations of motion for a supercavitating vehicle are given as

$$\begin{aligned} \sum F_x &= m(\dot{v}_x + v_z\omega_y - v_y\omega_z) \\ \sum F_y &= m(\dot{v}_y + v_x\omega_z - v_z\omega_x) \\ \sum F_z &= m(\dot{v}_z + v_y\omega_x - v_x\omega_y) \end{aligned} \tag{2.3}$$

$$\begin{aligned} \sum M_x &= I_{xx}\alpha_x - (I_{yy} - I_{zz})\omega_y\omega_z \\ \sum M_y &= I_{yy}\alpha_y - (I_{zz} - I_{xx})\omega_x\omega_z \\ \sum M_z &= I_{zz}\alpha_z - (I_{xx} - I_{yy})\omega_x\omega_y \end{aligned} \tag{2.4}$$

The six degree of freedom Equations (2.3) and (2.4) are paired down to a tractable longitudinal model with only two states: angle of attack (α) and pitch rate (q). This approach allows for better physical insight into the vehicle dynamics. Restricting the vehicle to the longitudinal plane, the following equations remain

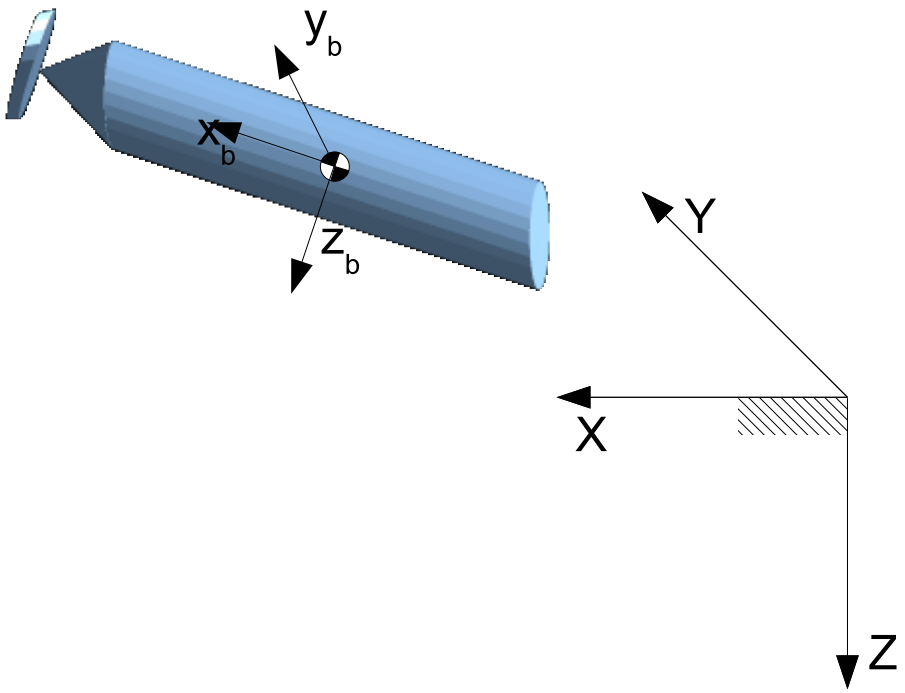

Figure 2.1: Inertial frame is denoted by capital letters (X, Y, Z) and the body-fixed coordinate system (*b-frame*) is denoted by lower case letters (x_b, y_b, z_b). Other general coordinate systems will also use lower case letters and be further identified by their subscripts.

$$\begin{aligned} \sum F_x &= m(\dot{v}_x + v_z\omega_y) \\ \sum F_z &= m(\dot{v}_z - v_x\omega_y) \\ \sum M_y &= I_{yy}\alpha_y \end{aligned} \tag{2.5}$$

The vehicle dynamics depend on the forces and moments acting on the vehicle. There exist forces and moments that depend on the condition of the vehicle with respect to the cavity. The primary example of this dependence is planing. When the vehicle is entirely within the cavity, no force and moment contribution is imparted by planing. There is an important contribution to the vehicle dynamics from planing when the tail of the vehicle is impinging on the wall of the cavity. The switching between planing and non-planing conditions must be accounted for in the vehicle's final equations of motion. This is accomplished by initially writing the equations of motion to include all possible force and moment terms for the chosen vehicle configuration. Then the specific equations of motion for the non-planing and planing conditions are obtained by only retaining the relevant force and moment terms for each condition. Prior to deriving the force and moment equations, a vehicle configuration is identified.

2.1 Vehicle Configuration

The physical configuration of a supercavitating vehicle depends greatly on the mission objectives. Requirements relating to launch, homing, drag reduction, and other factors all play into the decision. An optimal configuration for the supercavitating phase of the mission may turn out to be a detriment to the performance of the vehicle during the fully wetted phase. The focus of this thesis is only the supercavitating

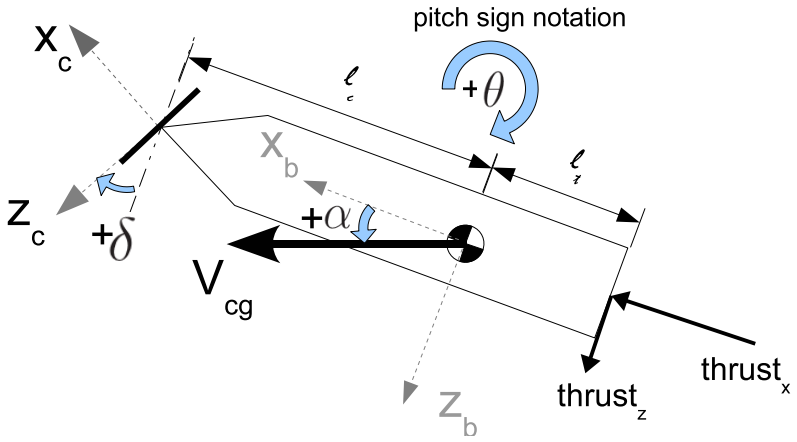

Figure 2.2: Diagram of longitudinal body and relevant notation - note positive vehicle angle of attack α is defined opposite the positive vehicle pitch angle θ direction

Vehicle Parameters

Name	Description	Value
L	vehicle length	2.066 m
D_{body}	vehicle diameter	0.1016 m
l_c	distance from vehicle CG to cavitator	1.1223 m
l_t	distance from vehicle CG to tail of vehicle	0.9437 m
m	mass of vehicle	22 kg
I_{yy}	moment of inertia	5.1847 kg m^2
d_c	disk cavitator diameter	0.0381 m
ρ	density of water	1000 kg/m^3
g	gravitational acceleration	9.8 m/s^2
σ	cavitation number	0.029

Table 2.1: List of the vehicle parameters [3]

condition and a simple vehicle configuration is chosen for the analysis. The nominal vehicle has a cylindrical body with a conical nose and a disk cavitator mounted on the nose of the vehicle. There are no fins, but instead thrust vectoring is assumed at the tail to support the aft end of the vehicle enabling the vehicle to maintain a non-planing flight condition. The chosen vehicle configuration along with the sign notation is depicted in Figure 2.2 and the physical properties of the vehicle are listed in Table 2.1. The physical properties used in this thesis are taken from [3], primarily for purposes of comparison. Studying the trade-offs between the various physical parameters for a supercavitating vehicle is important but beyond the scope of this thesis.

2.2 Two State (α,q) Model

There are four contributions which make up the total forces and moments imparted to the vehicle for the selected configuration. These are the cavitator, planing, thrust, and gravity. Equation (2.5) can be rearranged with each force and moment contribution identified as follows

$$\dot{u} = \frac{1}{m}\left(F_{c_x} + F_{p_x} + F_{T_x} + F_{g_x}\right) - w\,q \tag{2.6}$$

$$\dot{w} = \frac{1}{m}\left(F_{c_z} + F_{p_z} + F_{T_z} + F_{g_z}\right) + u\,q \tag{2.7}$$

$$\dot{q} = \frac{1}{I_{yy}}\left(M_{c_y} + M_{p_y} + M_{T_y}\right) \tag{2.8}$$

The subscripts c, p, T, and g correspond to the cavitator, planing, thrust, and gravity contributions respectively. Assuming that the $x-body$ velocity is constant and applying a small angle approximation, the vehicle angle of attack can be introduced to reduce the model to two states. Namely, $\dot{\alpha} \approx \frac{\dot{w}}{u}$ and thus the following two equations

remain

$$\dot{\alpha} = \frac{1}{u\,m}\left(F_{c_z} + F_{p_z} + F_{T_z} + F_{g_z}\right) + q \tag{2.9}$$

$$\dot{q} = \frac{1}{I_{yy}}\left(M_{c_y} + M_{p_y} + M_{T_y}\right) \tag{2.10}$$

Expressions for the forces and moments imparted by the cavitator, planing, gravity, and thrust must be obtained. A close look at both the cavitator and planing will reveal the dependence of their respective characteristics on the vehicle state.

2.3 Disk Cavitator

The forces and moments imparted by a disk cavitator at the nose of the vehicle depend on both the angle of attack of the cavitator as well as the cavitation number. In [4] the equations for lift, drag, and moment coefficients of a disk cavitator are given as

$$\begin{aligned} C_{Dc}(\sigma,\alpha_c) &= \frac{D_c(\sigma,\alpha_c)}{1/2\rho V^2 A_c} \approx C_{D0}(1+\sigma)cos^2\alpha_c \\ C_{Lc}(\sigma,\alpha_c) &= \frac{L_c(\sigma,\alpha_c)}{1/2\rho V^2 A_c} \approx C_{D0}(1+\sigma)cos\alpha_c sin\alpha_c \\ C_{Mc}(\sigma,\alpha_c) &= \frac{M_c(\sigma,\alpha_c)}{1/2\rho V^2 d_c A_c} \approx 0 \end{aligned} \tag{2.11}$$

where D_c and L_c are the drag and lift forces acting on the cavitator, M_c is the hydrodynamic moment, $A_c = \pi d_c^2/4$ is the disk area, and α_c is the cavitator angle of attack. C_{D0} is the drag coefficient at zero angle of attack and cavitation number, and is taken as approximately 0.805 based on empirical data [5]. Equations (2.11) are utilized by [4] to approximate the experimental results of [6], which is a very complete study of the forces and moments imparted by various cavitator shapes as a function

of angle of attack and cavitation number. Since supercavitation occurs at relatively low cavitation numbers ($\sigma < 0.1$), the dependence of the disk cavitator forces and moments on any fluctuation in a low cavitation number is very small.

Utilizing Equation (2.11) to approximate the forces and moments on a disk cavitator implies the following:

- The magnitude of the force vector acting on the cavitator is proportional to $C_{D0}(1+\sigma)cos\alpha_c$
- The force vector acting on the cavitator is always oriented normal to the cavitator, assuming there is little or no pitch rate on the vehicle. This is seen because the lift and drag coefficient expressions differ only by $sin\alpha_c$ and $cos\alpha_c$
- In the case that the cavitator is fixed perpendicular to the vehicle ($\delta_c = 0$), as the vehicle angle of attack changes there will be little or no force induced moment from the cavitator on the vehicle. This is because the cavitator force vector is oriented normal to the cavitator and any substantial change in force induced moment would only arise from cavitator actuation. The possibility of a small force induced moment would arise if the cavitator angle of attack differed from the vehicle angle of attack, for example as a result of the vehicle pitch rate.

The notion that the cavitator force vector is oriented normal to the cavitator can be derived from the following statement in [6]:

> *"In the case of the disc the ratio of lift coefficient to drag coefficient is found to be almost exactly equal to the tangent of the [cavitator] angle of attack, therefore tangential friction forces are negligible as compared to the normal pressure forces."*

It will later be shown that this distinction plays an important role in defining the static stability properties of the vehicle.

Rather than using Equation (2.11) to approximate the cavitator forces and moments, the hydrodynamic data for a disk cavitator collected in [6] was digitized and can be seen in Figure 2.3 and Figure 2.4. Notice that this range of cavitation numbers has little effect on the lift coefficient. In the case of a non-linear simulation, the data can be used in a lookup table to determine the hydrodynamic coefficients of the cavitator. A closed-form expression for the hydrodynamic coefficients is derived for later use in the linear simulation. The hydrodynamic data can be fit with a polynomial of sufficient order to capture the data with sufficient accuracy.

The fitting approach was applied to both the lift and drag coefficients of the cavitator. Assuming a constant cavitation number, the resulting polynomial approximations are

$$C_{Dc} \approx -k_2\alpha_c^2 + k_1 \tag{2.12}$$

$$C_{Lc} \approx -k_3\alpha_c \tag{2.13}$$

$$C_{Mc} \approx k_4\alpha_c \tag{2.14}$$

where k_1, k_2, k_3 and $k_4 > 0$. For $\sigma = 0.08$, then $k_1 = 0.875$, $k_2 = 0.0002(180/\pi)^2$, $k_3 = 0.0126(180/\pi)$, and $k_4 = 0$ for the disk cavitator. Note that α_c is the angle of attack of the cavitator (different from the vehicle angle of attack) and is in units of radians.

2.3.1 Nonlinear Expression

The force and moment nonlinear expressions for the cavitator are next derived. This requires determining the velocity and angle of attack at the nose of the vehicle, where the cavitator center of pressure (*cp*) is located. The cavitator angle of attack is then

CL	cavitation number σ			
angle of attack α (deg)	0.08	0.1	0.12	0.14
-30	0.363	0.369	0.373	0.380
-20	0.264	0.268	0.271	0.275
-10	0.140	0.143	0.145	0.148
-5	0.071	0.073	0.074	0.075
0	0.000	0.000	0.000	0.000
5	-0.071	-0.073	-0.074	-0.075
10	-0.140	-0.143	-0.145	-0.148
20	-0.264	-0.268	-0.271	-0.275
30	-0.363	-0.369	-0.373	-0.380

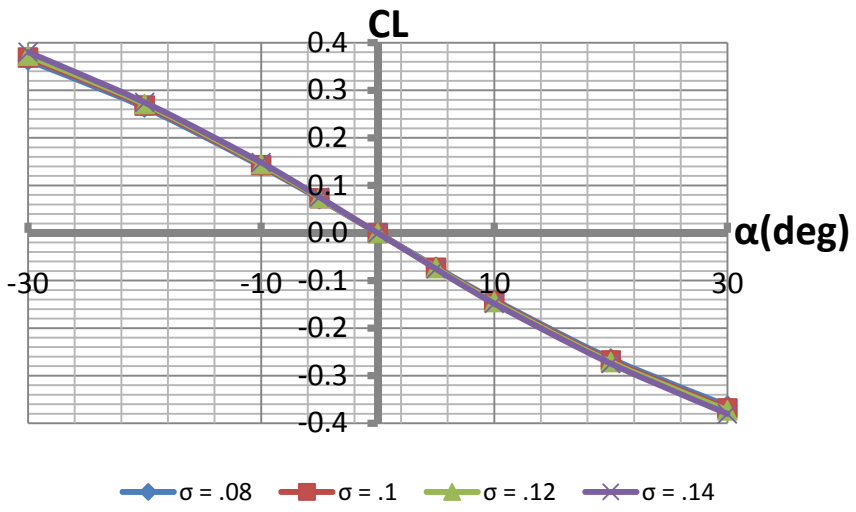

Figure 2.3: Table and plot of disk cavitator lift coefficient as function of cavitator angle of attack for various cavitation numbers based on [6]

CD	cavitation number σ		
angle of attack α (deg)	0.08	0.1	0.12
-30	0.659	0.670	0.682
-20	0.783	0.797	0.811
-10	0.848	0.864	0.881
-5	0.866	0.884	0.901
0	0.875	0.891	0.908
5	0.866	0.884	0.901
10	0.848	0.864	0.881
20	0.783	0.797	0.811
30	0.659	0.670	0.682

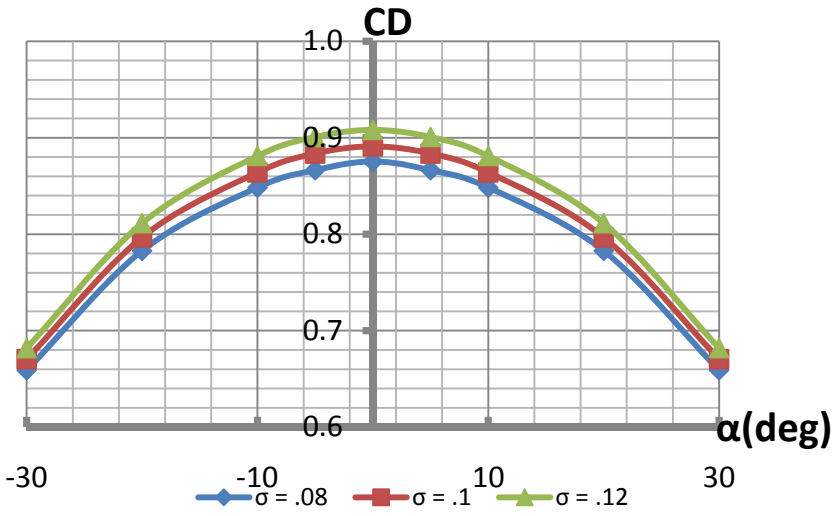

Figure 2.4: Table and plot of disk cavitator drag coefficient as function of cavitator angle of attack for various cavitation numbers based on [6]

used to lookup the corresponding hydrodynamic lift and drag coefficients, and the cavitator velocity vector is used to determine the magnitude and direction of the lift and drag. The lift and drag vectors are transformed and expressed in the vehicle body frame and the force induced moment is also calculated. These are the general steps that are followed, not only in the case of the cavitator but also in the case of planing whose force and moment expressions are derived in Section 2.4.1.

The following variables define the vehicle velocity and angular velocity vector, the position vector from the center of gravity (cg) to the cavitator cp, and the transformation matrix from body to cavitator frame.

$$\begin{aligned}
\bar{V}_{cg} =& [u, 0, w]^T \\
\omega =& [0, q, 0]^T \\
\bar{r}_{cg\rightarrow cp} =& [l_c, 0, 0]^T \\
DCM_{cb} =& \begin{bmatrix} cos(\delta_c) & 0 & -sin(\delta_c) \\ 0 & 1 & 0 \\ sin(\delta_c) & 0 & cos(\delta_c) \end{bmatrix}
\end{aligned}$$

Here l_c is the distance from the vehicle cg to the disk cavitator pivot which is assumed to be the cavitator cp. The superscript "T" is used to denote the matrix transpose. As shown in Figure 2.2, an intermediate local cavitator frame will be used in the derivation of the forces and moments of the disk cavitator expressed in the body frame. Since the cavitator hydrodynamic coefficients are known as a function of the angle of attack at the cavitator, the first step is to determine the local conditions at the cavitator and express them in the local frame. The velocity at the cavitator is

determined as

$$\begin{aligned}
\bar{V}_{cp}^{local} =& DCM_{cb}[\bar{V}_{cg} + \omega \times \bar{r}_{cg\to cp}] \\
=& DCM_{cb}\left\{ \begin{bmatrix} u \\ 0 \\ w \end{bmatrix} + \begin{bmatrix} 0 \\ q \\ 0 \end{bmatrix} \times \begin{bmatrix} l_c \\ 0 \\ 0 \end{bmatrix} \right\} \\
=& \begin{bmatrix} cos(\delta_c) & 0 & -sin(\delta_c) \\ 0 & 1 & 0 \\ sin(\delta_c) & 0 & cos(\delta_c) \end{bmatrix} \begin{bmatrix} u \\ 0 \\ w - l_c q \end{bmatrix} \\
=& \begin{bmatrix} ucos(\delta_c) - (w - l_c q)sin(\delta_c) \\ 0 \\ usin(\delta_c) + (w - l_c q)cos(\delta_c) \end{bmatrix} \equiv \begin{bmatrix} u_c \\ 0 \\ w_c \end{bmatrix}
\end{aligned}$$

Using the definition of angle of attack, the local angle of attack (α_c) of the cavitator and the local speed (V_c) can be determined

$$\begin{aligned}
\alpha_c &= tan^{-1}\left(\frac{w_c}{u_c}\right) \\
&= tan^{-1}\left(\frac{usin(\delta_c) + (w - l_c q)cos(\delta_c)}{ucos(\delta_c) - (w - l_c q)sin(\delta_c)}\right) \qquad (2.15) \\
V_c &= \sqrt{u_c^2 + w_c^2} \qquad (2.16)
\end{aligned}$$

The C_{Dc} gives the non-dimensional drag force which is opposite the direction of the cavitator velocity vector. Similarly C_{Lc} gives the non-dimensional cavitator lift force perpendicular to the drag and defined as positive upwards by [6]. The opposite of the lift and drag vectors define the cavitator wind axes, *w-frame*. The lift and drag expressed in the cavitator wind axes can be transformed into the the cavitator axes *c-*

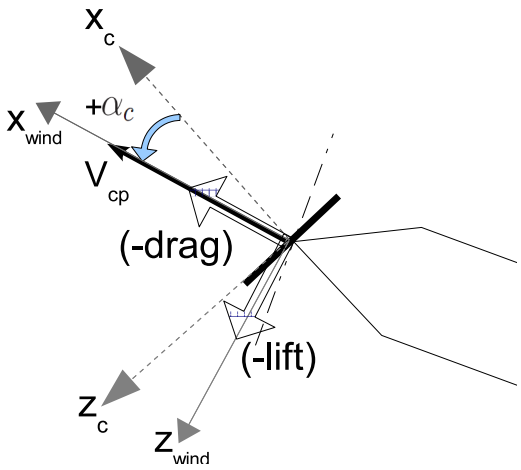

Figure 2.5: Diagram showing the necessary rotation of the lift and drag forces into the cavitator frame and then to the body frame.

frame and then to the body axes *b-frame*, as shown in Equation (2.18). The frame in which the force is expressed is denoted by a superscript. Figure 2.5 is representative of the following transformations from *w-frame* $\rightarrow$ *c-frame* $\rightarrow$ *b-frame*.

$$\bar{F}_c^{wind} = \begin{bmatrix} -D_c \\ 0 \\ -L_c \end{bmatrix} \tag{2.17}$$

$$\begin{aligned} \bar{F}_c^{body} =& DCM_{cb}^T \cdot DCM_{wc}^T \cdot \bar{F}_c^{wind} \\ =& \begin{bmatrix} cos(\delta_c) & 0 & sin(\delta_c) \\ 0 & 1 & 0 \\ -sin(\delta_c) & 0 & cos(\delta_c) \end{bmatrix} \begin{bmatrix} cos(-\alpha_c) & 0 & sin(-\alpha_c) \\ 0 & 1 & 0 \\ -sin(-\alpha_c) & 0 & cos(-\alpha_c) \end{bmatrix} \begin{bmatrix} -D_c \\ 0 \\ -L_c \end{bmatrix} \\ =& \begin{bmatrix} cos\delta_c(-D_c \cdot cos\alpha_c + L_c \cdot sin\alpha_c) + sin\delta_c(-D_c \cdot sin\alpha_c - L_c \cdot cos\alpha_c) \\ 0 \\ -sin\delta_c(-D_c \cdot cos\alpha_c + L_c \cdot sin\alpha_c) + cos\delta_c(-D_c \cdot sin\alpha_c - L_c \cdot cos\alpha_c) \end{bmatrix} \end{aligned} \tag{2.18}$$

Equation (2.18) is a complete expression for the longitudinal force of the cavitator on the vehicle cg, expressed in the body frame. The polynomial approximations of the drag and lift coefficients (Equations (2.12) and (2.13)) can be dimensionalized as shown below to obtain D_c and L_c.

$$\begin{aligned} D_c &= C_{Dc}\bar{q}_c A_c \\ L_c &= C_{Lc}\bar{q}_c A_c \\ \bar{q}_c &= \frac{1}{2}\rho V_c^2 \\ A_c &= \frac{\pi}{4} d_c^2 \end{aligned}$$

There is no moment coefficient contribution for a disk cavitator, thus the only mo-

ments are those induced by the force $\bar{F}_c$.

$$\begin{aligned} M_c^{body} &= \bar{r}^b_{cg\to cp} \times F_c^{body} \\ &= \begin{bmatrix} 0 & 0 & 0 \\ 0 & 0 & -l_c \\ 0 & l_c & 0 \end{bmatrix} \begin{bmatrix} F_{c_x} \\ 0 \\ F_{c_z} \end{bmatrix} \\ &= \begin{bmatrix} 0 \\ -l_c F_{c_z} \\ 0 \end{bmatrix} \end{aligned} \tag{2.19}$$

Equation (2.18) and (2.19) are the non-linear expressions for the force and moment from the cavitator on the vehicle expressed in the body frame.

2.3.2 Simplification

The longitudinal model in Equation (2.48) assumes a constant $x-body$ velocity, thus it is only necessary to look at F_{c_z} and M_{c_y}. The force and moment equations for the cavitator can be simplified greatly using a small angle approximation. Applying the small angle approximation and looking only at the terms of interest for the two state longitudinal model, Equations (2.18) and (2.19) are reduced to:

$$F_{c_z} = -\delta_c(-D_c + L_c\alpha_c) + (-D_c\alpha_c - L_c); \tag{2.20}$$

$$M_{c_y} = -l_c\, F_{c_z} \tag{2.21}$$

The nonlinear expression for the cavitator angle of attack can also be simplified as follows

$$\begin{aligned}\alpha_c &= tan^{-1}\left(\frac{w_c}{u_c}\right) \\ &\approx \frac{u\delta_c}{u-\delta_c(w-l_cq)} + \frac{w-l_cq}{u-\delta_c(w-l_cq)}\end{aligned}$$

The u term in the denominator dominates and so the denominator can be approximated $u-\delta_c(w-l_cq) \approx u$. Thus the expression can be further simplified

$$\begin{aligned}\alpha_c &\approx \frac{u\delta_c}{u} + \frac{w-l_cq}{u} \\ &\approx \delta_c + \alpha - \frac{l_cq}{u}\end{aligned} \tag{2.22}$$

This derivation was accomplished for a disk cavitator, but another shape cavitator may also be used if the equations for the hydrodynamic coefficients are known. Additionally, if the non-disk shape cavitator has a moment coefficient, that must also be added to the moment equation.

2.4 Planing

The force and moment expressions for planing are not trivial. The community has yet to settle on a model that is well suited for dynamic modeling purposes. The work of Logvinovich and Paryshev are cited often in the planing literature relating to supercavitation, for example, [7], [8], and [9]. Both Logvinovich and Paryshev take an analytically based fluid dynamic approach to the planing problem and the resulting expressions are not trivially implementable into a dynamic simulation. A simple expression for the planing force based on theory from Logvinovich is given in [4], though there is no discussion of its derivation. There is room to improve the

modeling of planing so as to

- capture the relationship between the forces and moments of planing to the static and dynamic state of the vehicle
- allow for implementation in a dynamic model

As opposed to using the above references' planing force and moment expressions, it was decided to continue utilizing non-dimensional coefficients. This way the model can be updated as better data becomes available on the hydrodynamic coefficients and even the fluid dynamic expressions can be used to back out hydrodynamic coefficients for comparison purposes. The basis for this approach is an extensive study on planing of cylinders conducted at California Institute of Technology [10]. To the extent we are aware, this extensive planing study has been relatively unused by the community of researchers working on dynamic modeling and control of supercavitating vehicles.

The work in [10] studies the forces and moments from a planing cylinder as a function of angle of attack, cavitation number, immersion depth, and the curvature of the fluid surface on which the planing occurs. The data for lift, drag, moment, and non-dimensional *cp* location was digitized in the region of interest. This region is namely for small cavitation number, angle of attack, and immersion depth. Since the non-dimensional center of pressure is given, the moment induced by the lift and drag can be calculated and thus there is no need for the moment coefficient data (which is given about the tail of the vehicle). The digitized data for the lift, drag, and non-dimensional *cp* are shown in Figure 2.6, Figure 2.7, and Figure 2.8. For the non-dimensional *cp*, L_1 is the distance from the tail of the vehicle to the center of pressure. A positive L_1 is the distance from the tail towards the nose of the vehicle.

CL σ = 0.08		submergence ratio h/d		
		0	0.2	0.4
angle of attack α (deg)	5	0.000	0.053	0.087
	6	0.000	0.055	0.080
	7	0.000	0.062	0.080
	8	0.000	0.069	0.086
	9	0.000	0.077	0.091
	10	0.000	0.080	0.107
	11	0.000	0.084	0.116
	12	0.000	0.090	0.123
	13	0.000	0.097	0.131
	14	0.000	0.100	0.135
	15	0.000	0.101	0.140
	16	0.000	0.102	0.146
	17	0.000	0.104	0.154
	18	0.000	0.106	0.160
	19	0.000	0.107	0.167

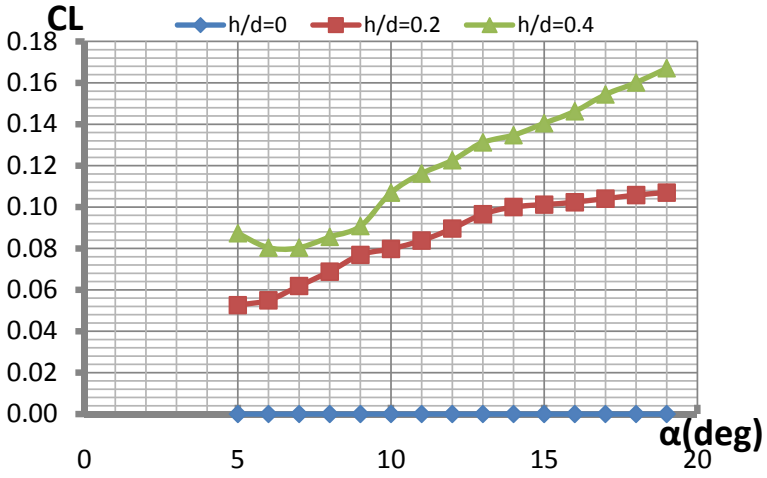

Figure 2.6: Table and plot of planing lift coefficient as function of angle of attack (α_{cb}) and immersion depth [10]

CD σ = 0.08	submergence ratio h/d		
angle of attack α (deg)	0	0.2	0.4
6	0.000	0.022	0.040
8	0.000	0.023	0.041
10	0.000	0.025	0.042
12	0.000	0.026	0.046
14	0.000	0.027	0.043
15	0.000	0.029	0.048
16	0.000	0.030	0.051
17	0.000	0.031	0.054
18	0.000	0.033	0.057
19	0.000	0.034	0.060

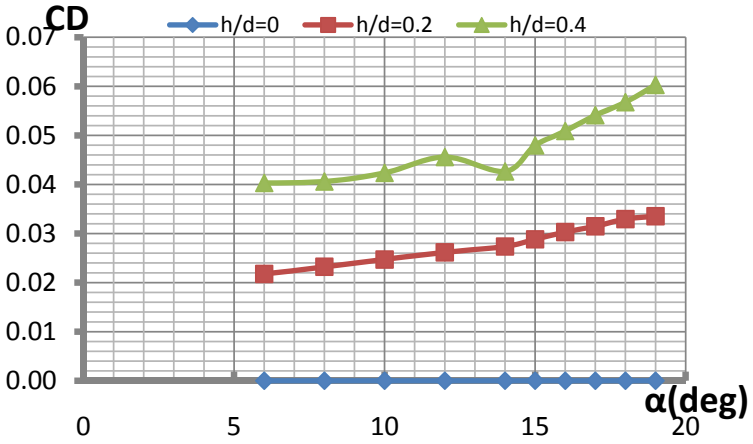

Figure 2.7: Table and plot of planing drag coefficient as function of angle of attack (α_{cb}) and immersion depth [10]

L1/D σ = 0.08	submergence ratio h/d		
angle of attack α (deg)	0	0.2	0.4
8	0.000	1.588	2.529
9	0.000	1.500	2.382
10	0.000	1.324	2.221
11	0.000	1.176	2.029
12	0.000	1.118	1.853
13	0.000	1.059	1.765
14	0.000	1.000	1.676
15	0.000	0.882	1.559
16	0.000	0.794	1.456
17	0.000	0.735	1.382
18	0.000	0.588	1.176
19	0.000	0.515	1.044

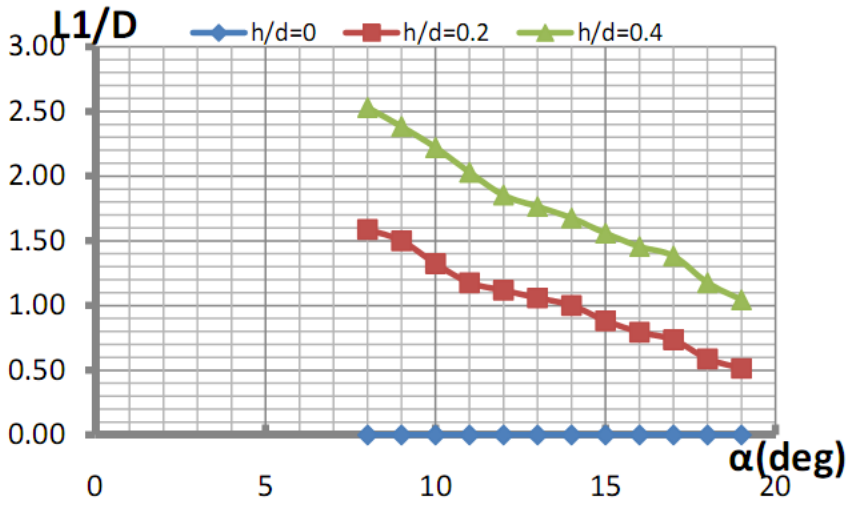

Figure 2.8: Table and plot of planing non-dimensional *cp* location as function of angle of attack (α_{cb}) and immersion depth [10]

As was done with the cavitator, the planing coefficient data can be fit with polynomials as

$$C_{Dp} \approx c_1|\alpha_{cb}| + c_2\frac{h}{D_{body}} \tag{2.23}$$

$$C_{Lp} \approx c_3|\alpha_{cb}| + c_4\frac{h}{D_{body}} \tag{2.24}$$

$$\frac{L_1}{D_{body}} \approx c_5 + c_6|\alpha_{cb}| + c_7\frac{h}{D_{body}} \tag{2.25}$$

$$l_p = l_t - \left(\frac{L_1}{D_{body}}\right) D_{body} \tag{2.26}$$

where l_p is the distance from the vehicle cg to the point of planing. For $\sigma = 0.08$, then $c_1 = 0.0002(180/\pi)$, $c_2 = 0.1151$, $c_3 = 0.0014(180/\pi)$, $c_4 = 0.2751$, $c_5 = 1.0508$, $c_6 = -0.0743(180/\pi)$, and $c_7 = 4.3900$. Note that α_{cb} is the angle between the cavity and the body at the point of planing and must be positive in units of radians. This is a difficult angle to measure and so it has been approximated as the absolute value of the angle of attack at the nose of the vehicle. Namely

$$\alpha_{cb} \approx tan^{-1}\left(\frac{w - l_c q}{u}\right) \tag{2.27}$$

The rationale behind this approximation is the fact that the cavity is incepted and created by the nose of the vehicle. Ignoring the effects of buoyancy, as has been done in this thesis for simplicity, the angle between the vehicle centerline and the cavity centerline is determined by the angle of attack at the nose of the vehicle. A more detailed approximation would include both buoyancy and the effect of the cavity curvature on α_{cb}.

2.4.1 Nonlinear Expression

The expressions for the forces and moments caused by planing are derived in a similar fashion as it was for the cavitator, with one difference. There will be a switch in the direction of the planing lift force contribution depending on whether the vehicle is planing on the bottom or top of the cavity. An intermediate planing frame will be used which is defined with its origin at the *cp* of planing. The $x-axis$ is parallel to the body $x-axis$ but the $z-axis$ is defined to always point into the wall in which planing is occurring. In the case that the vehicle is planing onto the bottom of the cavity, the planing frame is simply a translation of the body frame from the *cg* of the vehicle to the *cp* of planing. In the case that the vehicle is planing on the top part of the cavity, the body frame is translated as well as rotated about the body $x-axis$ by 180^o. The effect of this rotation, denoted by angle Φ, will be embedded into the transformation matrix from the body frame to the local planing frame.

The position vector from the *cg* of the vehicle to the center of pressure of planing and the transformation matrix from the body frame to the local planing frame are

$$\begin{aligned} \bar{r}_{cg\to cp} =& [-l_p, 0, 0]^T \\ DCM_{pb} =& \begin{bmatrix} 1 & 0 & 0 \\ 0 & cos(\Phi) & sin(\Phi) \\ 0 & -sin(\Phi) & cos(\Phi) \end{bmatrix} \end{aligned} \tag{2.28}$$

where l_p has been defined in (2.26) and the planing *cp* is approximated as being located on the vehicle centerline. The value of the angle Φ in the transformation matrix DCM_{pb} depends on whether planing is occurring at the bottom or top of the cavity. The local planing frame is always oriented with the $x-axis$ along the body $x-axis$ and the $z-axis$ rotated to be pointed into the wall in which planing is occurring. In the case of planing on the bottom of the cavity, $\Phi = 0$ and the DCM_{pb}

becomes the identity matrix. In the case that the vehicle is planing on the top of the cavity, then $\Phi = \pi$ radians and rotates the local planing frame to match the desired notation.

As was done with the cavitator, the local velocity in the planing frame is given as

$$\begin{aligned}
\bar{V}_{cp}^{local} =& DCM_{pb}[\bar{V}_{cg} + \omega \times \bar{r}_{cg \to cp}] \\
=& DCM_{pb} \left\{ \begin{bmatrix} u \\ 0 \\ w \end{bmatrix} + \begin{bmatrix} 0 \\ q \\ 0 \end{bmatrix} \times \begin{bmatrix} -l_p \\ 0 \\ 0 \end{bmatrix} \right\} \\
=& \begin{bmatrix} u \\ 0 \\ (w + l_p q) cos(\Phi) \end{bmatrix} \equiv \begin{bmatrix} u_p \\ 0 \\ w_p \end{bmatrix}
\end{aligned}$$

Using the definition of angle of attack, the local angle of attack (α_p) of the planing surface and the local speed (V_p) can be determined

$$\begin{aligned}
\alpha_p &= tan^{-1} \left(\frac{w_p}{u_p} \right) \\
&= tan^{-1} \left(\frac{(w + l_p q) cos(\Phi)}{u} \right) \qquad (2.29) \\
V_p &= \sqrt{u_p^2 + w_p^2} \qquad (2.30)
\end{aligned}$$

The polynomial approximations for lift and drag coefficient of planing given in

(2.23) and (2.24) can be dimensionalized as shown below to obtain D_p and L_p

$$
\begin{aligned}
D_p &= C_{Dp}\bar{q}_p D_{body}^2 \\
L_p &= C_{Lp}\bar{q}_P D_{body}^2 \\
\bar{q}_p &= \frac{1}{2}\rho V_p^2
\end{aligned}
$$

thus the drag and lift planing forces in the wind axes can be determined. Note that it is in accordance with [10] that the planing drag and lift coefficients are dimensionalized with $\bar{q}_p D_{body}^2$. Transforming the wind axes forces to the local planing axes and thereafter to the body axes, the final expression for the planing forces on the vehicle cg are

$$
\bar{F}_p^{wind} = \begin{bmatrix} -D_p \\ 0 \\ -L_p \end{bmatrix} \tag{2.31}
$$

$$
\begin{aligned}
\bar{F}_p^{body} =& DCM_{pb}^T \cdot DCM_{wp}^T \cdot \bar{F}_p^{wind} \\
=& \begin{bmatrix} 1 & 0 & 0 \\ 0 & cos(\Phi) & -sin(\Phi) \\ 0 & sin(\Phi) & cos(\Phi) \end{bmatrix} \begin{bmatrix} cos(-\alpha_p) & 0 & sin(-\alpha_p) \\ 0 & 1 & 0 \\ -sin(-\alpha_p) & 0 & cos(-\alpha_p) \end{bmatrix} \begin{bmatrix} -D_p \\ 0 \\ -L_p \end{bmatrix} \\
=& \begin{bmatrix} -D_p \cdot cos\alpha_p + L_p \cdot sin\alpha_p \\ 0 \\ cos\Phi(-D_p \cdot sin\alpha_p - L_p \cdot cos\alpha_p) \end{bmatrix}
\end{aligned} \tag{2.32}
$$

Equation (2.32) is a complete expression for the longitudinal force of planing on the vehicle cg, expressed in the vehicle body frame.

The only planing moment contribution currently accounted for is the moment

induced by the force $\bar{F}_p$.

$$\begin{aligned}\bar{M}_p^{body} &= \bar{r}^b_{cg\to cp} \times \bar{F}_p^{body} \\ &= \begin{bmatrix} 0 & 0 & 0 \\ 0 & 0 & l_p \\ 0 & -l_p & 0 \end{bmatrix} \begin{bmatrix} F_{p_x} \\ 0 \\ F_{p_z} \end{bmatrix} \\ &= \begin{bmatrix} 0 \\ l_p F_{p_z} \\ 0 \end{bmatrix} \end{aligned} \tag{2.33}$$

Equation (2.32) and (2.33) are the nonlinear expressions for the force and moment from planing on the vehicle expressed in the body frame.

2.4.2 Simplification

The planing force and moment nonlinear equations can be greatly simplified. Employing the fact that the $x-body$ velocity remains constant, the F_{p_x} expression can be dropped. Applying small angle approximation to the remaining F_{p_z} and M_{p_y} results in

$$F_{p_z} = cos(\Phi)(-D_p\alpha_p - L_p); \tag{2.34}$$

$$M_{p_y} = l_p\, F_{p_z} \tag{2.35}$$

The nonlinear expressions for planing angle of attack and the angle between the cavity and the body can also be simplified using the same reasoning as was used in Equation

(2.22) for the cavitator. The resulting simplified expression is

$$\alpha_p \approx \alpha + \frac{l_p q}{u} \tag{2.36}$$

$$\alpha_{cb} \approx \alpha - \frac{l_c q}{u} \tag{2.37}$$

This derivation for the planing forces and moments was accomplished using hydrodynamic coefficients. Though the planing hydrodynamic data that is used in this thesis comes from [10], the derived framework allows for any future sources of hydrodynamic data to be used as well.

2.4.3 Cavity Model

The cavity of a supercavitating vehicle is a main feature in modeling of the vehicle environment. Experimental research on the two dimensional cavity outline as well as the effect of the cavitator angle of attack on the outline of the cavity is in [11] and [12], respectively. Accurate modeling of cavity dynamics continues to be a topic of research, for example [13]. Two cavity models were utilized for different purposes in this work.

Time Dependent Cavity Model

The first model is by Logvinovich [7] and provides the radius of the cavity as a function of time since making contact with the cavitator. The Logvinovich model can include time delay effects, meaning the time history of the cavitator location determines the cavity shape. Logvinovich's cavity model and the relevant equations are shown in Equations (2.38) to (2.40).

$$R_c(t) = R_{max}\sqrt{1 - \left(1 - \frac{R_1^2}{R_{max}^2}\right)\left|1 - \frac{t}{t_{max}}\right|^{\frac{2}{\kappa}}} \tag{2.38}$$

$$R_1 = 1.92R_n$$

$$L_{max} = R_{max}\left(\frac{1.92}{\sigma} - 3\right) \tag{2.39}$$

$$t_{max} = \frac{L_{max}}{V_m}$$

$$R_{max} = R_n\sqrt{\frac{C_{x0}(1+\sigma)}{k\sigma}} \tag{2.40}$$

Here R_c is the radius of the cavity, R_{max} is the maximum radius of the cavity, t_{max} is the time for a cavity section to grow to R_{max}, and R_n is the disk cavitator radius. The distance from the front of the cavity to the point of maximum radius, R_{max} is denoted L_{max}. By this notation, cavity inception occurs at $t = 0$ and closure at $t = 2 * t_{max}$. Finally k approaches 1 as the cavitation number nears 0 and so we take $k = 1$, and κ is a correction multiplier taken as $\kappa = 0.85$. [7].

Among the limitations of the Logvinovich cavity model is the poor accuracy in capturing the frontal portion of the cavity shape. This model is typically married to an empirical formula which gives a better approximation of the frontal portion. This empirical formula is shown in Equation (2.41), where x is the distance downstream from the cavitator centerline. It is worth noting that for small values of x, the frontal cavity shape does not depend on the cavitation number σ. A visual comparison of the two equations is shown in Figure 2.9.

$$R_c(x) = R_n\left(1 + 3\frac{x}{R_n}\right)^{1/3} \tag{2.41}$$

Furthermore, at $\frac{t}{t_{max}} > 1.5$ the cavity boundaries become uncertain as froth begins

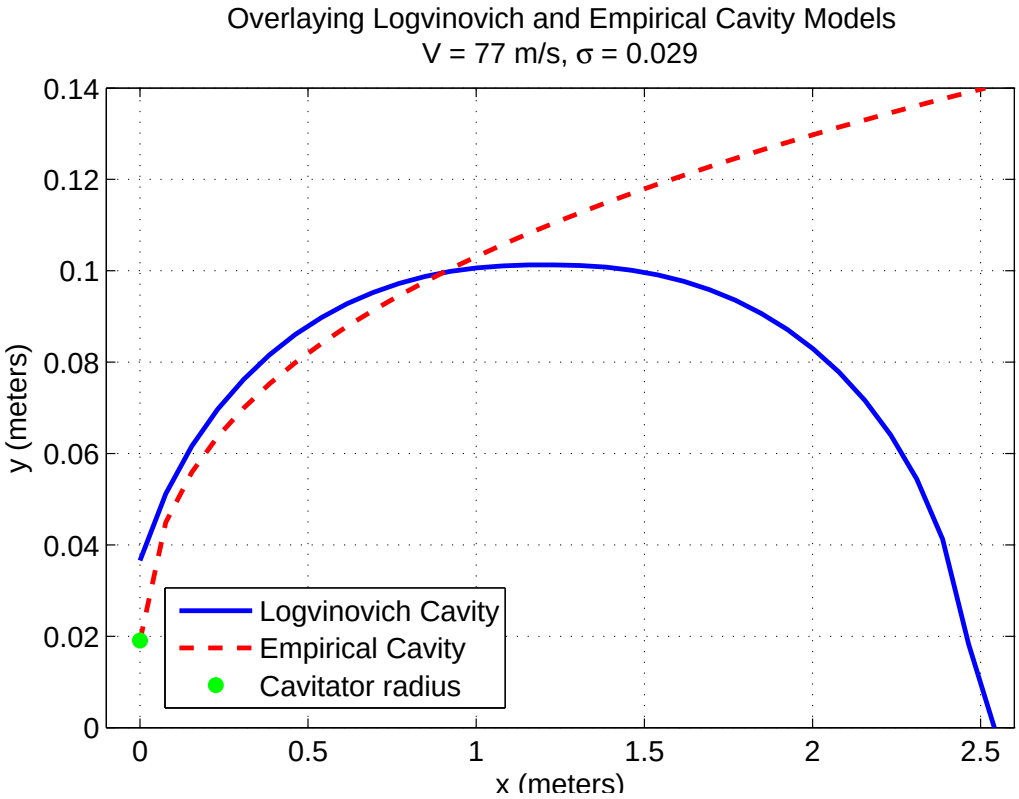

Figure 2.9: Example case showing the empirical formula's approximation of the frontal portion of the cavity. The empirical formula is only valid for the frontal portion of the cavity. The Logvinovich cavity radius was calculated as a function of position using $t = \frac{x}{V}$

forming. The Logvinovich cavity model is used in the full nonlinear simulation of the vehicle, which also captures the time delay effect on the cavity shape. The empirical cavity formula is not included since the goal of modeling the cavity is to detect planing, which occurs in the later portion of the cavity. Additionally, the uncertain cavity boundary is not included in this analysis because the simulation requires a defined cavity boundary from which to detect planing.

Elliptical Instantaneous Cavity Model

The second cavity model assumes an instantaneous elliptical cavity formed by the cavitator. The elliptical cavity model [5] and the relevant equations are shown in Equation (2.42).

$$R_c(t) = R_{max}\left(1 - \left(\frac{x - L_c/2}{L_c/2}\right)^2\right)^{\frac{1}{2.4}} \tag{2.42}$$

where $L_c = 2L_{max}$ and L_{max}, R_{max} are defined in Equation (2.39) and (2.40) respectively. The elliptical cavity model ignores time delay affects and as implemented, generates instantaneous cavities along the direction of the cavitator velocity vector. This thesis is concerned with modeling for control system design and analysis, and a cavity model which adequately captures the cavity shape and lends itself well to numerical implementation is required. The goal of the simplified vehicle model is to obtain linear models of the non-planing and planing vehicle, and not necessarily to study the switching between the two conditions. For this purpose, the elliptical model was used in the simplified nonlinear model. The simplified nonlinear model is used for trimming and linearizing the equations of motion, and is the basis for the subsequent analyses of the vehicle linear dynamics.

2.4.4 Detecting Planing

The simulation of the supercavitating vehicle requires determination of the position of the vehicle with respect to the cavity. This requires information about the cavity dynamics as well as the relative position between the body and cavity. For this section the goal is to obtain simple models from which physical insight can be extracted. To do so, two approaches were investigated for detecting when to apply planing forces.

The first approach is using geometric relationships. The cavity centerline is along the velocity vector of the cavitator, ignoring any time delay or buoyancy characteristics of the cavity. In theory one can calculate the immersion depth using the length of the cavity and the body, the angle between the cavity and the body centerline, and the radius of both the body and the cavity at the end of the vehicle. The ability of the simple geometric approach to detect planing was very poor when compared to the full non-linear simulation which uses a more complicated and accurate method to detect planing, discussed in the appendix.

The second approach is to use a full nonlinear simulation to simulate a longitudinal planing condition. Thereafter, the start to finish of a single planing occurrence can be analyzed and the states fitted to gain a polynomial relationship between the planing immersion depth and the other vehicle states of interest. This approach was found to be satisfactory and did well in capturing a single planing occurrence. Simulating the vehicle starting with a $x - body$ velocity of $77m/s$ and all other states at zero, the first planing occurrence was captured and fit using least squares to obtain

$$\frac{h}{D_{body}} \approx \frac{1}{D_{body}}(c_8 + c_9\alpha + c_{10}q) \tag{2.43}$$

In this condition the coefficients were found to be $c_8 = -0.02430m$, $c_9 = 2.06631\frac{m}{rad}$, and $c_{10} = 0\frac{m}{rad/s}$. Essentially there was little contribution from q in the fitting. Looking at (2.43), if $\alpha = 0$ then $\frac{h}{D_{body}}$ will be negative. Planing forces are applied

only when a positive immersion depth is calculated, thus to the following condition is added

$$
\begin{aligned}
&if\ \frac{h}{D_{body}} < 0 \\
&\quad \frac{h}{D_{body}} = 0 \\
&\quad \alpha_{cb} = 0 \\
&end
\end{aligned}
$$

Since the planing lift and drag coefficient polynomials depends on both $\frac{h}{D_{body}}$ and α_{cb}, this condition ensures that no planing force or moment is applied if the vehicle is not planing.

This approach was found to capture planing very well compared to the full non-linear model. The limitation of this approach is that the coefficients for the fitted immersion depth polynomial must be updated using a nonlinear simulation for any change in the conditions which are being simulated. A more detailed approach to detecting planing and accounting for the time delay effects accompanied with the cavity location is addressed later in the thesis.

2.5 Gravity and Thrust

Gravity will act at the center of gravity of the vehicle and when expressed in the body frame is given by Equation (2.44), where $g > 0$.

$$\bar{F}_g^{body} = \begin{bmatrix} -m\,g\,sin(\theta) \\ 0 \\ m\,g\,cos(\theta) \end{bmatrix} \tag{2.44}$$

Applying the small angle approximation, the gravity force vector would be

$$\bar{F}_g^{body} = \begin{bmatrix} -m\,g\,\theta \\ 0 \\ m\,g \end{bmatrix} \tag{2.45}$$

The thrust vector acts at the tail of the vehicle and has both a *x-body* and *z-body* component. When also expressed in the vehicle body frame, the force and moment from thrust is given by Equations (2.46) and (2.47) respectively, where $l_t > 0$ and T_x, T_z are the input thrust magnitudes.

$$\bar{F}_T^{body} = \begin{bmatrix} T_x \\ 0 \\ T_z \end{bmatrix} \tag{2.46}$$

$$\bar{M}_T^{body} = \begin{bmatrix} 0 \\ l_t\,T_z \\ 0 \end{bmatrix} \tag{2.47}$$

Non-Planing Trim Condition		**Planing Trim Condition**	
Name	Value	Name	Value
u	77 m/s	u	76.3 m/s
w	0 m/s	w	0.9396 m/s
q	0 rad	q	0 rad
θ	0 rad	θ	0.05 rad
δ_c	-0.0404 rad	δ_c	-0.0358 rad
T_x	2953.7 N	T_x	2954.6 N
T_z	-117.119 N	T_z	0 N
		$\frac{h}{D_{body}}$	0.0113

Table 2.2: Trim condition for non-planing and planing nonlinear 3 DOF equations where $\sigma = 0.08$ and the polynomial approximations are used for hydrodynamic coefficients.

2.6 Trim Conditions

The force and moment expressions for the disk cavitator, planing, gravity, and thrust are plugged into the two state nonlinear equations, namely Equations (2.9) and (2.10). The two state longitudinal model in a planing and non-planing condition has been derived in a simplified symbolic format. The symbolic nature of the derivation simplifies the process of connecting the observed dynamics to the physical parameters of the vehicle. Setting $\dot{\alpha} = 0$, $\dot{q} = 0$, Equations (2.9) and (2.10) can be solved for an equilibrium set of state conditions and vehicle inputs, referred to as a trim point. The nonlinear equations are then linearized about the obtained trim points. A non-planing and a planing trim condition for the nonlinear model is obtained in this manner, and are listed in Table 2.2.

2.6.1 Time Delay Effects

Note that for trimming the vehicle in the planing condition, the elliptical cavity model was utilized and no cavity pulsation or time delay affects were included. The elliptical cavity was instantaneously generated with the cavity centerline along the

direction of the cavitator velocity vector. This simplified the trimming of the vehicle and accomplished the goal of obtaining a model of the linear dynamics while the vehicle is planing. Nevertheless, the nonlinear vehicle does have different dynamics if cavity formation time delay effects are included. For example, simulating open loop untrimmed vehicle motion while including time delay effects resulted in an undamped switching between planing on the bottom and top of the cavity and ultimately leading to instability. Simulating the same condition without cavity time delay dynamics, the vehicle impinges onto the bottom of the cavity several times and finally settles in a stable planing condition.

The time delay effects complicate the interaction between the vehicle and the cavity and can lead to instability. When analyzing the linear planing dynamics in the following sections, these complex vehicle and cavity interactions have been disregarded.

2.7 Linearization

The remainder of the linear analysis in the thesis uses a linearization of the vehicle about the non-planing and planing trim conditions given in Table 2.2. The equations are linearized about the trim point using a Taylor series first order approximation. The linearized equations are expressed in state space form as

$$\begin{bmatrix} \dot{\alpha} \\ \dot{q} \end{bmatrix} = \begin{bmatrix} \frac{1}{u\,m}\left(\frac{\partial F_{c_z}}{\partial \alpha} + \frac{\partial F_{p_z}}{\partial \alpha}\right) & \frac{1}{u\,m}\left(\frac{\partial F_{c_z}}{\partial q} + \frac{\partial F_{p_z}}{\partial q}\right) + 1 \\ \frac{1}{I_{yy}}\left(\frac{\partial M_{c_y}}{\partial \alpha} + \frac{\partial M_{p_y}}{\partial \alpha}\right) & \frac{1}{I_{yy}}\left(\frac{\partial M_{c_y}}{\partial q} + \frac{\partial M_{p_y}}{\partial q}\right) \end{bmatrix} \begin{bmatrix} \alpha \\ q \end{bmatrix} + \begin{bmatrix} \frac{1}{u\,m}\left(\frac{\partial F_{c_z}}{\partial \delta_c}\right) & \frac{1}{u\,m} \\ \frac{1}{I_{yy}}\left(\frac{\partial M_{c_y}}{\partial \delta_c}\right) & \frac{l_t}{I_{yy}} \end{bmatrix} \begin{bmatrix} \delta_c \\ T_z \end{bmatrix} \tag{2.48}$$

where a coordinate change is implied making the linear states represent deviations from the trim point. Equation (2.48) is the linearized longitudinal equation of motion for the supercavitating vehicle. In the case that the vehicle is entirely within the

cavity, the planing force and moment terms disappear. Additionally, if another vehicle configuration is analyzed which included fins or canards, their respective contributions can easily be included into the linear model.

2.8 Non-Planing Linear Model

Equation (2.48) is used with all planing terms set to zero. In the non-planing case, the partial derivatives of the forces and moments with respect to the states and inputs are computed

$$\begin{aligned}
\frac{\partial F_{c_z}}{\partial \alpha} &= \bar{q}\, A_c \left(\alpha_c\, \delta_c\, 2(k_3 - k_2) + \alpha_c^2 (3\, k_2) + (k_3 - k_1)\right) \\
\frac{\partial F_{c_z}}{\partial q} &= \frac{-l_c\, \bar{q}\, A_c}{u} \left(\alpha_c\, \delta_c\, 2(k_3 - k_2) + \alpha_c^2 (3\, k_2) + (k_3 - k_1)\right) \\
\frac{\partial F_{c_z}}{\partial \delta_c} &= \bar{q}\, A_c \left(\alpha_c\, \delta_c\, 2(k_3 - k_2) + \alpha_c^2 (k_3 + 2\, k_2) + k_3\right)
\end{aligned}$$

Since $M_{c_y} = -l_c\, F_{c_z}$, then the following will hold:

$$\begin{aligned}
\frac{\partial M_{c_y}}{\partial \alpha} &= -l_c \left(\frac{\partial F_{c_z}}{\partial \alpha}\right) \\
\frac{\partial M_{c_y}}{\partial q} &= -l_c \left(\frac{\partial F_{c_z}}{\partial q}\right) \\
\frac{\partial M_{c_y}}{\partial \delta_c} &= -l_c \left(\frac{\partial F_{c_z}}{\partial \delta_c}\right)
\end{aligned}$$

Plugging in the numerical values for the entries to the non-planing longitudinal linear state-space model results in (2.49).

$$\begin{bmatrix} \dot{\alpha} \\ \dot{q} \end{bmatrix} = \begin{bmatrix} -0.299 & 1.00 \\ 109.5 & -1.60 \end{bmatrix} \begin{bmatrix} \alpha \\ q \end{bmatrix} + \begin{bmatrix} 1.45 & 0.0006 \\ -530.7 & 0.182 \end{bmatrix} \begin{bmatrix} \delta_c \\ T_z \end{bmatrix} \tag{2.49}$$

2.9 Planing Linear Model

The planing linear model includes the non-planing model terms as well as the partial derivatives of the planing forces and moments with respect to the states and inputs

$$\frac{\partial F_{p_z}}{\partial \alpha} = -\bar{q} D_{body}^2 \left(c_4 \alpha_{cb} + c_5 \frac{h}{D_{body}} + \left(\frac{c_5 c_9}{D_{body}} + c_4 \right) \alpha_p + \frac{c_7 c_9}{D_{body}} + c_6 \right)$$
$$\frac{\partial F_{p_z}}{\partial q} = -\bar{q} D_{body}^2 \left(\left(\frac{c_5 c_{10}}{D_{body}} - \frac{c_4 l_c}{u} \right) \alpha_p + \frac{c_7 c_{10}}{D_{body}} - \frac{c_6 l_c}{u} + \frac{l_p}{u} \left(c_4 \alpha_{cb} + c_5 \frac{h}{D_{body}} \right) \right)$$

Since $M_{p_y} = l_p \, F_{p_z}$, then the following will hold for the moments

$$\frac{\partial M_{p_y}}{\partial \alpha} = l_p \left(\frac{\partial F_{p_z}}{\partial \alpha} \right)$$
$$\frac{\partial M_{p_y}}{\partial q} = l_p \left(\frac{\partial F_{p_z}}{\partial q} \right)$$

Plugging in the numerical values for the entries to the planing longitudinal linear state-space model results in (2.50).

$$\begin{bmatrix} \dot{\alpha} \\ \dot{q} \end{bmatrix} = \begin{bmatrix} -102.4 & 1.025 \\ -2757 & 4.054 \end{bmatrix} \begin{bmatrix} \alpha \\ q \end{bmatrix} + \begin{bmatrix} 1.43 & 0.0006 \\ -519.8 & 0.182 \end{bmatrix} \begin{bmatrix} \delta_c \\ T_z \end{bmatrix} \tag{2.50}$$

Chapter 3

Longitudinal Dynamics

The analysis of the longitudinal dynamics uses the planing and non-planing vehicle models derived in Chapter 2. The longitudinal model in Equation (2.48) will be rewritten such that the various force and moment terms are non-dimensionalized. Utilizing the non-dimensionalized terms are an attempt to minimize the effects of the specific trim condition and allow for a more general study of the vehicle dynamics. The rewritten longitudinal model is

$$\begin{bmatrix} \dot{\alpha} \\ \dot{q} \end{bmatrix} = \begin{bmatrix} \frac{\bar{q}}{um}\left(AC_{cav,z_\alpha} + D_{body}^2 C_{plan,z_\alpha}\right) & \frac{\bar{q}}{u^2 m}\left(Al_c C_{cav,z_q} + D_{body}^2 l_p C_{plan,z_q}\right) + 1 \\ \frac{\bar{q}}{I_{yy}}\left(Al_c C_{cav,m_\alpha} + D_{body}^2 l_p C_{plan,m_\alpha}\right) & \frac{\bar{q}}{I_{yy}u}\left(Al_c^2 C_{cav,m_q} + D_{body}^2 l_p^2 C_{plan,m_q}\right) \end{bmatrix} \begin{bmatrix} \alpha \\ q \end{bmatrix} + \begin{bmatrix} \frac{A\bar{q}}{um} C_{cav,z_\delta} & \frac{1}{um} \\ \frac{A\bar{q}l_c}{I_{yy}} C_{cav,m_\delta} & \frac{l_t}{I_{yy}} \end{bmatrix} \begin{bmatrix} \delta_c \\ T_z \end{bmatrix} \tag{3.1}$$

where each non-dimensional term is defined and values for the planing and non-planing condition are given in Table 3.1. The dynamics of the non-planing condition and the planing condition will be studied and compared using this framework.

Longitudinal Stability and Control Derivatives

Name	Definition	Non-Planing Value	Planing Value
C_{cav,z_α}	$\frac{1}{A\bar{q}}\frac{\partial F_{cav_z}}{\partial \alpha}$	-0.1507	-0.1527
C_{cav,z_q}	$\frac{1}{A\bar{q}}\left(\frac{u}{l_c}\right)\frac{\partial F_{cav_z}}{\partial q}$	0.1507	0.1527
C_{cav,z_δ}	$\frac{1}{A\bar{q}}\frac{\partial F_{cav_z}}{\partial \delta}$	0.7254	0.7223
C_{cav,m_α}	$\frac{1}{A\bar{q}l_c}\frac{\partial M_{cav}}{\partial \alpha}$	0.1507	0.1527
C_{cav,m_q}	$\frac{1}{A\bar{q}}\left(\frac{u}{l_c^2}\right)\frac{\partial M_{cav}}{\partial q}$	-0.1507	-0.1527
C_{cav,m_δ}	$\frac{1}{A\bar{q}l_c}\frac{\partial M_{cav}}{\partial \delta}$	-0.7254	-0.7223
C_{plan,z_α}	$\frac{1}{D_{body}^2\bar{q}}\frac{\partial F_{plan_z}}{\partial \alpha}$	-	-5.700
C_{plan,z_q}	$\frac{1}{D_{body}^2\bar{q}}\left(\frac{u}{l_p}\right)\frac{\partial F_{plan_z}}{\partial q}$	-	0.1068
C_{plan,m_q}	$\frac{1}{D_{body}^2\bar{q}}\left(\frac{u}{l_p^2}\right)\frac{\partial M_{plan}}{\partial q}$	-	0.1068
C_{plan,m_α}	$\frac{1}{D_{body}^2\bar{q}l_p}\frac{\partial M_{plan}}{\partial \alpha}$	-	-5.700

Table 3.1: The longitudinal stability and control derivatives for the non-planing and planing trim conditions

3.1 Non-Planing Condition

The cavitator is deflected to provide lift on the vehicle. The lift from the cavitator induces a moment on the vehicle which must be balanced. The counter moment could be provided by the fins if the vehicle had fins mounted on the tail. Since the vehicle being analyzed does not have fins, the counter moment is provided by thrust vectoring. The non-planing trim condition contains a $-117N$ thrust component in the $z-axis$ direction. This shows that in order to maintain a non-planing condition while supercavitating, the vehicle must have a means of balancing the moment created by the lift at the cavitator. Naturally, the location of the center of gravity can be used to leverage the amount of force necessary to balance the cavitator induced moment.

The transfer function of the non-planing vehicle from cavitator input to the vehi-

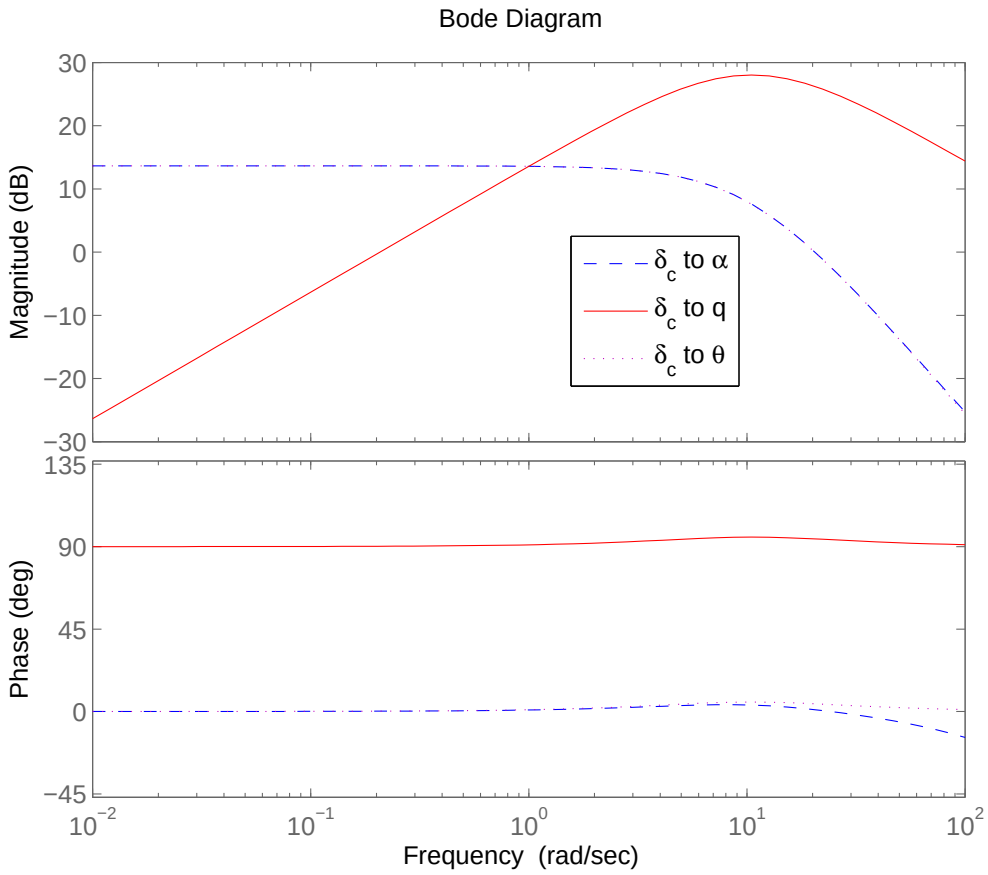

Figure 3.1: Non-planing vehicle Bode plot. The magnitude and phase response of the cavitator to angle of attack α and pitch angle θ are the same for the plotted frequency range.

Name	Definition	Non-Planing Value
C_{cav,z_α}	$\frac{1}{A\bar{q}}\frac{\partial F_{cav_z}}{\partial \alpha}$	-0.1507
C_{cav,z_q}	$\frac{1}{A\bar{q}}\left(\frac{u}{l_c}\right)\frac{\partial F_{cav_z}}{\partial q}$	0.1507
C_{cav,z_δ}	$\frac{1}{A\bar{q}}\frac{\partial F_{cav_z}}{\partial \delta}$	0.7254
C_{cav,m_α}	$\frac{1}{A\bar{q}l_c}\frac{\partial M_{cav}}{\partial \alpha}$	0.1507
C_{cav,m_q}	$\frac{1}{A\bar{q}}\left(\frac{u}{l_c^2}\right)\frac{\partial M_{cav}}{\partial q}$	-0.1507
C_{cav,m_δ}	$\frac{1}{A\bar{q}l_c}\frac{\partial M_{cav}}{\partial \delta}$	-0.7254

Static stability

Unstable

Figure 3.2: Term of importance to determining the vehicle static stability

cle's angle of attack and pitch rate are

$$\frac{\alpha(s)}{\delta_c(s)} = \frac{1.45(s-366.7)}{(s-9.6)(s+11.5)} \tag{3.2}$$

$$\frac{q(s)}{\delta_c(s)} = \frac{-530.7s}{(s-9.6)(s+11.5)} \tag{3.3}$$

where s is the Laplace variable. The non-planing vehicle longitudinal model is unstable and contains a right half plane pole at +9.6. The Bode response of cavitator input to angle of attack, pitch rate, and pitch angle are plotted in Figure 3.1. The angle of attack and pitch angle responses are very similar and will only differ at high frequencies where the far right half plane zero present in Equation (3.2) and will affect the Bode plot. The pitch rate can be used at higher frequencies through a stability augmentation system to assist in stabilizing the vehicle. The source of the vehicle instability in the non-planing case is related to the disk cavitator characteristics and is analyzed in more detail.

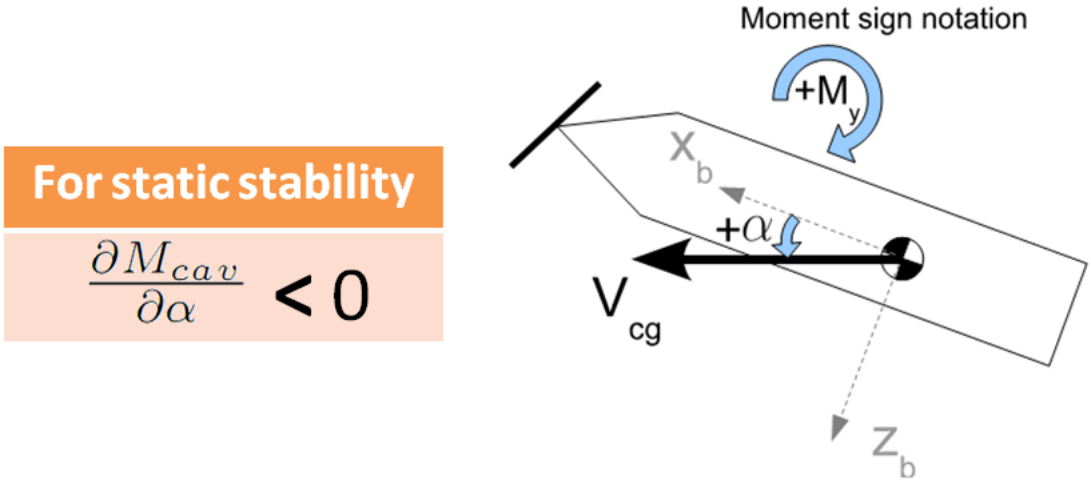

Figure 3.3: Sign notation for vehicle static stability

3.1.1 Static Stability

The change in pitching moment due to change in angle of attack determines the static longitudinal stability and must be negative for a "statically stable aircraft"[14]. This also holds for the supercavitating vehicle, where static stability implies that the vehicle tends to return towards its equilibrium condition after a disturbance. For the non-planing vehicle, the only moment contribution that depends on the vehicle angle of attack is the cavitator. Thus for static stability it is required that $C_{cav,m_\alpha} < 0$. Consider Figure 3.2, the non-planing trim condition $C_{cav,m_\alpha} > 0$ and therefore is statically unstable. An understanding of why C_{cav,m_α} must be negative can be obtained by considering Figure 3.3. A positive angle of attack will pitch the vehicle's nose upwards and in order for the vehicle to return to a level position, a negative moment must be applied to the vehicle.

The static stability term is determined by the properties of the cavitator and therefore the shape of the cavitator is important in determining the static stability of the vehicle.

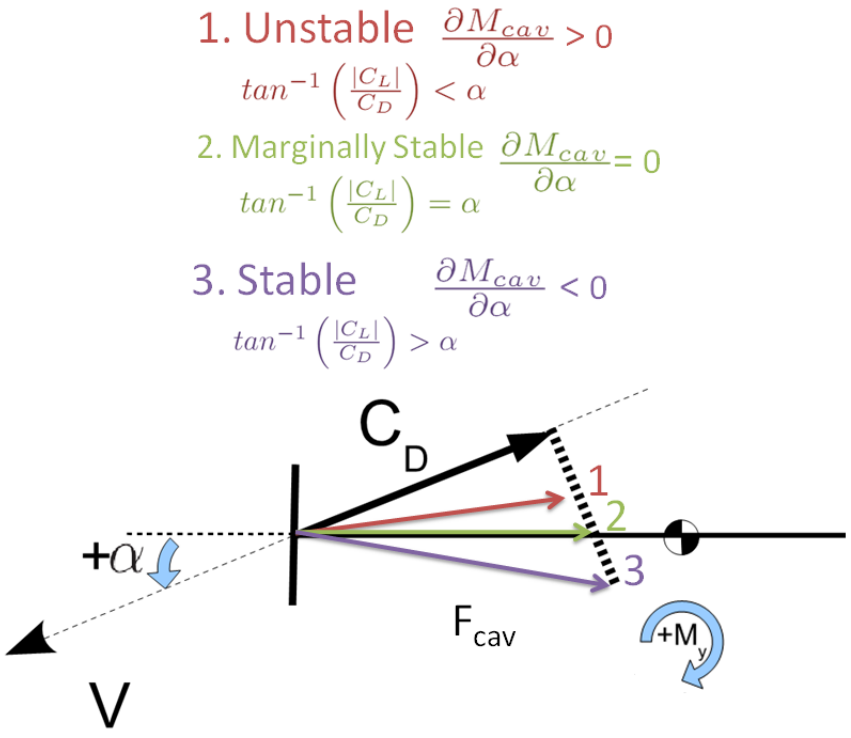

Figure 3.4: Static stability of disk cavitator, angles exaggerated purposely

Disk Cavitator

The intent is to connect the static instability of the vehicle to the physical characteristics of the disk cavitator. A qualitative study is conducted where the cavitator is undeflected ($\delta_c = 0$) with respect to the vehicle. The angle between the velocity vector and the resultant force vector on the cavitator is given by $tan^{-1}\left(\frac{|C_L|}{C_D}\right)$. The relation between this angle and the vehicle angle of attack, α, determines the directionality (and magnitude) of the moment applied to the vehicle. This relationship is shown graphically with exaggerated angles in Figure 3.4. The three possibilities determining the static stability property of the non-planing vehicle are shown in the same figure, where each possibility is numbered and color coded with the corresponding orientation of the F_{cav} force vector.

1. The first case is colored red and $tan^{-1}\left(\frac{|C_L|}{C_D}\right) < \alpha$. The angle between the cavitator force vector and the velocity vector is less than that of the vehicle angle of attack and therefore the F_{cav} cavitator force vector is oriented above the vehicle centerline. This directionality of the force vector imparts a positive moment on the vehicle. The shown perturbation is a positive angle of attack, thus $\frac{\partial M_{cav}}{\partial \alpha} > 0$ and the positive moment will only increase the angle of attack and destabilize the vehicle.

2. The second case is green in color and $tan^{-1}\left(\frac{|C_L|}{C_D}\right) = \alpha$. The angle between the cavitator force vector and the velocity vector is exactly equal to that of the the vehicle angle attack. This places the cavitator force vector along the vehicle centerline, thus imparting no moment to the vehicle. This causes the vehicle to be marginally stable and essentially $C_{cav,m_\alpha} = 0$. Interestingly, using the disk cavitator hydrodynamic coefficient approximations presented in [4], which were reproduced in Equation (2.11), implies exactly this condition. It is worth noting that the cavitator force vector would slightly depart from the the vehicle centerline if the cavitator angle of attack differed from that of the vehicle angle of attack by virtue of a pitch rate q or cavitator deflection δ_c.

3. The third case is colored purple and $tan^{-1}\left(\frac{|C_L|}{C_D}\right) > \alpha$. The angle between the cavitator force vector and the velocity vector is larger than the vehicle angle of attack. The cavitator force vector F_{cav} becomes oriented below the vehicle centerline, creating a restoring moment on the vehicle and static stability is achieved ($C_{cav,m_\alpha} < 0$).

This qualitative analysis assumed that the cavitator was undeflected and thus perpendicular to the body centerline. In the trimmed vehicle case, the cavitator is deflected in order to provide a portion of the lift on the vehicle. This qualitative analysis can still provide insight for the case that the cavitator deflection is very

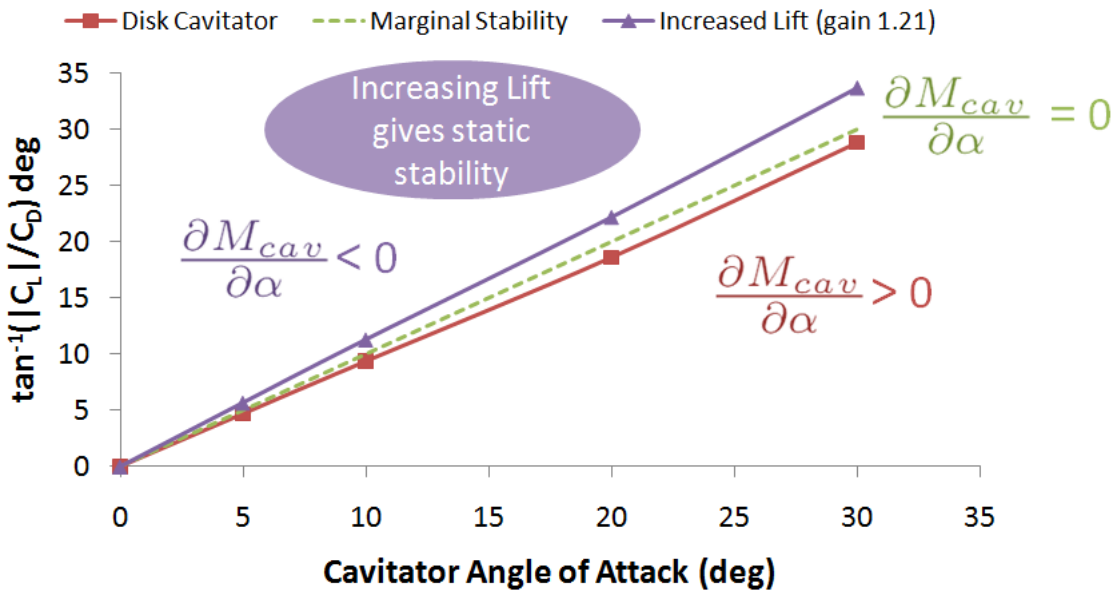

Figure 3.5: Disk Cavitator force vector orientation and implications for static stability

small, as is the case in the non-planing trim condition where the cavitator deflection is on the order of -2^o.

This analysis showed that the relation between the angle $tan^{-1}\left(\frac{|C_L|}{C_D}\right)$ and the vehicle angle of attack α is important. Reference [6] was quoted in Section 2.3, stating that from a hydrodynamicist's standpoint the tangential force on the cavitator is negligible compared to the normal pressure force acting on the cavitator. By this approximation, the force vector of the cavitator will be oriented normal to the face of the cavitator, implying that $tan^{-1}\left(\frac{|C_L|}{C_D}\right) = \alpha_c$. This approximation was tested by using the experimental hydrodynamic coefficients for the disk cavitator from [6] to calculate $tan^{-1}\left(\frac{|C_L|}{C_D}\right)$ and plot it against the cavitator angle of attack. The resulting plot is shown in Figure 3.5. A 45^o line would indicate that the $tan^{-1}\left(\frac{|C_L|}{C_D}\right) = \alpha_c$ and the two angles are equal. Points above the 45^o line indicate $tan^{-1}\left(\frac{|C_L|}{C_D}\right) > \alpha$, which corresponds to the stable condition from the qualitative analysis in Figure 3.4. The plot in Figure 3.5 shows that the disk cavitator leans on the side of instability and

ignoring the tangential force on the cavitator is contrary to a conservative assumption in terms of vehicle stability.

The effect of the disk cavitator lift coefficient magnitude on the sign of C_{cav,m_α} is further analyzed. The moment imparted on the vehicle by the cavitator is plotted as a function of the vehicle angle of attack in Figure 3.6 for a series of cavitators with varying lift coefficients. The nominal disk cavitator's lift coefficient resulted in a positive slope for the moment versus angle of attack plot. The lift coefficient of the disk cavitator was incrementally increased until the slope of the moment versus angle of attack plot became negative. Increasing the lift of the cavitator causes the switch in the sign of C_{cav,m_α}. The same figure shows that a certain lift coefficient exists which causes C_{cav,m_α} to be very close to zero. More exactly, a simple linear scaling of the lift coefficient will never make $C_{cav,m_\alpha} = 0$ over the range of angles of attack. This is because the disk cavitator drag coefficient, which has a quadratic dependence on angle of attack, also contributes to the moment imparted on the vehicle.

The static stability analysis has shown that the disk cavitator's lift coefficient is slightly too low for C_{cav,m_α} to be negative. This finding will be confirmed quantitatively. Consider a cavitator that generates 21% more lift than the disk cavitator. The angle $tan^{-1}\left(\frac{|C_L|}{C_D}\right)$ was also computed for the increased lift cavitator, and plotted against the cavitator angle of attack in Figure 3.5. The plot shows that the increased lift cavitator falls into the statically stable region where $C_{cav,m_\alpha} < 0$. The prediction that a cavitator with $C_{cav,m_\alpha} < 0$ would result in a statically stable vehicle is tested by trimming and linearizing the non-planing model using the increased lift cavitator at the same trim condition as was the vehicle with the nominal disk cavitator. Interestingly, rather than obtaining a stable vehicle, the instability shifts from the the natural frequency term to the vehicle damping term. More specifically, the original

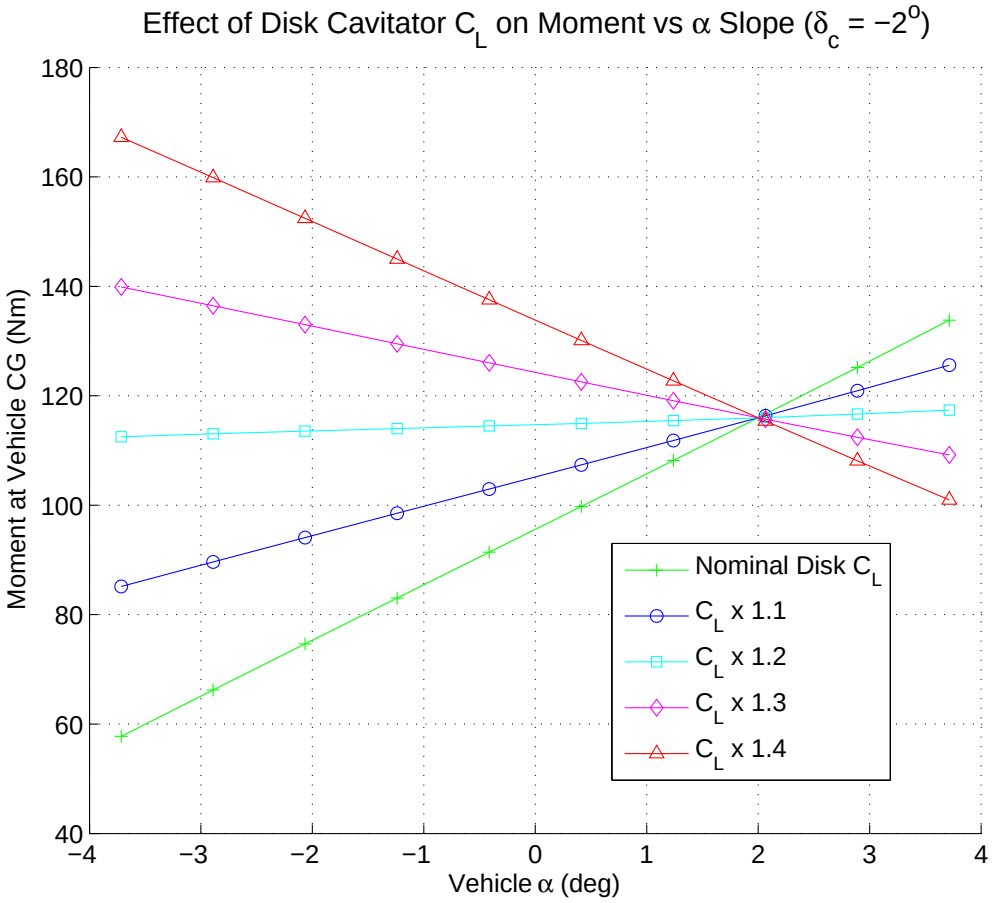

Figure 3.6: Increasing disk cavitator lift will change the sign of the moment versus α slope ($u = 77m/s, \sigma = 0.08$)

vehicle transfer function from cavitator input to pitch rate is

$$\frac{q(s)}{\delta_c(s)} = \frac{-530.7s}{(s^2 + 1.91s - 110.3)}$$

and the same transfer function for the increased lift cavitator is

$$\frac{q(s)}{\delta_c(s)} = \frac{-641.2s}{(s^2 - 0.006s + 0.35)} \tag{3.4}$$

Notice how the instability shifted from the natural frequency to the damping term. The vehicle with the nominal disk cavitator has positive damping but this is replaced with negative damping in the case of the hypothetical high lift cavitator. The reason for this switch can be explained by looking at the sources of damping for the vehicle. Before doing so, a qualitative discussion of how static stability would change for cone shaped cavitators is presented.

Effect of Cavitator Shape on Static Stability

The hydroynamic data on disk cavitators was obtained from [6]. Reference [6] also contains data on 15^o and 45^o half-angle cones. A comparison of the lift and drag coefficients of the disk and cone cavitators is shown in Figure 3.7. As was done in the case of the disk cavitator, the hydrodynamic coefficients for the 45^o cone and the 15^o cone can be fitted with polynomials as well. The Equations (2.12), (2.13), and (2.14) are again used for the polynomial approximations of drag, lift, and moment coefficients. The coefficients of the polynomial approximations for the 45^o cone are $k_1 = 0.5553$, $k_2 = 0.0002(180/\pi)^2$, $k_3 = 0.0015(180/\pi)$, and $k_4 = 0$. The polynomial approximations of the 15^o cone has coefficients $k_1 = 0.21$, $k_2 = -0.0001(180/\pi)^2$, $k_3 = -0.0171(180/\pi)$, and $k_4 = 0.0134(180/\pi)$. The cavitation number for the data of both cones is $\sigma = 0.1$. The polynomial approximation is valid within the range of

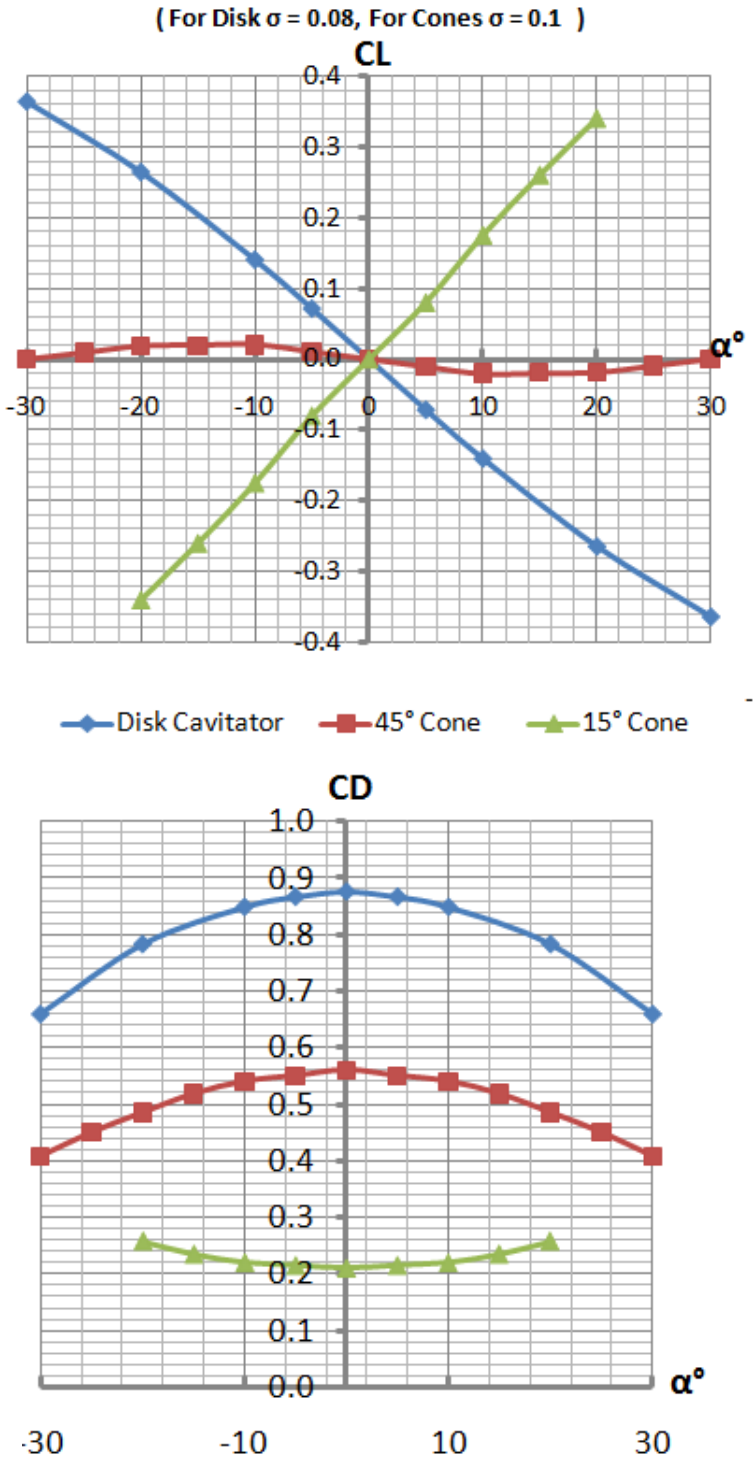

Figure 3.7: Comparison of lift and drag coefficients for various cavitator shapes [6]. Of the three shapes, the 15^o cone is the only shape with a non-zero moment coefficient.

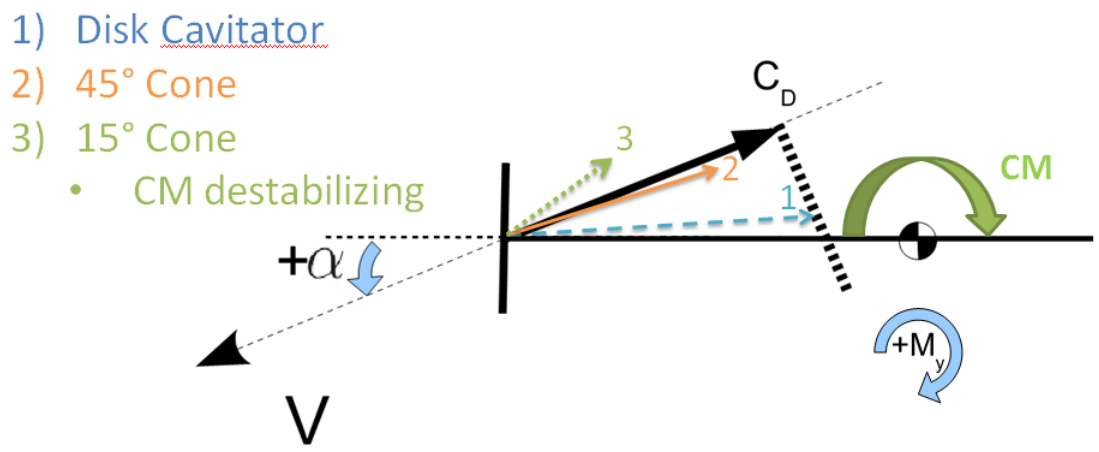

Figure 3.8: Comparison of cavitator force vector orientation and implications for static stability. Of the three shapes, the disk cavitator is the least destabilizing

$-15^o < \alpha_c < 15^o$ for the 45^o cone and $-20^o < \alpha_c < 20^o$ for the 15^o cone.

The various cavitator shapes have very different lift characteristics. The disk cavitator and the 15^o cone have very similar lift magnitudes with exactly opposite directionality. In comparison, the 45^o cone has relatively poor lift which can be understood from observing the pitched state of the cavitator. Deflecting the 45^o cone will give a slight increase in lift, but additional deflection makes the 45^o cone begin to look like an undeflected disk cavitator from the perspective of the free stream flow. This results in a very limited angle of attack range where lift is generated by the 45^o cone, with changes in the lift curve slope direction at about $\pm 15^o$.

The drag characteristics of the cavitators also vary. As one might expect, the disk cavitator has the greatest drag, followed by the 45^o cone and finally the 15^o cone. For small angles of attack, the drag coefficients can be approximated as constant for the three cavitators. The implications of these different lift and drag characteristics is analyzed in the following sections. In this section, the sole effect on static stability will be considered.

The same qualitative static stability analysis conducted for the disk cavitator can

be applied to the other cavitator shapes. This is shown graphically in Figure 3.8, with the disk, 45^o cone, and 15^o cone cavitator numbered one, two, and three.

1. The force vector of the disk cavitator is oriented slightly above the vehicle centerline, thus producing a small destabilizing moment.

2. The 45^o cone has very little lift. The cavitator drag is the primary contributor and results in the cavitator force vector being oriented very close to the direction opposite of the velocity vector. This causes a larger destabilizing moment than was the case for the disk cavitator.

3. The 15^o cone has an opposite lift direction than that of the disk cavitator. This orients the cavitator force vector above the negative velocity vector direction and creates an increased destabilizing moment. The 15^o cone also has a positive moment coefficient for positive angles of attack. In this example, this moment coefficient also contributes to further destabilizing the vehicle.

This qualitative analysis gives insight into the effect of cavitator shape on the static stability properties of the vehicle. For a more detailed quantitative analysis, a specific vehicle's trim condition should be analyzed. The detailed quantitative study is important because supercavitating vehicles most likely operate at small angles of attack. It may be the case that the destabilizing moment created by the disk cavitator compared to the 15^o cone are very similar and the difference lies within the band of uncertainty in the hydrodynamic coefficients.

It is clear from the cavitator comparison that the shape of the cavitator can deeply influence the vehicle dynamics. Considering that two simple cavitators, like the disk and the 15^o cone, have opposite lift curve slopes, it seems possible that other non-traditional cavitator shapes can be designed to have certain desirable characteristics. Two interesting cavitator shapes are shown in Figure 3.9. Research into

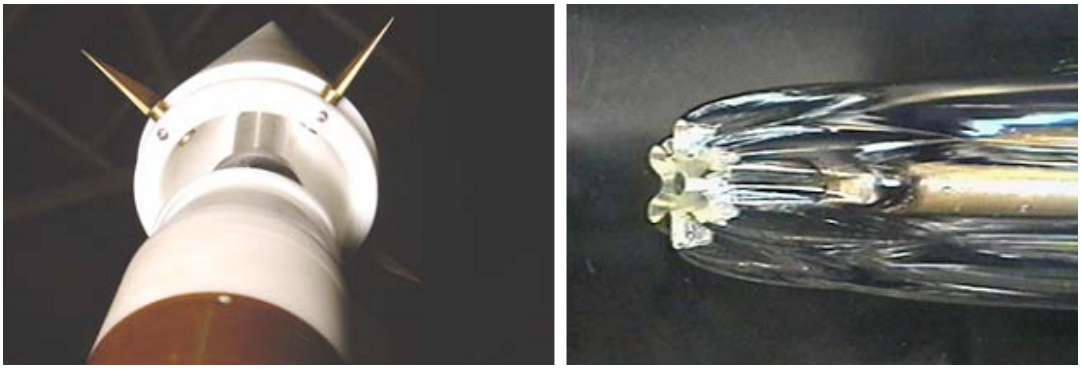

Figure 3.9: Two non-traditional cavitator shapes presented in [15]. The first (left) is a cone cavitator with augmented control surfaces and the second (right) is a snowflake shaped cavitator

Name	Definition	Non-Planing Value
C_{cav,z_α}	$\frac{1}{A\bar{q}}\frac{\partial F_{cav_z}}{\partial \alpha}$	-0.1507
C_{cav,z_q}	$\frac{1}{A\bar{q}}\left(\frac{u}{l_c}\right)\frac{\partial F_{cav_z}}{\partial q}$	0.1507
C_{cav,z_δ}	$\frac{1}{A\bar{q}}\frac{\partial F_{cav_z}}{\partial \delta}$	0.7254
C_{cav,m_α}	$\frac{1}{A\bar{q}l_c}\frac{\partial M_{cav}}{\partial \alpha}$	0.1507
C_{cav,m_q}	$\frac{1}{A\bar{q}}\left(\frac{u}{l_c^2}\right)\frac{\partial M_{cav}}{\partial q}$	-0.1507
C_{cav,m_δ}	$\frac{1}{A\bar{q}l_c}\frac{\partial M_{cav}}{\partial \delta}$	-0.7254

Damping

Damping

Figure 3.10: Terms of importance to determining the vehicle dynamic stability

non-traditional cavitator shapes are often motivated by factors other than the cavitator control properties. One example mentioned in [15] is increasing the cavitator surface area for fitting sensors within the cavitator.

3.1.2 Dynamic Stability

The nominal disk cavitator contributed to the static instability of the vehicle as discussed in Section 3.1.1. Furthermore, it was shown that a increased lift cavitator achieves static stability but loses the previously positive damping. In this section,

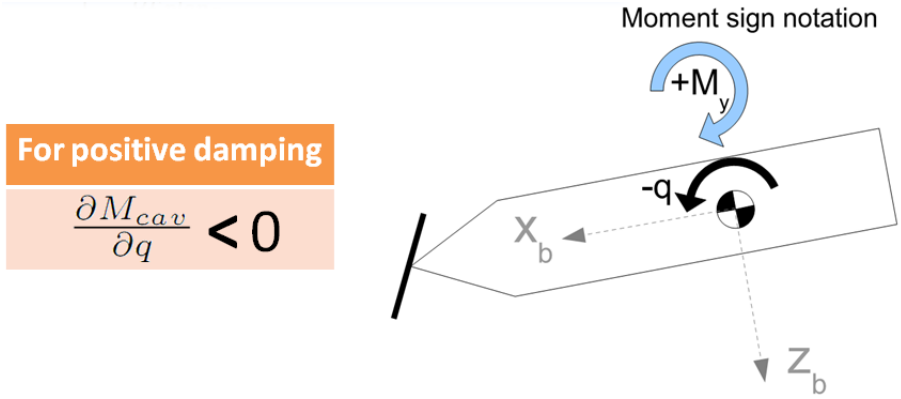

Figure 3.11: Sign notation for vehicle dynamic stability

the shift in instability from the natural frequency term to that of the damping term will be analyzed.

The terms which affect the vehicle damping are identified by symbolically computing the characteristic equation of the longitudinal state space model given in Equation (2.48). The characteristic equation of the non-planing vehicle is

$$s^2 + s2\zeta\omega_n + \omega_n^2 = s^2 + s(-a_{2,2} - a_{1,1}) + (a_{1,1}a_{2,2} - a_{1,2}a_{2,1})$$

where ζ is the damping ratio, ω_n the natural frequency, and $a_{i,j}$ refers to the entry in the i^{th} row, j^{th} column of the state matrix. Looking up the non-planing entries of the state matrix in Equation (2.48) and their numerical values in Equation (2.49), the damping term is given as

$$\begin{aligned} 2\zeta\omega_n &= -\frac{1}{I_{yy}}\frac{\partial M_{c_y}}{\partial q} - \frac{1}{u\,m}\frac{\partial F_{c_z}}{\partial \alpha} \\ &= 1.6 + 0.299 \end{aligned}$$

The dominant term that determines the sign of $2\zeta\omega_n$ for the non-planing vehicle is $\frac{1}{I_{yy}}\frac{\partial M_{c_y}}{\partial q}$. Thus referring to the non-dimensional stability derivatives in Table 3.1, the

sign of C_{m_q} greatly determines the damping of the non-planing vehicle. The following dynamic stability analysis will assume that the damping properties of the non-planing vehicle are determined by the sign on C_{m_q}. It will later be shown that this is not a valid assumption in the case of the planing vehicle.

The change in pitching moment due to pitch rate C_{m_q} must be negative for the vehicle to have positive damping. The main contributor to this damping in aircraft is the tail of the vehicle [14]. In the case of a non-planing supercavitating vehicle, the main damping contributor is the cavitator. If the vehicle has fins, the fins also contribute to the damping. Positive damping implies that any oscillations from a pitch disturbance would eventually subside and not be amplified. Thus for dynamic stability it is required that $C_{cav,m_q} < 0$. Looking at Figure 3.10, the non-planing trim condition meets that requirement and thus has positive damping. An understanding of why C_{cav,m_q} must be less than zero can be determined from Figure 3.11. In order to dampen a negative pitch rate, a positive moment must be applied by the vehicle.

The question remains as to why the instability shifted from the natural frequency term to that of the damping term when the lift of the cavitator was increased to obtain static stability. This is best understood using a figure similar to Figure 3.4, but this time drawn to understand what cavitator force vector orientation would be best for positive damping (Figure 3.12). The vehicle is given a negative pitch rate, which induces a positive angle of attack at the cavitator. Depending on the magnitude of the lift coefficient of the cavitator, there are three possible cases

1. The first case is colored red and $tan^{-1}\left(\frac{|C_L|}{C_D}\right) < \alpha$. The F_{cav} force vector is oriented above the vehicle centerline. This directionality of the force vector imparts a positive moment to the vehicle, dampening the original negative pitch rate perturbation.

2. The second case is green in color and $tan^{-1}\left(\frac{|C_L|}{C_D}\right) = \alpha$. The cavitator force

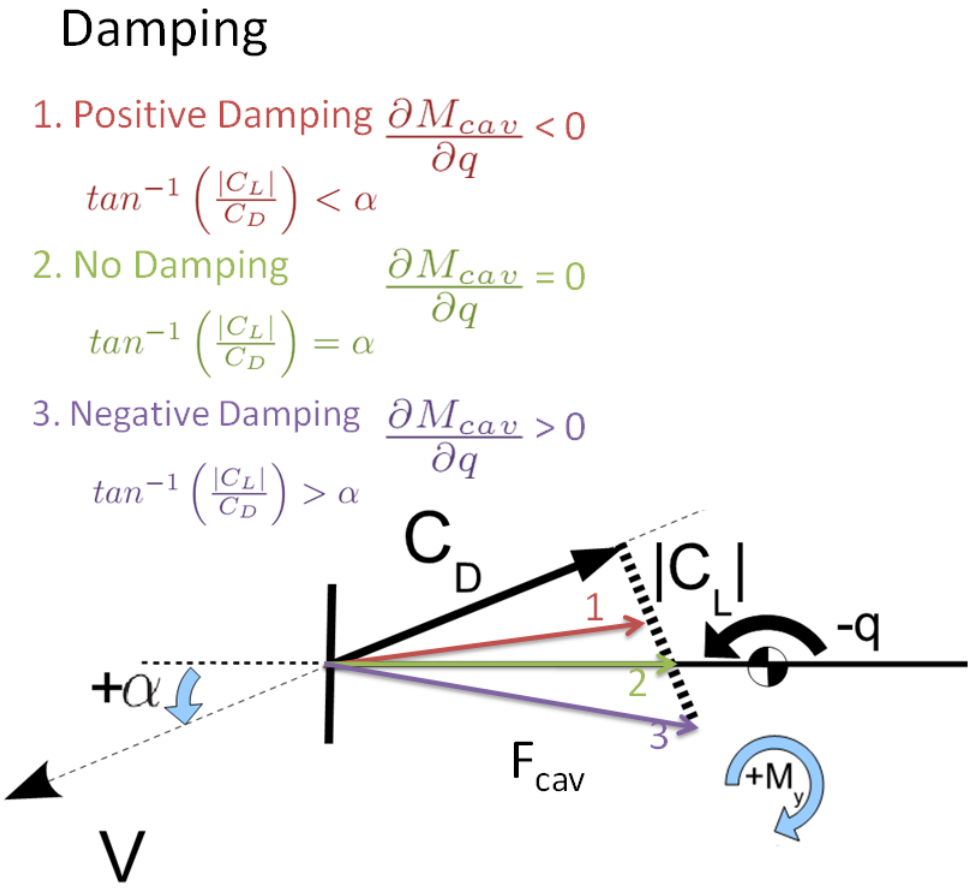

Figure 3.12: Dynamic stability of disk cavitator, angles exaggerated purposely

vector is along the vehicle centerline, thus imparting no moment to the vehicle. No moment is imparted to the vehicle and thus there is zero damping to counter the negative pitch rate perturbation.

3. The third case is colored purple and $tan^{-1}\left(\frac{|C_L|}{C_D}\right) > \alpha$. The angle between the cavitator force vector and the velocity vector is larger than the vehicle angle of attack. The cavitator force vector F_{cav} becomes oriented below the vehicle centerline, creating a negative moment on the vehicle, further increasing the magnitude of the negative pitch rate perturbation and destabilizing the vehicle.

Among the three listed cases, case one provides positive damping to the vehicle. Using the nominal cavitator, the vehicle matches case one and thus it makes sense that the damping term ($2\zeta\omega_n$) in the cavitator to pitch rate transfer function is positive. It also makes sense that if the lift is increased to achieve static stability, then the switch to case three becomes detrimental to damping, giving the vehicle negative damping ($2\zeta\omega_n < 0$). The shift in instability observed in the transfer functions can be understood from this analysis.

The cavitator is the sole contributor to the moment on the vehicle, with the exception of the thrust vectoring whose moment does not depend on the vehicle state. Thus a trade-off is observed between static stability and damping for the assumed vehicle configuration using the disk cavitator. A similar analysis could be conducted if fins were included on the vehicle.

3.1.3 Control Implications

The desirability of having positive damping at the cost of losing static stability or vice versa has implications for the control design of the vehicle. This will be studied by comparing the dynamics of the nominal disk cavitator vehicle, which has positive damping but is statically unstable, to that of the increased lift cavitator vehicle which

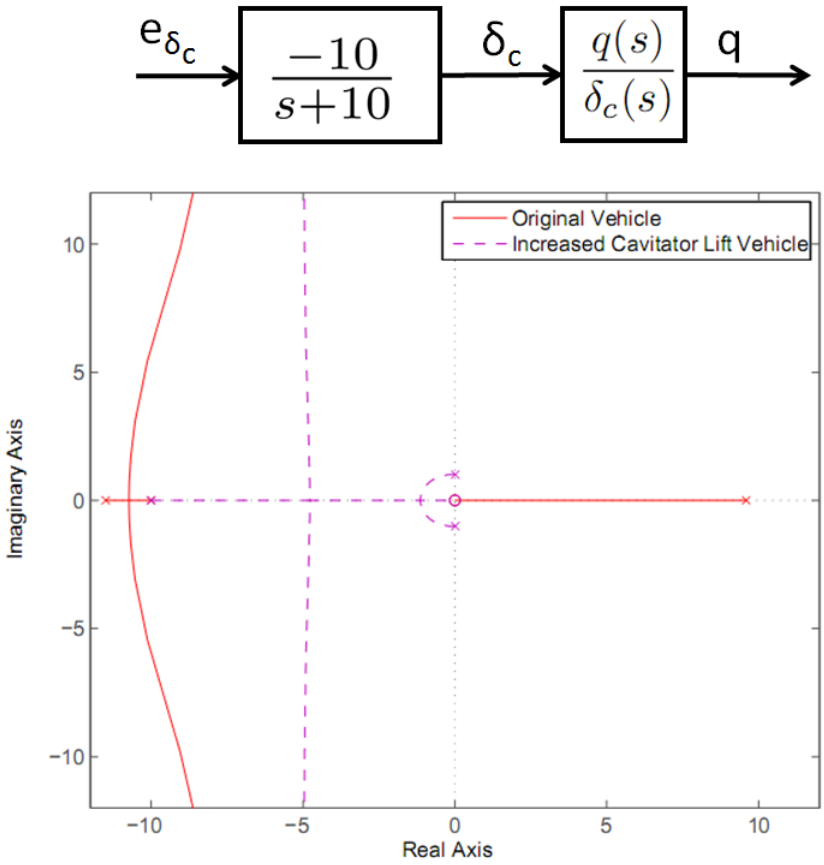

Figure 3.13: Root locus plot comparing dynamics of nominal disk cavitator and the increased lift cavitator vehicle using pitch rate feedback

has the opposite stability properties. The transfer functions for cavitator input to pitch rate output are given in Equation (3.3) and (3.4) respectively. In both cases the vehicle is unstable, though the source of the instability differs.

The first step in control design, before a pitch orientational control system can be designed for pitch tracking, is to use feedback to stabilize the vehicle. As is commonly done in aerospace vehicle control, it will be attempted to use a pitch rate feedback inner loop to stabilize the vehicle. Furthermore, pitch rate is a commonly available, accurate, and low noise sensor measurement for feedback. Assuming a proportional gain on the pitch rate feedback, it will be attempted to stabilize both

vehicles. Whether proportional gain is sufficient to move all the system poles to the left half-plane is nicely observed by plotting the root locus. The root locus plot for both vehicles are drawn in Figure 3.13. First order actuator dynamics are also included in this analysis.

The root locus plots reveal that in the case of the original vehicle which had positive damping but was statically unstable, a pitch rate feedback inner loop is insufficient to stabilize the system. In the case of the increased lift vehicle which was statically stable but had negative damping, the pitch rate feedback is sufficient to stabilize the system. Pitch rate feedback in effect increases the damping of the vehicle pitch dynamics [14]. The original vehicle already had positive damping and using pitch rate feedback was unable to overcome the static instability. On the other hand, the increased lift cavitator vehicle started off with static stability and only lacked damping. Thus the pitch rate feedback was able to provide the damping to stabilize the system effectively.

3.2 Planing Condition

The trim condition for the planing vehicle, Table 2.2, uses planing to support the aft end of the vehicle and balance the lift of the cavitator. In this case, the planing lift force results in approximately $50N$ of drag which must be compensated for by additional thrust. The reason the planing and the non-planing trim conditions have very similar T_x values is because the planing condition is trimmed at a slightly smaller velocity, $u = 76.3m/s$. Trimming both vehicles at $u = 77m/s$, the planing condition requires approximately $50N$ of additional thrust to overcome the drag from planing.

The transfer function of the planing vehicle from cavitator input to the vehicle's

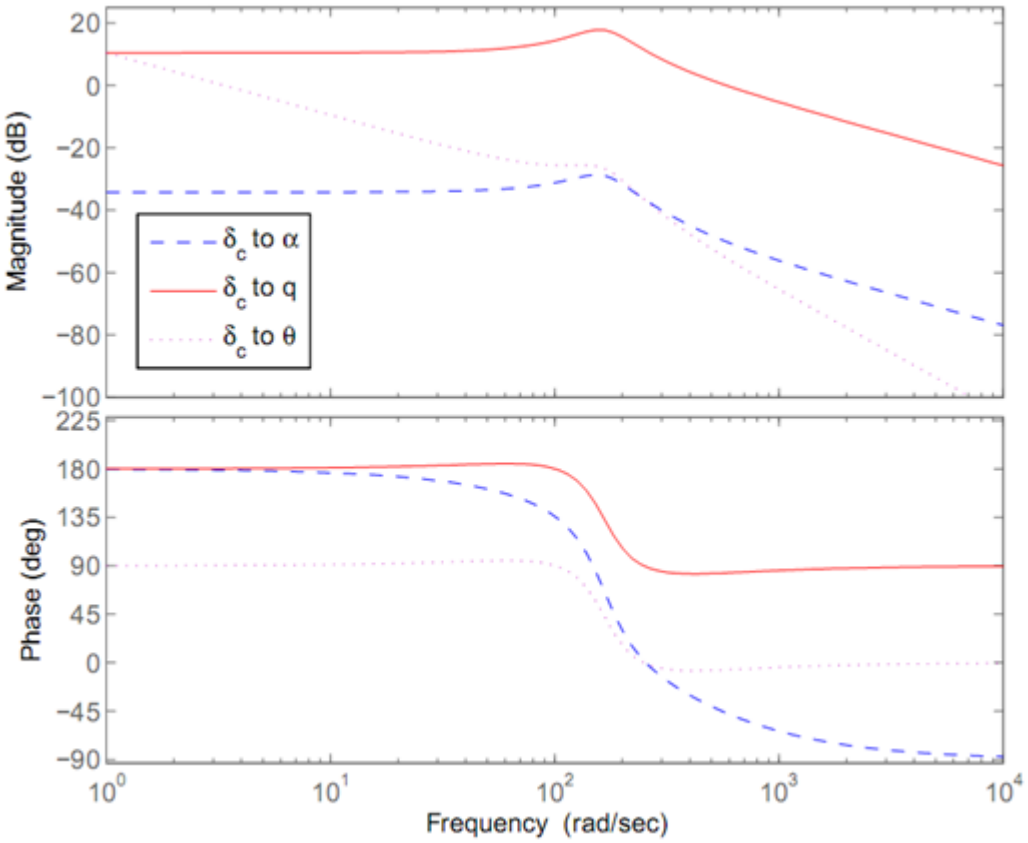

Figure 3.14: Planing vehicle Bode plot

angle of attack and pitch rate are

$$\frac{\alpha(s)}{\delta_c(s)} = \frac{1.43(s - 376.6)}{s^2 + 98.4s + 27860} \tag{3.5}$$

$$\frac{q(s)}{\delta_c(s)} = \frac{-519.5s(s + 178)}{s^2 + 98.4s + 27860} \tag{3.6}$$

As opposed to the non-planing trim condition, the planing trim condition is stable with two complex poles at $-49.2 \pm 159.5i$. The Bode response of the planing vehicle is shown in Figure 3.14. The planing vehicle has very poor control authority to affect the vehicle angle of attack using the cavitator as compared to the non-planing vehicle Bode response, shown in Figure 3.1. The other noticeable difference is that the cavitator can affect the pitch rate of the planing vehicle at steady state. This was not possible in the non-planing vehicle because of the zero at the origin limiting the ability of the cavitator in affecting pitch rate to higher frequencies only. The change that occurs for the vehicle to be stable in the planing trim condition will be analyzed. Initially, the static stability and dynamic stability terms will be revisited.

3.2.1 Static Stability

There are two terms that together make up the partial derivative of the moment with respect to angle of attack, as shown in Figure 3.15. Both the cavitator and the planing contribution will affect static stability. The cavitator contribution, C_{cav,m_α}, changes only slightly from its unstable positive value that was discussed in Section 3.1.1. The planing contribution, C_{plan,m_α}, is more than an order of magnitude larger than the cavitator term and is negative. It is more appropriate to compare the magnitudes of the dimensional form of the partial derivatives. The static stability contribution of the cavitator is $\frac{\partial M_{cav}}{\partial \alpha} = 566N/rad$, and the contribution of planing is $\frac{\partial M_{plan}}{\partial \alpha} = -143530N/rad$. This allows planing's stabilizing characteristics to overcome any

Name	Definition		Non-Planing Value	Planing Value
C_{cav,z_α}	$\frac{1}{A\bar{q}}\frac{\partial F_{cav_z}}{\partial \alpha}$	Damping	-0.1507	-0.1527
C_{cav,z_q}	$\frac{1}{A\bar{q}}\left(\frac{u}{l_c}\right)\frac{\partial F_{cav_z}}{\partial q}$		0.1507	0.1527
C_{cav,z_δ}	$\frac{1}{A\bar{q}}\frac{\partial F_{cav_z}}{\partial \delta}$		0.7254	0.7223
C_{cav,m_α}	$\frac{1}{A\bar{q}l_c}\frac{\partial M_{cav}}{\partial \alpha}$	Static Stability	0.1507	0.1527
C_{cav,m_q}	$\frac{1}{A\bar{q}}\left(\frac{u}{l_c^2}\right)\frac{\partial M_{cav}}{\partial q}$	Damping	-0.1507	-0.1527
C_{cav,m_δ}	$\frac{1}{A\bar{q}l_c}\frac{\partial M_{cav}}{\partial \delta}$		-0.7254	-0.7223
C_{plan,z_α}	$\frac{1}{D_{body}^2\bar{q}}\frac{\partial F_{plan_z}}{\partial \alpha}$	Damping	-	-5.700
C_{plan,z_q}	$\frac{1}{D_{body}^2\bar{q}}\left(\frac{u}{l_p}\right)\frac{\partial F_{plan_z}}{\partial q}$		-	0.1068
C_{plan,m_q}	$\frac{1}{D_{body}^2\bar{q}}\left(\frac{u}{l_p^2}\right)\frac{\partial M_{plan}}{\partial q}$	Damping	-	0.1068
C_{plan,m_α}	$\frac{1}{D_{body}^2\bar{q}l_p}\frac{\partial M_{plan}}{\partial \alpha}$	Static Stability	-	-5.700

Figure 3.15: Terms affecting static and dynamic stability of the planing vehicle

instability from the cavitator on the vehicle.

The stabilizing contribution of planing to static stability can be understood by looking at Figure 3.16. The vehicle is perturbed from an initial planing trim condition. The force and moment contribution of planing attempts to return the vehicle to the initial trim condition. An opposite counter clockwise perturbation can also be visualized. In that case the planing force would diminish, again attracting the vehicle back towards the equilibrium condition.

3.2.2 Dynamic Stability

It was shown in Section 3.1.2 that the characteristic equation of the vehicle can be written in terms of the entries of the vehicle state matrix of the two state linear model. The second order characteristic equation's damping term for the planing vehicle is

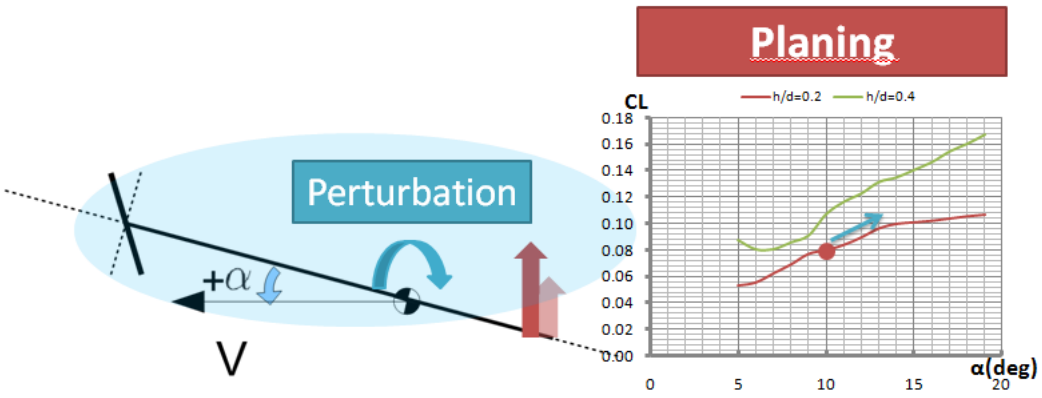

Figure 3.16: Qualitative example showing planing's contribution to vehicle static stability

$$
\begin{aligned}
2\zeta\omega_n &= -\frac{1}{I_{yy}}\left(\frac{\partial M_{c_y}}{\partial q}+\frac{\partial M_{p_y}}{\partial q}\right)-\frac{1}{u\,m}\left(\frac{\partial F_{c_z}}{\partial \alpha}+\frac{\partial F_{p_z}}{\partial \alpha}\right)\\
&= -4.1+102.4
\end{aligned}
$$

The dominant term that determines the sign of $2\zeta\omega_n$ for the planing vehicle is $\frac{1}{u\,m}\left(\frac{\partial F_{c_z}}{\partial \alpha}+\frac{\partial F_{p_z}}{\partial \alpha}\right)=\frac{1}{u\,m}(-504-171440)$. Clearly the planing term $\frac{\partial F_{p_z}}{\partial \alpha}$, written non-dimensionally as C_{plan,z_α}, dominates and essentially determines the damping property of the planing vehicle. This is contrary to the non-planing vehicle, where the partial derivative of the moment with respect to pitch rate determined the vehicle damping. This explains why $C_{plan,m_q}>0$, yet the planing vehicle damping is positive.

Although the partial derivative of the moment with respect to pitch rate has little effect on the overall vehicle damping, the cavitator and planing contribution to this derivative are briefly analyzed. The cavitator contribution, $C_{cav,m_q}=-0.1527$, is stabilizing and very similar to the value in the non-planing condition. On the other hand, the planing contribution C_{plan,m_q} is positive and thus has a destabilizing effect on the dynamic stability of the vehicle. In the most simple case, the planing force

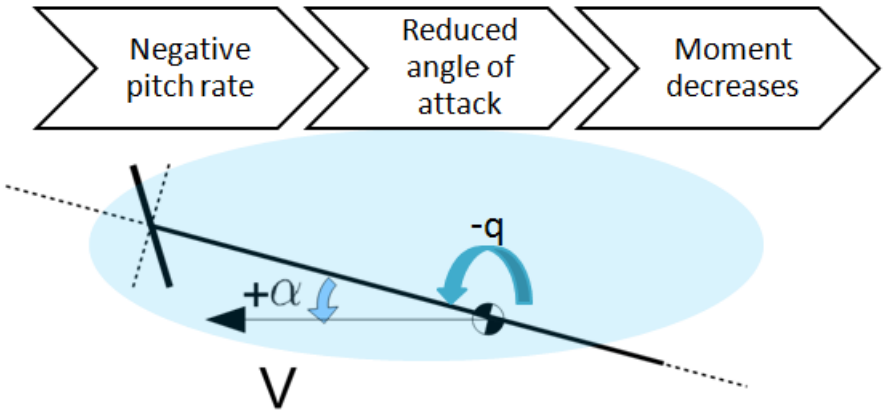

Figure 3.17: In a planing condition, a negative pitch rate causes the moment to decrease. Thus $C_{plan,m_q} > 0$

depends on the angle between the body and the cavity at the location of planing. In a dynamic scenario, this angle would be changing in a complicated fashion. As the body pitches, the cavity which is formed by the cavitator will also be changing shape. The cavity shape itself has complex pulsating dynamics which has largely been ignored in this thesis. Recognizing these complex interactions, a simple analysis is still conducted to give a possible explanation of why $C_{plan,m_q} > 0$ in this model.

The positive planing angle between the body and the cavity is approximated as the absolute value of the angle of attack at the nose of the vehicle and is given in Equation (2.27). In Figure 3.17, a planing vehicle is shown with a negative pitch rate perturbation. The negative pitch rate causes the angle of attack at the cavitator to be reduced. The reduced angle causes the magnitude of the planing moment to also decrease, thus $C_{plan,m_q} > 0$.

It was shown earlier that terms other than C_{m_q}, namely C_{plan,z_α} largely determine the vehicle damping. A qualitative analysis showing why $C_{plan,z_\alpha} < 0$ is conducted again using Figure 3.16. As the vehicle angle of attack increases, the aft end of the vehicle immerses further into the cavity wall. This causes the planing lift force to increase, which translates into a negative *z-body* force. Therefore $C_{plan,z_\alpha} < 0$, and

it makes intuitive sense that planing force is very great and largely determines the planing vehicle dynamics.

The cross-coupling between states and inputs tends to complicate the system relatively quickly. Nevertheless where possible, simplified qualitative examples linking the observed dynamics to the vehicle physical characteristics can assist understanding the connections between the the physical vehicle and the associate control challenges.

Chapter 4

Other Trade-off Studies

4.1 Planing and Fins

The cavitator provides lift at the nose of the vehicle, which imparts a force induced moment on the vehicle which must be balanced. Countering the lift moment by a force at the tail of the vehicle is one method of balancing the vehicle pitch dynamics. The force at the tail of the vehicle may be provided by several means. Initially thrust vectoring was used when studying the non-planing vehicle. Though theoretically possible, the challenges of controlling the thrust vector may make this option complicated and difficult to implement.

A second means of supporting the aft end of the vehicle is to use planing. The impingement of the body on the cavity wall naturally creates a restoring force on the tail of the vehicle. Furthermore, the simplicity of this supporting mechanism makes it attractive. Utilizing planing to support the vehicle, and possibly using planing to the advantage of the vehicle by inducing planing to assist maneuvering would require no additional hardware to be installed on the vehicle. Instead a deeper understanding of the cavity dynamics as well as possibly a complex sensory package to determine the location of the body within the cavity may be required.

A third option is the addition of fins to the tail of the vehicle. Compared with

planing, the fins would provide direct control authority on the vehicle. In comparison to fins on traditional underwater vehicles, an additional level of complexity is added to the fins because they are partially within the cavity. Movement of the body with respect to the cavity causes the fins to pull in and out of the cavity wall, affecting the wetted area of the fins. Furthermore, the fins may also supercavitate, affecting their lift characteristics as well as the ventilation required to maintain the cavity around the vehicle.

It is important to understand the different drag values associated with supporting the tail of the vehicle with planing or fins. A drag study was conducted on the planing trim condition presented in Table 2.2. In this condition, the tail of the vehicle has an immersion ratio of $\frac{h}{D_{body}} = 0.0113$, and the angle between the vehicle and the cavity is $\alpha_{cb} = 0.0123 rad$. Using Equations (2.24) and (2.23), the planing lift and drag coefficients are 0.0041 and 0.0014 respectively. This results in a planing lift force of 123 Newtons and an associated drag of 43 Newtons.

Using hydrodynamic experimental data on wedge fins from [16], the same lift necessary to support the vehicle can be provided by fins and the associated drag analyzed. Adhering to the notation used in [16], which is reproduced in Figure 4.1, two fins are assumed to be mounted on the tail of the vehicle. It is assumed initially that the fins have a span and chord of $b = c = 3\,inches$ each. In actuality the physical fins would be slightly larger to account for *lost* surface area between the vehicle body and the cavity wall. The two fins would each provide half of the planing lift. Thus the necessary lift coefficient of each fin can be calculated as

$$C_{Lf} = \frac{1}{2}\left(\frac{123N}{\bar{q}\,S}\right) = 0.0036$$

where $S = bc$. Interpreting the angle of attack associated with the required lift, as well as checking if the intial size of fin was reasonable requires the lift and drag

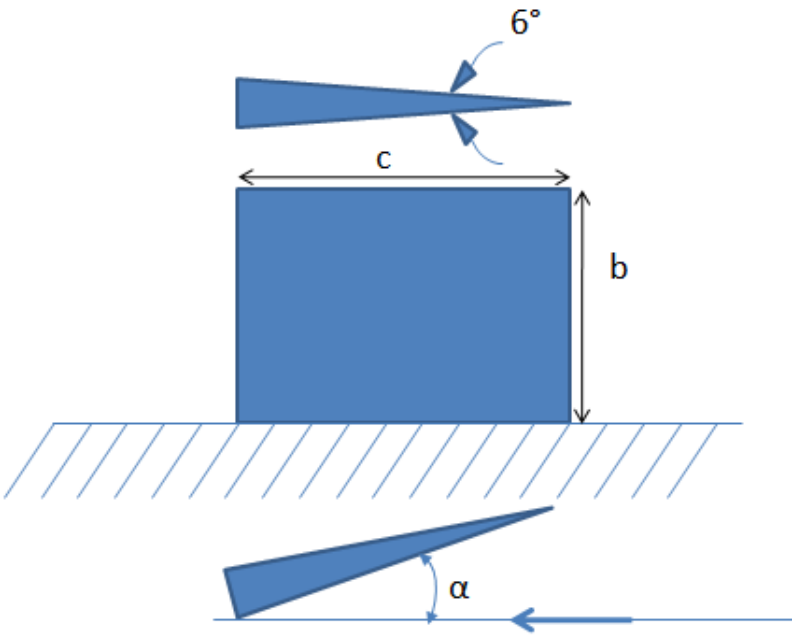

Figure 4.1: Wedge fins notation used in [16]

coefficient data for the fin shown in Figure 4.2. The zero lift and minimum drag angle of attack occurs at $\alpha_{fin} = 3^o$ instead of zero degrees because the angle is measured from the lower surface of the wedge profile, as was shown in Figure 4.1. The C_{Lf} required occurs at a very low angle of attack, and the initial fin size should be reduced. Additionally, the associated combined drag ($C_{Df} = 0.015$) for the fins in this case is 507 Newtons, which is an order of magnitude greater than the drag from planing.

A substantial reduction in fin size, $b = c = .5\,inches$, results in $C_{Lf} = 0.13$ which corresponds to a fin deflection of 2^o from the zero lift point. The corresponding drag coefficient would be $C_{Df} = 0.015$ for the two fins which leads to a drag force of 14 Newtons.

Several important characteristics of wedge shape fins are identified by this case study. First is that, compared to the body dimensions, the wetted fin area necessary

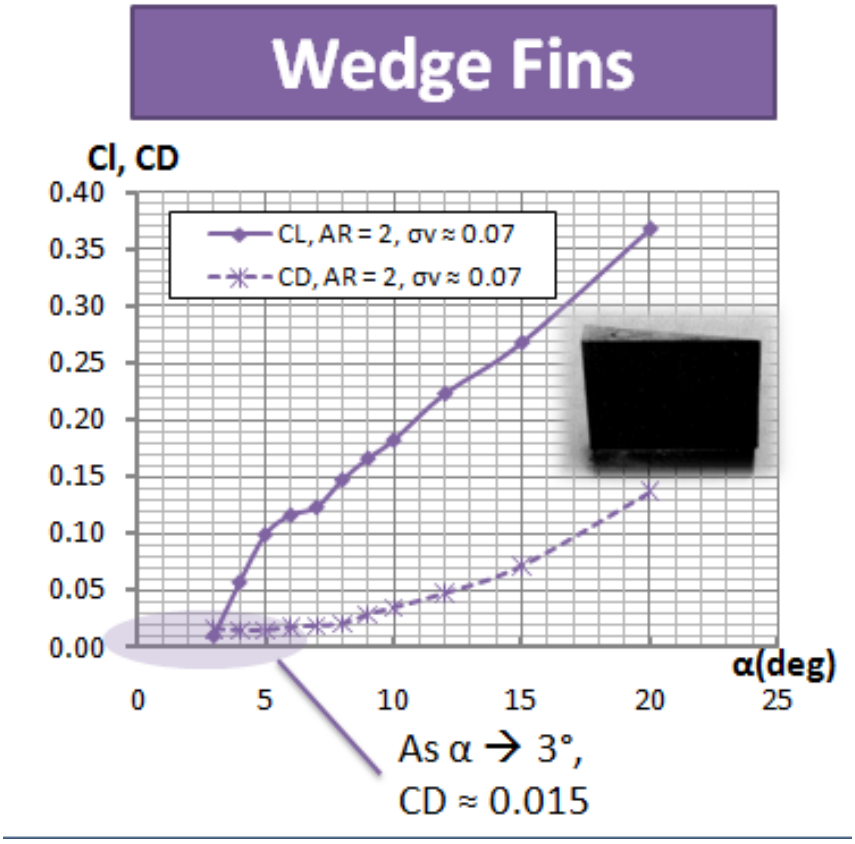

Figure 4.2: Plot of wedge fin lift and drag coefficient as a function of fin angle of attack for a low cavitation number, based on [16] and picture of fin used in experiment

to lift the vehicle is very small. Smaller fins definitely have less weight, but building small fins that can support the required loading conditions is structurally challenging. Additionally, if such a small wetted area is required by the fins, then small vehicle perturbations with respect to the cavity would have very large effects on changing the wetted area of the fins. This would pose a very serious challenge.

Figure 4.2 reveals that using a larger fin at a lower angle of attack to trim the vehicle is very costly in terms of drag. The fin drag coefficient is relatively constant for $0 \rightarrow 5^o$ deflection from the zero lift point. Minimizing the wetted area of the fin necessary to produce the required lift is very beneficial. A smaller fin, with a larger deflection, would provide the required lift with little or no increase in drag. The reduced wetted area with the same drag coefficient can minimize the drag created by the fins.

4.1.1 Fin Aspect Ratio

Using the fin geometry notation presented in Figure 4.1, the fin aspect ratio is defined as $AR = \frac{2b}{c}$. In the previous analysis, the fin aspect ratio was maintained at $AR = 2.0$. Under cavitating flow conditions, fin geometries with larger aspect ratio's increase the lift coefficient of the fin [16]. An additional qualitative property of high aspect ratio fins can be deduced from analyzing the fin environment. A fin mounted onto the vehicle will be partially immersed into the cavity wall, and this immersed length of the fin will be generating lift. In the event of a perturbation of the cavity location with respect to the vehicle, the movement will cause the immersed length of the fin to change. In the case of a high aspect ratio fin, the change in immersed fin surface area would be less than in that of a low aspect ratio fin. This is shown visually in Figure 4.3. This means that the higher aspect ratio fin would be more robust to the effect of cavity perturbations on the fin lift.

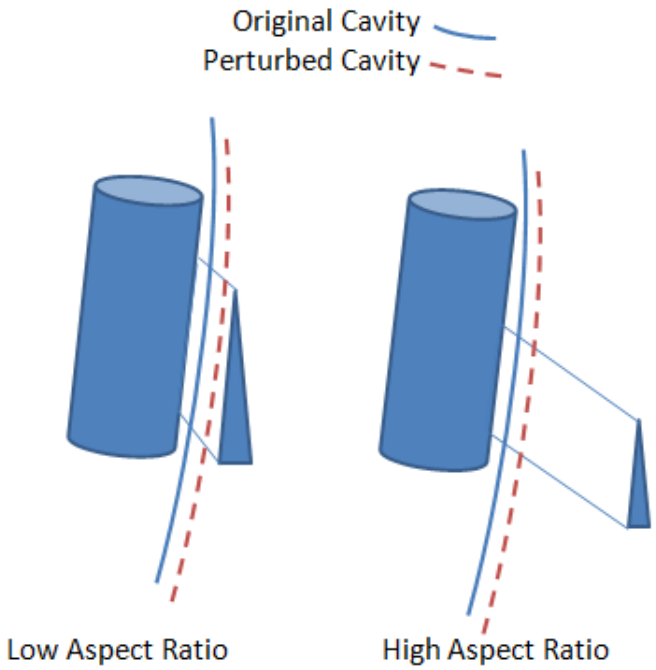

Figure 4.3: Cavity perturbation has smaller affect on wetted length of the fin with a higher aspect ratio

4.2 Cavitator Shape and Vehicle Dynamics

In Section 3.1.1 the effect of cavitator shape on the static stability of the non-planing vehicle was studied. Though none of the three cavitator shapes resulted in static stability for the non-planing vehicle, qualitatively it was shown that the disk cavitator was the least destabilizing, followed by the 45^o cone and finally the 15^o cone was the most destabilizing. In this section, the effect of the cavitator shape on the vehicle dynamics will be analyzed in more detail, in many ways confirming the qualitative analysis previously conducted.

4.2.1 Drag

The choice of cavitator shape on the vehicle drag is an important consideration. The cone shaped cavitators would seemingly reduce the drag when compared to the disk cavitator. This is confirmed by comparing the drag coefficients for the three cavitator shapes, as is shown in Figure 3.7. The equation for cavitator drag is given as

$$
\begin{aligned}
D_c &= C_{Dc}\bar{q}_c A_c \\
\bar{q}_c &= \frac{1}{2}\rho V_c^2 \\
A_c &= \frac{\pi}{4} d_c^2
\end{aligned}
$$

where in the case of the cones, d_c is the base diameter. In order to conduct a fair comparison, each cavitator shape is sized such that all three generate the same cavity dimensions. The cavity dimensions of interest are the cavity maximum diameter (d_m) and the cavity length (L_{cavity}). The Reichardt theoretical formula for the non-

dimensional maximum cavity diameter is given in [5] as

$$\frac{d_m}{d_c} = \left(\frac{C_{Dc}}{\sigma - 0.132\sigma^{8/7}} \right)^{1/2} \tag{4.1}$$

Also based on Reichardt's derivations is the equation for the cavity length. As presented in [5], the non-dimensional cavity length is

$$\frac{L_{cavity}}{d_c} = \frac{\sigma + 0.008}{\sigma(0.066 + 1.7\sigma)} \left(\frac{C_{Dc}}{\sigma(1 - 0.132\sigma^{1/7})} \right)^{1/2} \tag{4.2}$$

Equations (4.1) and (4.2) can be applied for the three cavitator shapes. Interestingly, the equations only depend on the cavitator drag coefficient, diameter, and the cavitation number. In all three cases, the cavitation number are assumed constant and equal. It is stated in [5], and the equations confirm, that $C_{Dc}A_c$ of all three cavitator shapes must be equal in order for d_m and L_{cavity} to be the same. This implies that the cone cavitators must be sized such that they generate the same drag as the disk cavitator. It is the cavitator drag that largely determines the cavity dimensions. Thus, there is no benefit in terms of drag reduction for using a different shape cavitator. In order to generate equivalent cavity dimensions, there must be equivalent drag.

It should be pointed out that although the cavitators are sized to generate equal d_m and L_{cavity}, the cavity outlines will differ and depend on the shape of the cavitator. This is especially true of the frontal portion of the cavity [5].

The cavitator drag coefficients are relatively constant for small angles of attack. In both Equations (4.1) and (4.2), it shall be assumed that $C_{Dc} \approx C_{Dc}|_{\alpha=0}$. The nominal vehicle configuration using the disk cavitator has $C_{Dc}A_c = \frac{\pi(0.0381m)^2}{4}(0.875) = 9.9758E^{-4}m^2$. Utilizing the respective $C_{Dc}|_{\alpha=0}$ for each cone cavitator, the diameter d_c required to match the disk cavitator $C_{Dc}A_c$ is calculated and shown in Table 4.1.

Interestingly, the diameter required for the 15^o cone cavitator is more than double

Vehicle Cavitator Sizes

Cavitator Shape	$C_{Dc}\|_{\alpha=0}$	d_c
disk	0.875	0.0381 m
45^o cone	0.555	0.0478 m
15^o cone	0.21	0.0778 m

Table 4.1: Cavitator sizes required to match the nominal vehicle disk cavitator $C_{Dc}A_c$. These size cavitators all create the same cavity dimensions d_m and L_{cavity}

Disk Cavitator		45^o **Cone**		15^o **Cone**	
Name	Value	Name	Value	Name	Value
u	77 m/s	u	77 m/s	u	77 m/s
w	0 m/s	w	0 m/s	w	0 m/s
q	0 rad	q	0 rad	q	0 rad
θ	0 rad	θ	0 rad	θ	0 rad
δ_c	-0.0404 rad	δ_c	-0.2152 rad	δ_c	0.0069 rad
T_x	2953.7 N	T_x	2795.4 N	T_x	2957.5 N
T_z	-117.119 N	T_z	-117.119 N	T_z	-119.941 N

Table 4.2: Trim conditions for non-planing non-linear 3 DOF equations for disk, 45^o, and 15^o cone cavitators. In all cases, $\sigma = 0.08$ and the polynomial approximations of the hydrodynamic coefficients are used

the diameter of the disk cavitator. From this comparison, one can obtain a rule of thumb for supercavitating vehicle nose design. When a smaller profile nose is required, bluntly shaped cavitators with greater drag must be considered.

4.2.2 Non-Planing

The three cavitator shapes with their respective dimensions were used to trim the vehicle in a non-planing condition. The three trim conditions are presented in Table 4.2. The slight difference in T_x for the three cases can be attributed to the $C_{Dc} \approx C_{Dc}|_{\alpha=0}$ approximation. The positive lift curve slope of the 15^o cone resulted in a positive cavitator pitch to trim the vehicle. Additionally, a slightly larger T_z is required for the 15^o cone cavitator to counter act the destabilizing moment coefficient, which is

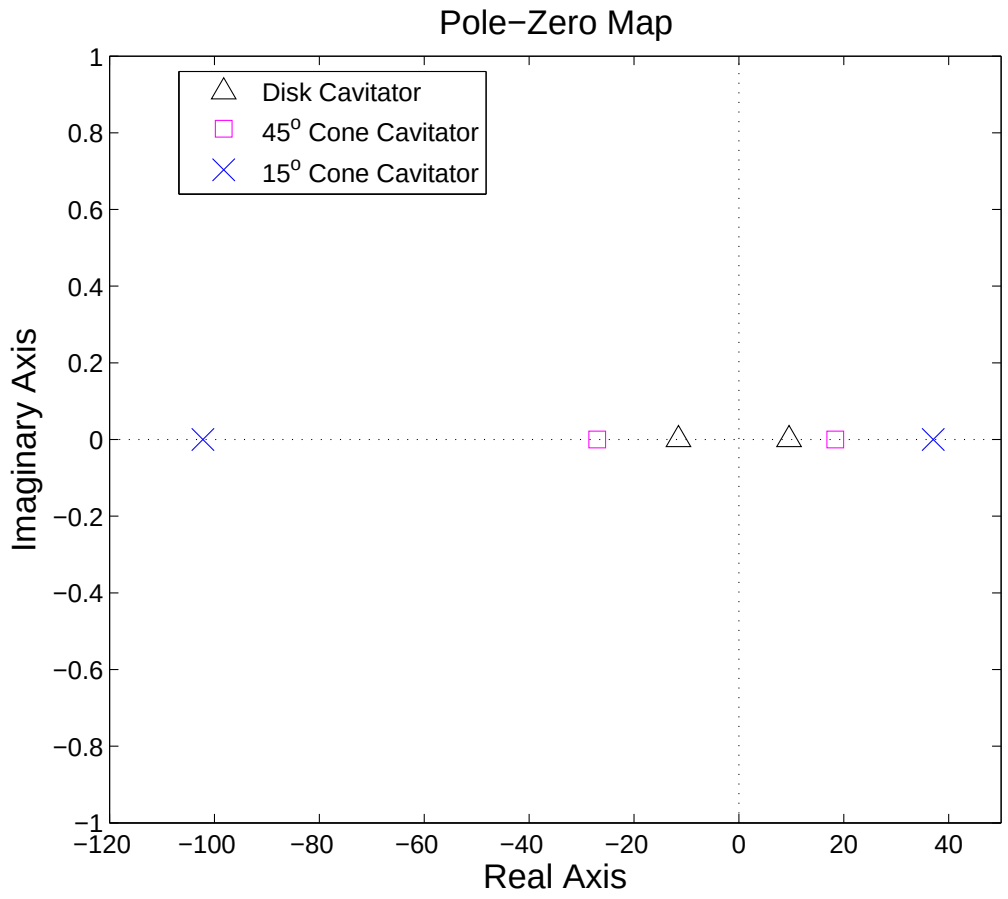

Figure 4.4: The location of the vehicle poles changes for different cavitator shapes on the non-planing vehicle

not present for the disk or 45^o cone.

The 3 DOF non-linear equations of motion are linearized at the three trim conditions, providing linear models for each of the cavitator shapes. The dynamics of the resulting linear models are compared to understand the affect of the cavitator shape on the non-planing vehicle.

All three cavitator shapes result in unstable non-planing trim points. The pole locations of the three models are plotted in Figure 4.4. The right half plane pole (RHP) of the disk cavitator vehicle is closest to the origin, followed by the 45^o cone vehicle

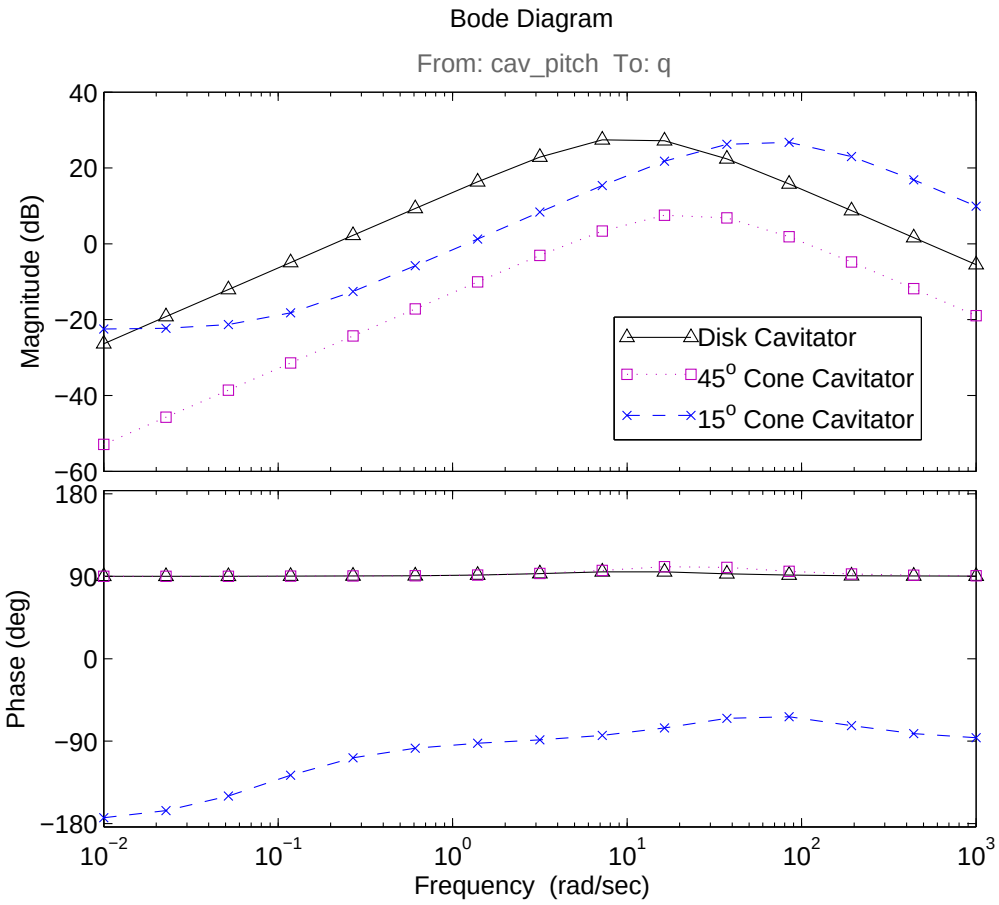

Figure 4.5: The cavitator to pitch rate Bode plot of the non-planing vehicle for different cavitator shapes

and finally the 15^o cone vehicle having the farthest RHP pole. This implies that faster actuators are required on the vehicle with the 15^o cone cavitator to overcome the vehicle's fast unstable dynamics. This matches the earlier qualitative analysis of the static stability of the three cavitator shapes.

Bode plots can be used to compare the control authority afforded by the three cavitator shapes. Figure 4.5 shows a Bode plot for the three cavitators' ability to affect the vehicle pitch rate. All three cavitators can be used to affect pitch rate at higher frequencies. The disk cavitator and the 15^o cone have relatively equal

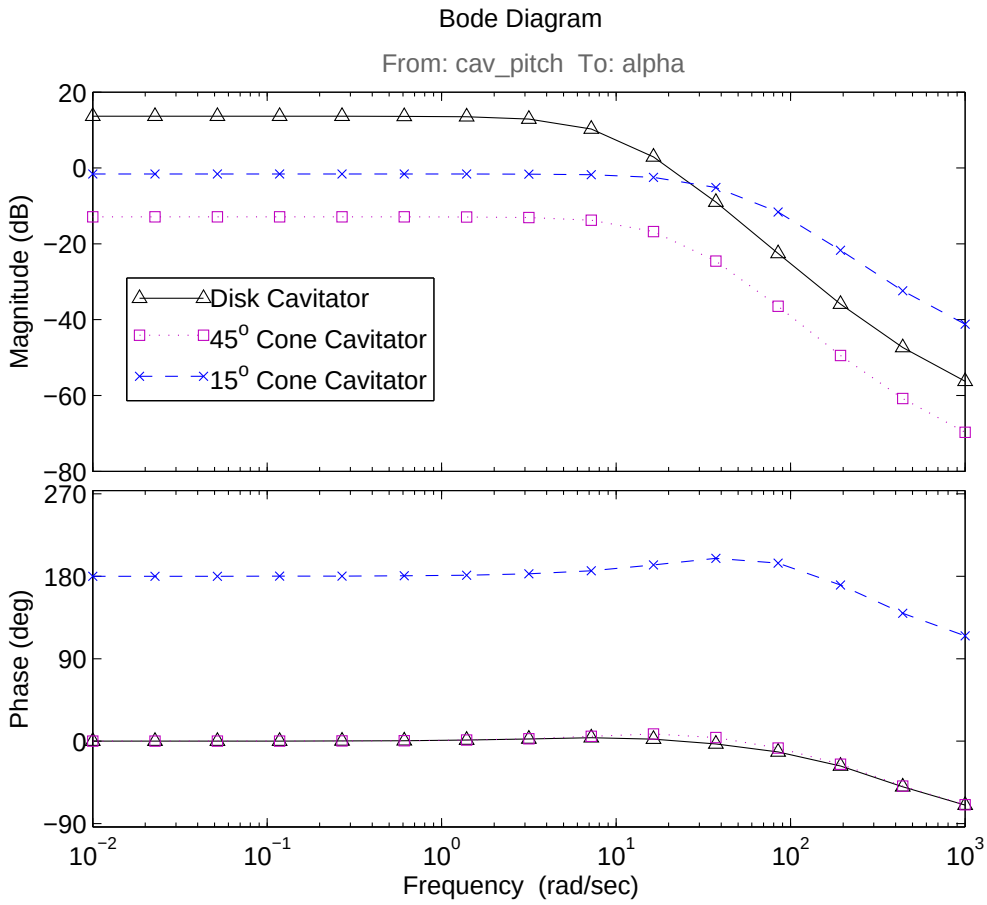

Figure 4.6: The cavitator to vehicle angle of attack Bode plot of the non-planing vehicle for different cavitator shapes

peaks in magnitude, which can be associated with their nearly equal lift curve slope magnitudes, but opposite signs which is visible from their associated phase. The 45^o cone has relatively poor control authority, and this confirms the very poor lift obtainable from the 45^o cone.

Similarly, Figure 4.6 shows the Bode plot for all three cavitators' ability to affect the vehicle angle of attack. Interestingly, the disk cavitator has by far the greatest control authority on affecting the vehicle angle of attack.

Disk Cavitator		45^o **Cone**		15^o **Cone**	
Name	Value	Name	Value	Name	Value
u	76.3 m/s	u	76.3 m/s	u	76.3 m/s
w	0.9396 m/s	w	0.9396 m/s	w	0.9404 m/s
q	0 rad	q	0 rad	q	0 rad
θ	0.05 rad	θ	0.05 rad	θ	0.05 rad
δ_c	-0.0358 rad	δ_c	-0.1390 rad	δ_c	$-.0083$ rad
T_x	2954.6 N	T_x	2900.7 N	T_x	2956.5 N
T_z	0 N	T_z	0 N	T_z	0 N
$\frac{h}{D_{body}}$	0.0113	$\frac{h}{D_{body}}$	0.0113	$\frac{h}{D_{body}}$	0.0115

Table 4.3: Trim conditions for planing non-linear 3 DOF equations for disk, 45^o, and 15^o cone cavitators. In all cases, $\sigma = 0.08$ and the polynomial approximations of the hydrodynamic coefficients are used

4.2.3 Planing

Using the previously calculated cavitator sizes, the same analysis is conducted in the planing case. Table 4.3 shows the planing vehicle trim conditions for each of the cavitator shapes.

Despite the 15^o cone having a positive lift curve slope, the trimmed 15^o cavitator deflection is a small negative value in this case. This is because the vehicle itself is trimmed at a positive angle of attack. The combination of the the positive vehicle angle of attack and the slight negative cavitator deflection results in the 15^o cavitator experiencing a local positive angle of attack.

The aft end of the planing vehicle is supported by planing and not thrust vectoring. The 15^o cone cavitator vehicle has a slightly larger planing immersion depth which can be explained by the same destabilizing moment coefficient that required additional thrust vectoring in the non-planing case.

Again the 3 DOF non-linear equations of motion are linearized at the three trim conditions,and the dynamics of the linear models are compared to understand the effect of the cavitator shape on the planing vehicle.

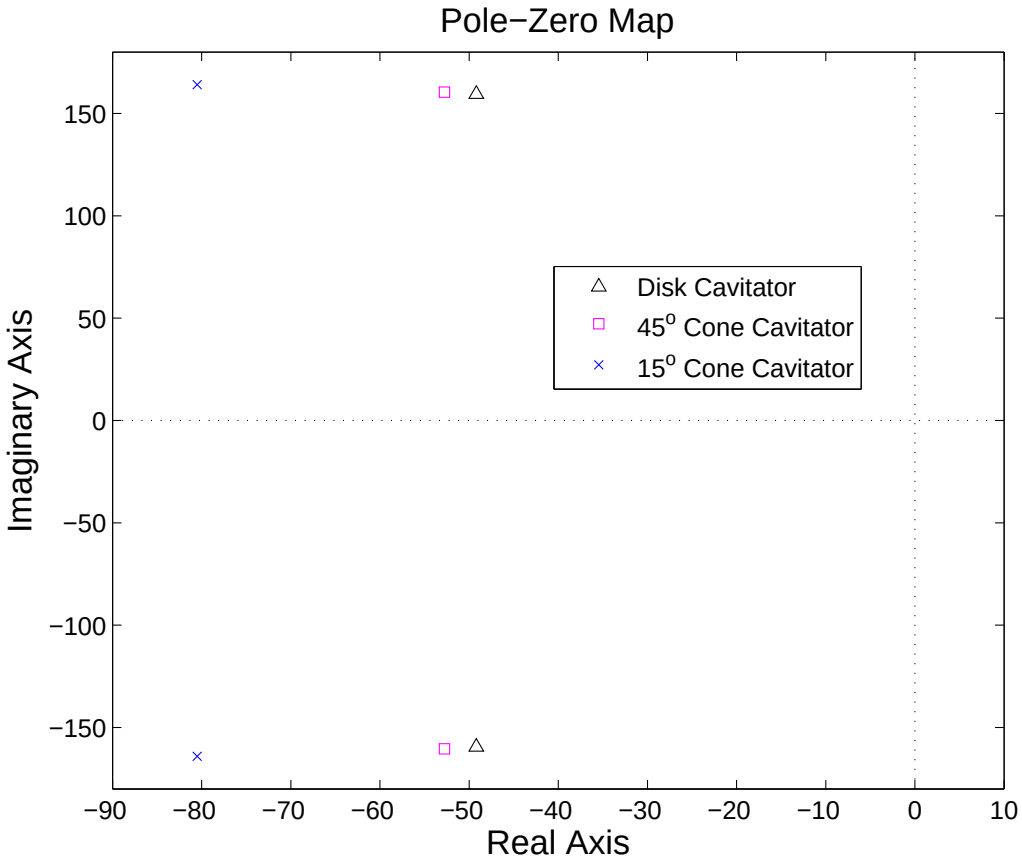

Figure 4.7: The location of the vehicle poles changes for different cavitator shapes on the planing vehicle

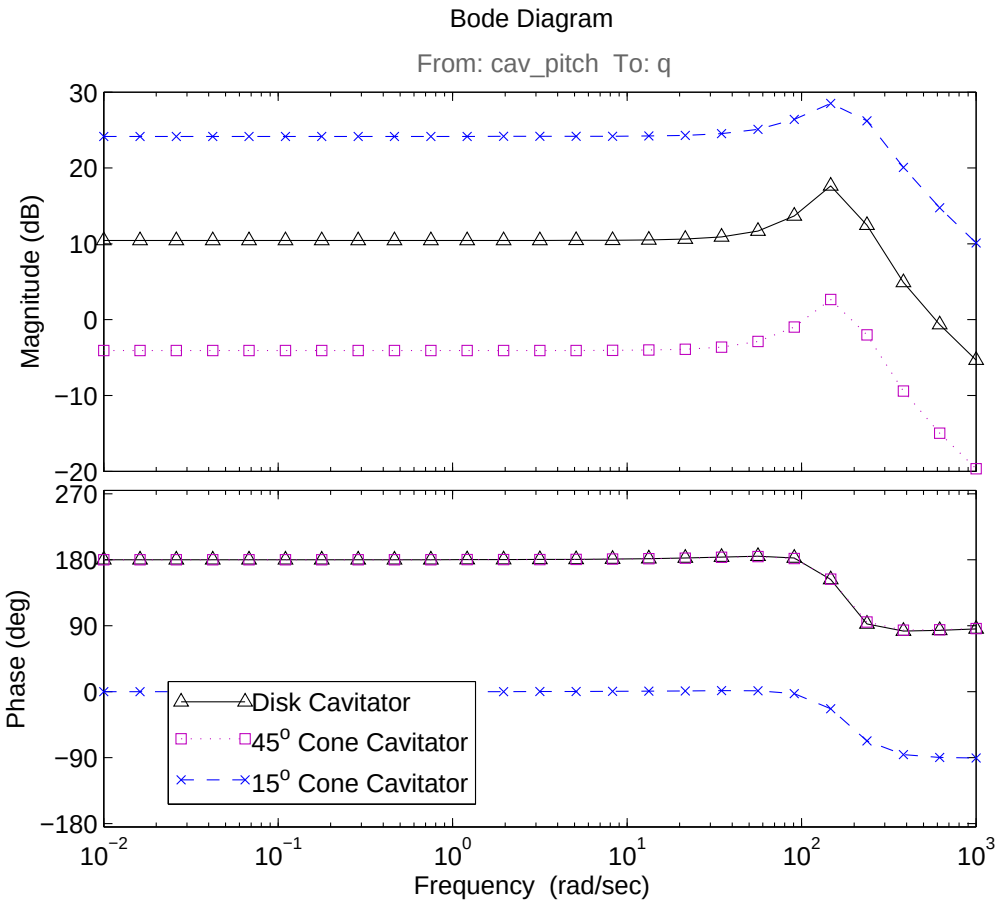

Figure 4.8: The cavitator to pitch rate Bode plot of the planing vehicle for different cavitator shapes

All three cavitator shapes result in stable planing trim points. The pole locations of the three models are plotted in Figure 4.7. The poles of the 15^o cone vehicle are the farthest from the origin giving the vehicle much faster dynamics. Although faster dynamics allow for very quick manoeuvres, there is greater complexity and demand for faster sensors and actuators. There also are structural implications when the vehicle has faster dynamics.

Bode plots for the ability of all three cavitators to affect the vehicle pitch rate are shown in Figure 4.8. The magnitude plots are very similar in shape but differ

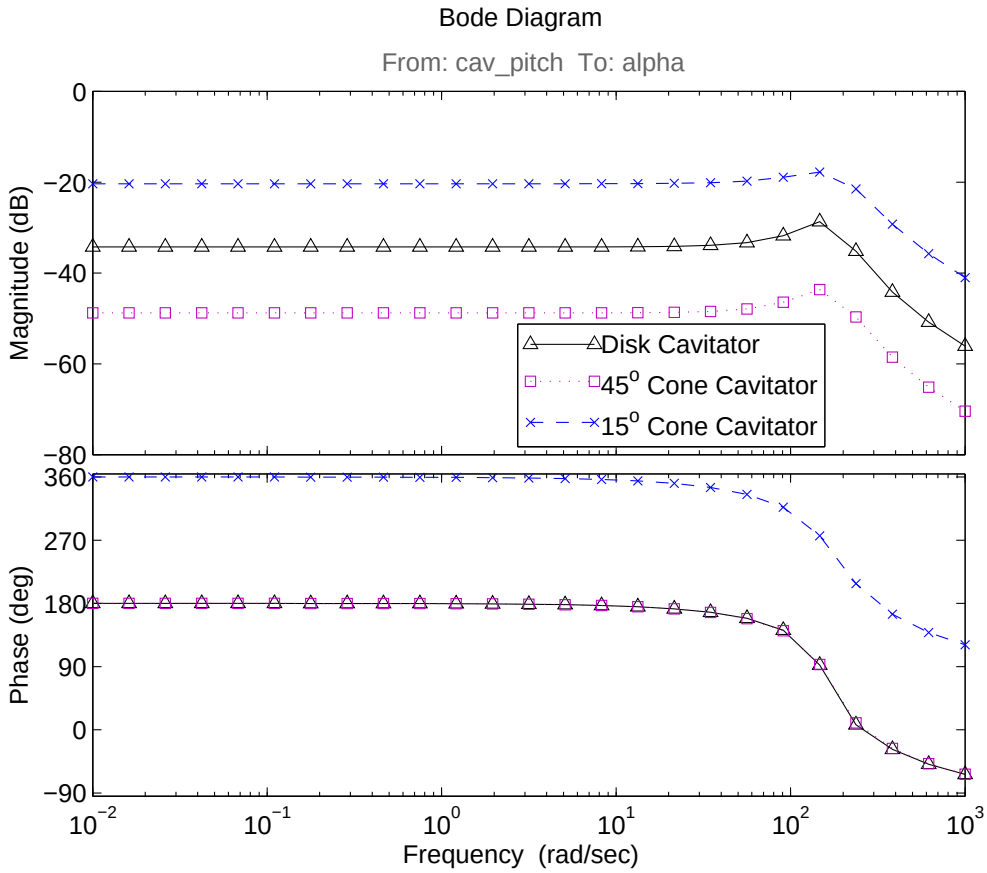

Figure 4.9: The cavitator to vehicle angle of attack Bode plot of the planing vehicle for different cavitator shapes

substantially in magnitude. The 15^o cone cavitator vehicle has by far the greatest control authority to affect the vehicle pitch rate. This differs when compared to the non-planing case where the disk cavitator vehicle had the greatest control authority.

Figure 4.9 shows the Bode plot for the ability of all three cavitators to affect the vehicle angle of attack. Although the same shape and control authority ordering as was seen in the cavitator to pitch rate is maintained, all three vehicles have very poor control authority in affecting the vehicle angle of attack when planing. This phenomenon was not seen in the non-planing vehicle, indicating that the stable dynamics of planing greatly overshadow the cavitator dynamics.

Chapter 5

Recommendations and Conclusion

The derived model used static experimental data to model the vehicle dynamics. Data on the dynamic effects on the various hydrodynamic components would greatly simplify, and improve the accuracy of the vehicle model. More specifically, understanding the dynamics of the forces and moments from the cavitator, planing, and fins. Planing is least understood, especially in regards to damping effects and how the forces and moments change depending on whether the vehicle is entering the water or pulling back into the cavity. Finally, much of the existing hydrodynamic data was collected over a large range of angles of attack. Throughout this work, it was determined that very small angles of attack and deflections would be necessary and thus more comprehensive experimental data at smaller angles of attack would provide a finer data set.

Several of the unique control challenges associated with supercavitating vehicles have been identified. The goal of this thesis was to provide a basic understanding of the physics of a supercavitating vehicle and linking the physics to the observed dynamics in simulation. Analyzing the non-planing linear dynamics, it was observed that the disk cavitator contributed damping to the vehicle but failed to provide static stability. Additionally, it was shown that a trade-off existed between static and dynamic stability as well as the implications on stabilizing using pitch rate feedback.

The effect of cavitator shape on the stability characteristics of the vehicle were studied. None of the three cavitator shapes achieved static stability, and in fact the disk cavitator was the least destabilizing in this regard. It was also shown that proportional pitch rate feedback was unable to stabilize the vehicle. This suggests that maintaining a non-planing operating condition is challenging to say the least and would be costly in terms of control authority. Maintaining a constant planing condition may be more desirable, although it requires a better understanding of the cavity dynamics.

Analyzing the planing vehicle's linear dynamics provided an understanding of planing's stabilizing features. This was done without consideration of the time delay and cavity pulsation affects which complicates planing. Comparisons between supporting the aft end of the vehicle with planing as opposed to using wedge shaped fins lead to general guidelines for sizing fins for the vehicle. Using smaller fins with larger angles of attack can greatly reduce the drag associated with the fins. Additionally, the effect of the fin aspect ratio on vehicle performance showed that higher aspect ratio fins both provide greater lift as well as robustness to cavity perturbations. Finally, a more detailed quantitative analysis of the cavitator shapes on the vehicle dynamics showed how there existed no benefits in terms of drag when comparing disk versus cone shaped cavitators. Additionally it was shown that 15^o cone shaped cavitator gave the vehicle faster dynamics which would required faster actuators as compared to the disk cavitator. The 45^o cone cavitator had very poor lift properties and no noticeable benefit on the vehicle dynamics.

Having a basic intuition for the vehicle dynamics can reduce time and effort during the actual control system design. It is hoped that this thesis shows the richness of understanding and insight that can be gained by taking a deep look at simplified vehicle models.

Appendix A

Nonlinear Simulation

The following is a brief documentation of the 6 degree of freedom nonlinear simulation of a supercavitating vehicle. The simulation is based on hydrodynamic coefficients and can be updated as new experimental data becomes available.

A.1 Nonlinear Model

Newton's method is used to derive the equations of motion for the vehicle. The base vehicle configuration has two primary sources of hydrodynamic forces and moments, namely:

1. Cavitator
2. Afterbody planing

The equations of motion for a general force and moment generating surface will be derived, and thereafter the general equations will be applied to the three hydrodynamic force and moment sources. This approach was chosen because the simulation is also implemented in this way. This allows for our simulation to be modular in nature and thus easy to update and modify.

A.1.1 Euler's Equations of Motion

The vehicle center of gravity is chosen as the origin for our body-fixed coordinate system (*b-frame*). Expressed in the *b-frame*, the translational equations of motion are given in Equation (2.3). Similarly, assuming the *b-frame* is selected as the principal axes, the rotational equations are given in Equation (2.2).

There are two ways to calculate the forces and moments for each hydrodynamic component. The first approach is to use an analytical formula and the second approach is using experimental data. Analytical expressions are important and provide a great deal of insight into each components behavior. These expressions are topics of research themselves, especially since the theory is complicated by the supercavitating conditions. The validity of these expressions are judged by experimental measurements. Experimental data will provide the forces and moments as a function of the conditions, like angle of attack and cavitation number. The two hydrodynamic components have been studied separately using experimental techniques and the results have been published [6] [10].

This simulation is based on non-dimensional force and moment coefficients. This allows a general framework to be implemented and furthermore available experimental results can be swapped into the simulation. Additionally the analytical force and moment expressions can be used to to generate non-dimensional coefficients allowing for comparison. Next the implementation of the Euler's Equations in Simulink is shown. Since this 6 degree of freedom model is implemented in Simulink, as the various equations are presented the relevant implementation in Simulink is also shown.

Simulink Implementation: Euler's Equations

Equations (2.1) and (2.2) were implemented into Simulink and saved as a library block named `SixDOF_block.mdl`, as shown in Figure A.4. The block named `6DoF (Euler Angles).mdl`

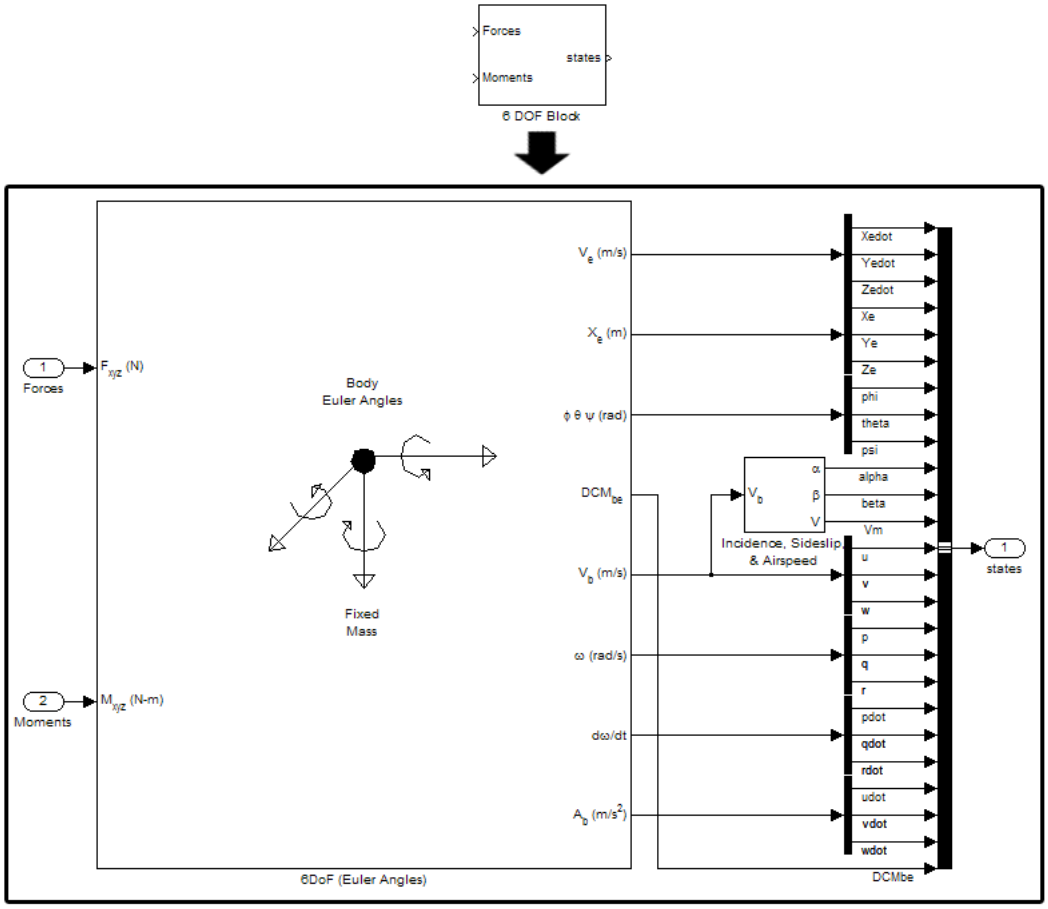

Figure A.1: Simulink implementation of Euler's Equation of motion

is taken from Simulink's Aerospace Blockset. Next is the analysis of a general force and moment component, starting with the coordinate frame.

A.2 Coordinate System

A diagram of the inertial and body-fixed coordinate systems (*b-frame*) are shown in Figure 2.1. Other coordinate systems will be defined later for simplifying the analysis of each general component, like the cavitator.

By a series of three rotations a vector expressed in the *b-frame* (x_b, y_b, z_b) can

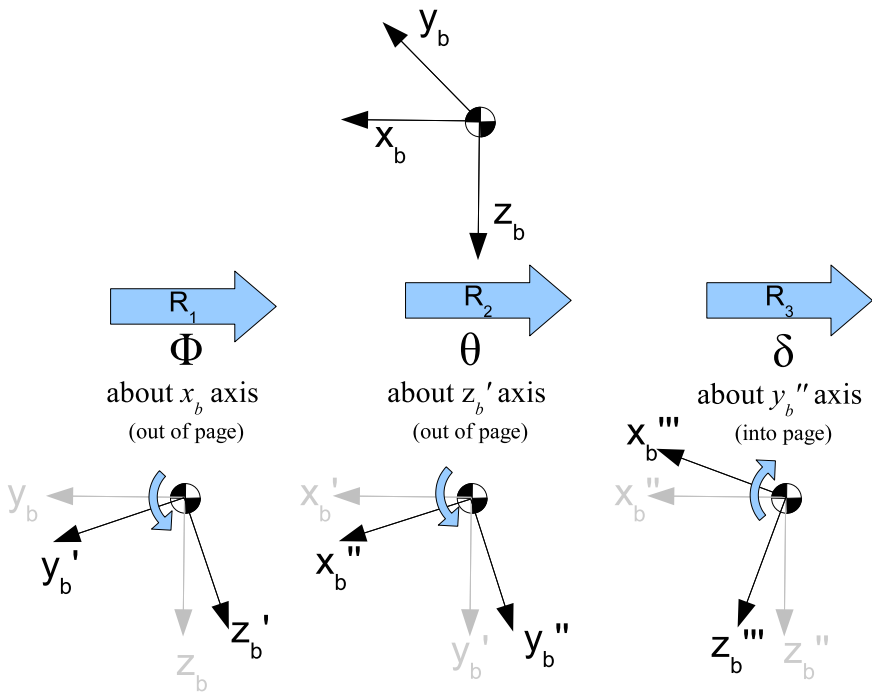

Figure A.2: Set of three rotations necessary to go from *b-frame* to any other general coordinate system. The rotation matrices (R_1, R_2, R_3) correspond to the three rotations (Φ, θ, δ) respectively.

be transformed to the other general frames. These three rotations are depicted in Figure A.2.

A.2.1 Rotation 1: Φ

The first rotation is about the x_b axis and is denoted by the angle $\Phi \in 0 : 2\pi$. The corresponding rotation matrix is given as Equation (A.1). As an example, in the case of four fins as the tail configuration of the vehicle, Φ would be 0, $\frac{\pi}{2}$, π, and $\frac{3\pi}{2}$ radians. If each fin has its own local coordinate system (x_f, y_f, z_f), in this way the y_{fi} axis is placed along the span of the *i'th* fin.

$$[R_1] = \begin{bmatrix} 1 & 0 & 0 \\ 0 & cos(\Phi) & sin(\Phi) \\ 0 & -sin(\Phi) & cos(\Phi) \end{bmatrix} \tag{A.1}$$

A.2.2 Rotation 2: θ

The second rotation is about the intermediate axis z_b' axis and is denoted by the angle $\theta \in 0 : 2\pi$. The corresponding rotation matrix is given as Equation (A.2). Continuing the fin example, the θ rotation corresponds to a sweepback of each fin.

$$[R_2] = \begin{bmatrix} cos(\theta) & sin(\theta) & 0 \\ -sin(\theta) & cos(\theta) & 0 \\ 0 & 0 & 1 \end{bmatrix} \tag{A.2}$$

A.2.3 Rotation 3: δ

The third and final rotation is about the intermediate axis y_b'' axis and is denoted by the angle $\delta \in -\pi : \pi$. The corresponding rotation matrix is given as Equation (A.3) and in the case of the fin, δ is the fin deflection.

$$[R_3] = \begin{bmatrix} cos(\delta) & 0 & -sin(\delta) \\ 0 & 1 & 0 \\ sin(\delta) & 0 & cos(\delta) \end{bmatrix} \tag{A.3}$$

A.2.4 Complete Rotation Matrix

The three rotation matrices $[R_1]$, $[R_2]$, and $[R_3]$ in the order presented can transform a vector from the *b-frame* (x_b, y_b, z_b) to any other general coordinate system (for example the fin or cavitator). This is shown in Equation (A.5) where v is any vector and the superscript denotes the coordinate system in which it is expressed. This transformation matrix is called the direction cosine matrix (DCM) and the two subsequent subscripts identify the direction of transformation. For example, DCM_{gb} would mean *direction cosine matrix transforming from body frame to general frame.* Since DCM is unitary ($DCM^{-1} \equiv DCM^T$), the opposite transformation is done using its transpose: DCM_{gb}^T transforms from general $\rightarrow$ body frame.

$$[DCM_{gb}] = [R_3][R_2][R_1] \tag{A.4}$$

$$\{v\}^{general} = [DCM_{gb}]\{v\}^{body} \tag{A.5}$$

A.3 General Component

For any general component, a series of properties must be known which will later be used to calculate the force and moment contribution. There are two categories of necessary information: vehicle specific properties and component specific properties. These are listed in Table A.1 and Table A.2 respectively.

A.3.1 Coordinate System

The first step is to define a coordinate system for the general component, which as previously mentioned places the y-axis along the span of the component (if applicable, like fins). The location of this coordinate system must be specified as well as its

Vehicle Specific Properties

Name	Description	Units
σ	cavitation number	-
ρ	water density	$\frac{kg}{m^3}$
$\bar{r}_{b\to cg}$	position vector from origin of *b-frame* to *cg*, expressed in *b-frame*	m
$\bar{v}_{cg}$	velocity of cg expressed in *b-frame*	$\frac{m}{s}$
ω	angular velocity expressed in *b-frame*	$\frac{rad}{s}$
$C_L,\ C_D,\ etc...$	hydrodynamic coefficients	-

Table A.1: List of vehicle specific properties used to calculate each general component's force and moment contribution

Component Specific Properties

Name	Description	Units
$\bar{r}_{b\to g}$	position vector from origin of *b-frame* to origin of *general frame*, expressed in *b-frame*	m
$\bar{r}_{g\to cp}$	position vector from origin of *general frame* to center of pressure (*cp*) of the component, expressed in *general frame*	m
DCM_{gb}	direction cosine matrix which transforms from *b-frame* $\to$ *general frame*	-
S	reference area	m
l_{ref}	reference length	m
b	reference span	m

Table A.2: List of component specific properties used to calculate each general component's force and moment contribution

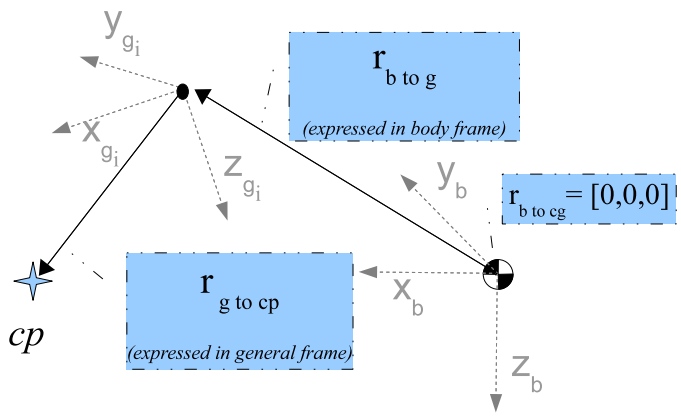

Figure A.3: Defining the relation between the vehicle cg, the *b-frame*, the component's *general frame*, and the general component's *cp*.

orientation with respect to the vehicle body frame. Figure A.3 shows a general case with all three important position vectors defining the relationships between the vehicle *cg*, component *cp*, the *general frame* and the *b-frame*. By defining our specific *general frame*, we are specifying $\bar{r}_{b\to g}$ and DCM_{gb}. The transformation matrix DCM_{gb} is obtained by Equation (A.4). This means any component deflection is accounted for in this manner and the general frame both is fixed to and rotates with the general component.

A.3.2 Local Conditions

Next the velocity at the *cp* of the component is determined. To obtain this, we need the position vector between the vehicle cg and the cp of the component:

$$\bar{r}_{cg\to cp} = -\bar{r}_{b\to cg} + \bar{r}_{b\to g} + [DCM_{gb}]^T \bar{r}_{g\to cp} \tag{A.6}$$

Where the $[DCM_{gb}]^T$ is necessary to keep all of Equation (A.6) expressed in the *b-frame*. Note that so long as the origin of the *b-frame* is chosen as the *cg*, $\bar{r}_{b\to cg} = [0,0,0]^T$. Using $\bar{r}_{cg\to cp}$, the vehicle velocity $\bar{V}_{cg} = [u,v,w]^T$, and the angular rates $\omega = [p,q,r]^T$ we can apply the transport theorem and find the local velocity at *cp* and express it in the *general frame*:

$$\bar{v}_{cp} = DCM_{gb}[\bar{v}_{cg} + \omega \times \bar{r}_{cg\to cp}] \tag{A.7}$$

Note the DCM_{gb} in Equation (A.7) expresses the $\bar{v}_{cp}$ vector in the respective general frame (x_g, y_g, z_g) of the component. *We will continue to work in the general frame for the next steps.* Using the components of the local velocity vector $\bar{v}_{cp} = [u_g, v_g, w_g]^T$ we can find the local angle of attack (α_g), sideslip angle (β_g), and velocity magnitude (V_g).

$$\alpha_g = tan^{-1}\left(\frac{w_g}{u_g}\right) \tag{A.8}$$

$$V_g = \sqrt{u_g^2 + v_g^2 + w_g^2} \tag{A.9}$$

$$\beta_g = tan^{-1}\left(\frac{v_g}{V_g}\right) \tag{A.10}$$

Equations (A.8), (A.9), and (A.10) give the local conditions at a generalized component, expressed in the *general frame*. Next the components hydrodynamic coefficients are determined for the calculated flow conditions.

Simulink Implementation: Local Conditions

Equations (A.7), (A.8), (A.9), and (A.10) were implemented into Simulink and saved as a library block named `Local_conditions.mdl`, as shown in Figure A.4.

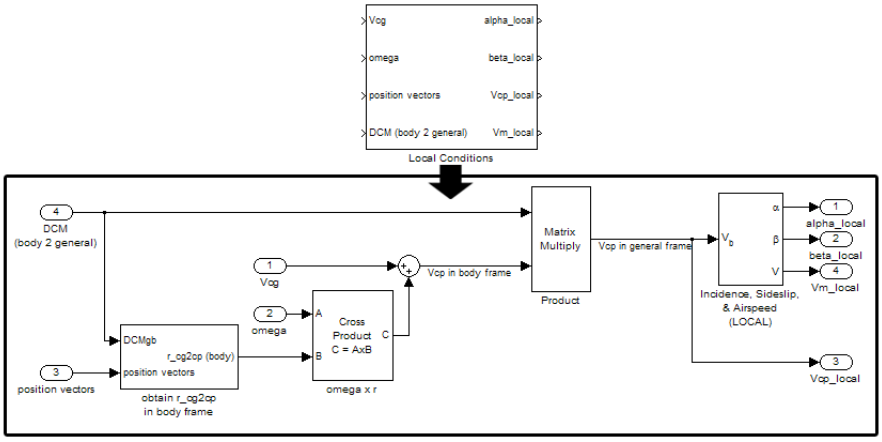

Figure A.4: Simulink implementation of local conditions calculations.

Coefficients for Varying Axes

Body	Stability	Wind
C_x axial force	$C_{D(\beta=0)}$ drag force	C_D drag force
C_y side force	C_y side force	C_c cross-wind force
C_z normal force	C_L lift force	C_L lift force
C_l rolling moment	C_l rolling moment	C_l rolling moment
C_m pitching moment	C_m pitching moment	C_m pitching moment
C_n yawing moment	C_n yawing moment	C_n yawing moment

Table A.3: List coefficients used for body, stability, and wind axes. This derivation used the wind axis set of coefficients.

A.3.3 Hydrodynamic Coefficients

Using the obtained local flow conditions at the component of interest, the corresponding hydrodynamic coefficients will be determined. Lookup tables will be used for this purpose. These coefficients are commonly presented in three axes: body, stability, or the wind axes, as listed in Table A.3.

At this point we have data on C_D, C_L, and C_m for the main components and will be using the wind axis convention. This information is given as a function of angle of attack (α), cavitation number (σ), and submergence ratio in the case of planing. Experimental data on the dependence of these coefficients on sideslip angle (β) was

not available. The unknown contributions to the coefficients were neglected but may be added later when data becomes available. During control design one may study the effect of these coefficients on the controller performance by including uncertainty in their values.

A linear interpolation of the lookup table values was used to obtain the necessary coefficients for the given set of conditions. The local dynamic pressure ($\bar{q}_g$) for the component can be calculated as shown in Equation (A.11).

$$\bar{q}_g = \frac{1}{2}\rho V m_g^2 \tag{A.11}$$

Simulink Implementation: Hydrodynamic Coefficients

The lookup tables described as well as Equation (A.11) were implemented in Simulink and saved as a library block named `Aero_Coeff.mdl`, as shown in Figure A.5. Note the unknown coefficients are currently set to zero.The dependence on sideslip (β) is also unknown as previously mentioned, and thus currently not used.

A.3.4 Hydrodynamic Forces and Moments

Thus far a 6×1 vector of hydrodynamic coefficients expressed in the local wind axis for a general component as well as the local dynamic pressure is obtained. The following parameters are defined next and later used for completing the general force and moment derivation. These parameters come either directly or indirectly from the component specific properties in Table A.2. First the position vector between the general component and the vehicle cg is required:

$$\bar{r}_{g\to cg} = [DCM_{gb}](\bar{r}_{b\to cg} - \bar{r}_{b\to g}) \tag{A.12}$$

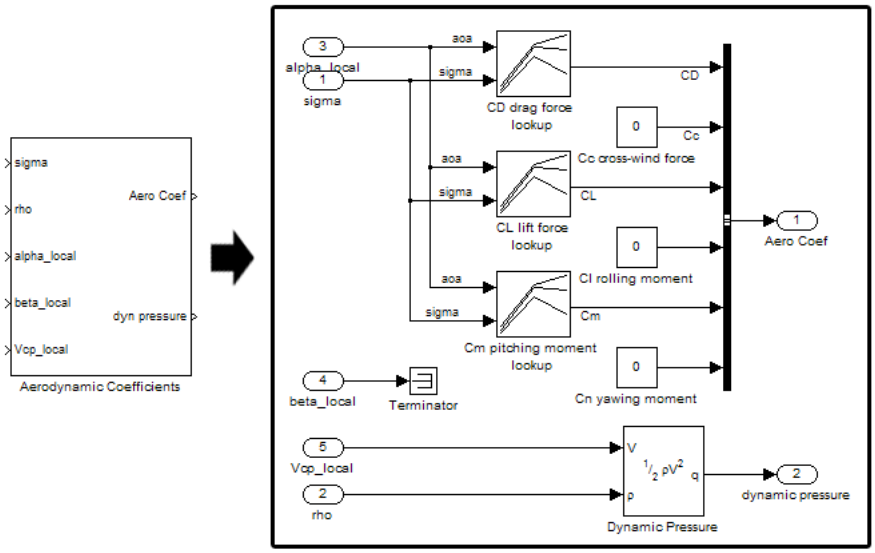

Figure A.5: Simulink implementation of hydrodynamic coefficient lookup tables and local dynamic pressure calculation.

Where the $[DCM_{gb}]$ is necessary to keep all of Equation (A.12) expressed in the *general frame*. It is also necessary to define the position vector between the origin of the general component frame and the *cp* of the component. This vector ($\bar{r}_{g\to cp}$) is directly taken from Table A.2 and is already expressed in the *general frame*. The local velocity vector ($\bar{v}_{cp}$) is defined in Equation (A.7). Finally, it is necessary to define the reference geometries S, l_{ref}, and b which are used to non-dimensionalize the hydrodynamic coefficients of the general component.

The force coefficients and the moment coefficients are separated into two 3×1 vectors, as shown in Equations (A.13) and (A.14).

$$C_{forces} = \begin{bmatrix} C_D \\ C_c \\ C_L \end{bmatrix} \tag{A.13}$$

$$C_{moments} = \begin{bmatrix} C_l \\ C_m \\ C_n \end{bmatrix} \tag{A.14}$$

The forces are discussed first and thereafter the moments, but before hand a new transformation matrix necessary to convert between the local wind axis and the *general frame* of the component is defined.

Local Wind to General Frame Transformation

Earlier α_g and β_g were obtained using Equations (A.8) and (A.10). The transformation begins in the *general frame* with a rotation of $-\alpha_g$ about the y_g axis and thereafter a rotation of β_g about the transformed z_g axis. Thus using the previously defined rotation matrix convention, $\delta = -\alpha_g$ and $\theta = \beta_g$ and obtain $[R_3]$ and $[R_2]$ as defined in Equations (A.3) and (A.2) respectively.

$$[DCM_{wg}] = [R_2][R_3] \tag{A.15}$$

$$\{v\}^{wind} = [DCM_{wg}]\,\{v\}^{general} \tag{A.16}$$

The transformation matrix from *general frame* to the local wind axis of the general component is given by Equation (A.15). An example of such a transformation is shown in Equation (A.16) where v is any vector and the superscript denotes the coordinate system in which it is expressed.

Forces

The necessary parameters are now defined for calculating the forces from the general component acting on the vehicle. Equation (A.17) shows the forces expressed in the wind axis. The negative of the force coefficients is necessary to match them with the vehicle wind axis. Thereafter, since the hydrodynamic coefficients are given in the wind axis, two pre-multiplying transformation matrices convert from the local wind axis to the *general frame* of the component and finally to the *b-frame* of the vehicle as shown in Equation (A.18).

$$\bar{F}_g^{wind} = \begin{bmatrix} -C_D \bar{q}_g S \\ -C_c \bar{q}_g S \\ -C_L \bar{q}_g S \end{bmatrix} \tag{A.17}$$

$$\bar{F}_g = [DCM_{gb}]^T [DCM_{wg}]^T \bar{F}_g^{wind} \tag{A.18}$$

Moments

The general component moments can be divided into two parts. The first due to the forces acting at a location other than the vehicle *cg*. The second due to hydrodynamic moment coefficients. Equation (A.19) defines the moment arm between the component's *cp* and the vehicle *cg*, expressed in the wind frame. Equation (A.20) takes the cross product between the component's force vector and the moment arm, all expressed in the wind frame. The sum of the force induced moments and the moment contributions of moment coefficients are also expressed in the wind frame. Finally in Equation (A.21) two transformation matrices are used to express the total moment from the general component in the *b-frame*.

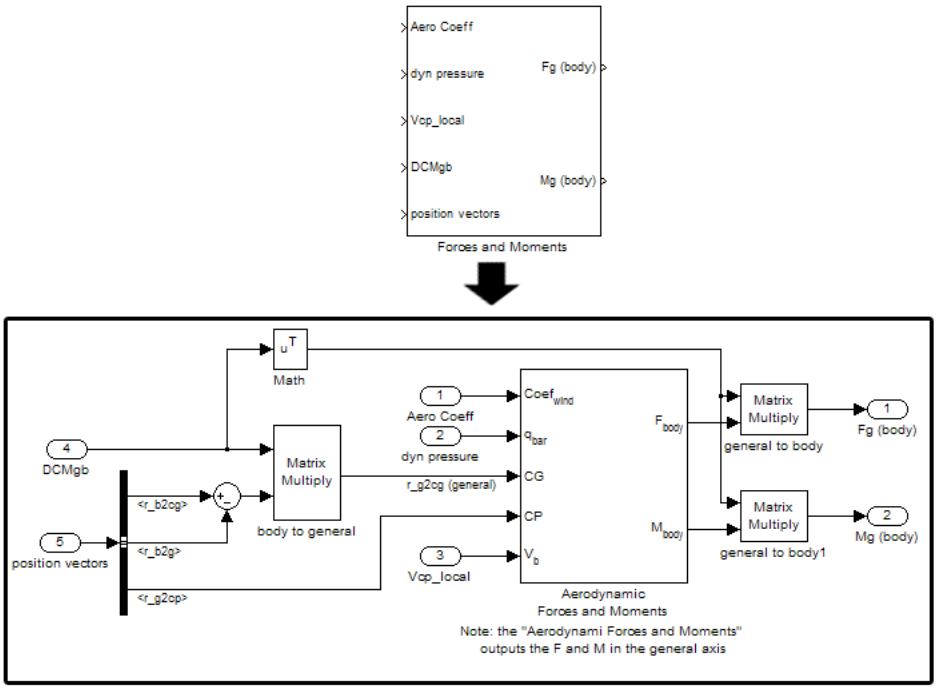

Figure A.6: Simulink implementation of general component forces and moment calculation.

$$\bar{r}_{cp\to cg}^{wind} = [DCM_{wg}](\bar{r}_{g\to cg} - \bar{r}_{g\to cp}) \tag{A.19}$$

$$M_g^{wind} = F_g^{wind} \times \bar{r}_{cp\to cg}^{wind} + \begin{bmatrix} C_l \bar{q}_g Sb \\ C_m \bar{q}_g Sl_{ref} \\ C_n \bar{q}_g Sb \end{bmatrix} \tag{A.20}$$

$$M_g = [DCM_{gb}]^T [DCM_{wg}]^T M_g^{wind} \tag{A.21}$$

Simulink Implementation: Aerodynamic Forces and Moments

The forces and moment equations are implemented into Simulink and saved as a library block named `Force_Moment.mdl`, as shown in Figure A.6. Note the block named `Aerodynamic Forces and Moments.mdl` is from Simulink's Aerospace Blockset.

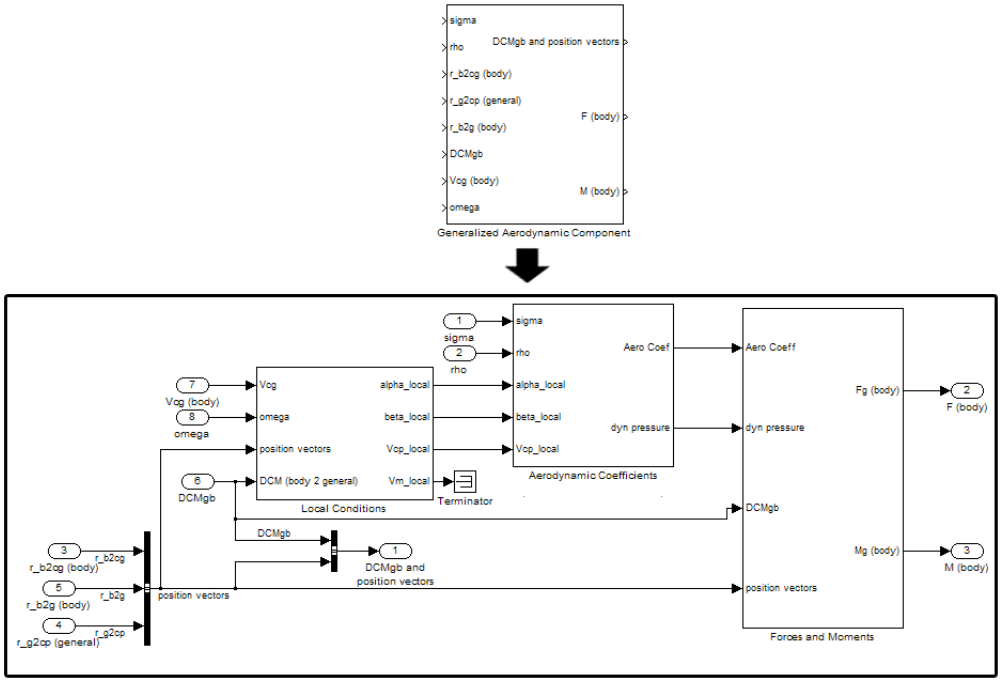

Figure A.7: Simulink implementation of general component block.

A.3.5 Simulink Implementation: General Component

The above derivations allow for adding a force and moment generating surface to the vehicle in a modular fashion. All three blocks: Local Conditions, Hydrodynamic Coefficients, and Forces and Moment block together are combined into a single Generalized Hydrodynamic Component block. The data flow in this block is shown in Figure A.7. The forces and moments from the general components are summed and passed to the `SixDOF_block.mdl` shown in Figure Figure A.4.

A.4 Cavitator Component

The implementation of the cavitator is simplified greatly using the above general component derivation. Using the vehicle and component specific properties listed in Table A.1 and Table A.2 respectively, the cavitator force and moment contributions

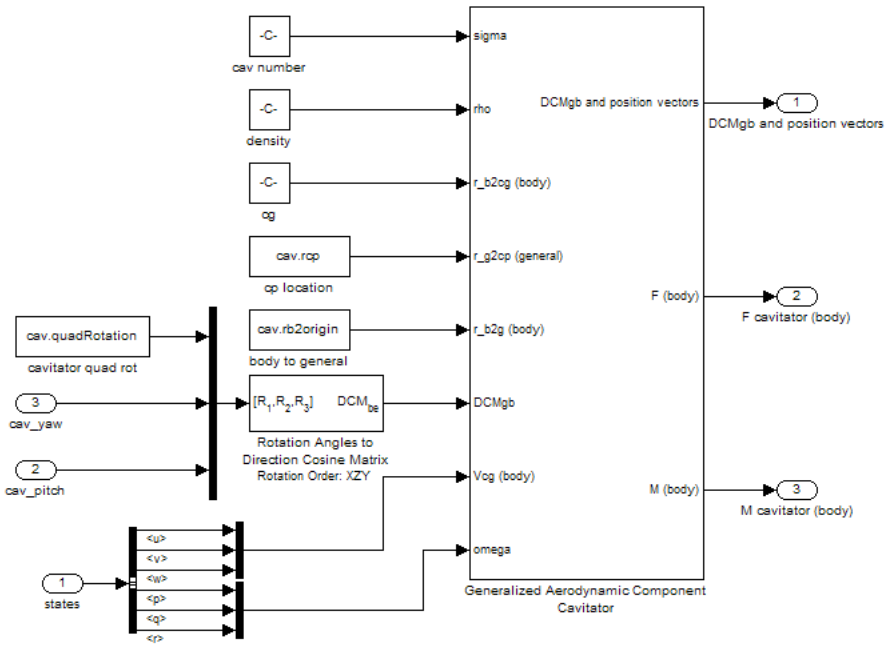

Figure A.8: Simulink implementation of cavitator component block.

is obtained without any additional derivation.

A.4.1 Simulink Implementation: Cavitator Component

The cavitator implementation of the general component is shown in Figure A.8. As visible from the figure, the three rotation angles (Φ, θ, δ) used to define the direction cosine matrix are $(0, \textit{cavitator yaw}, \textit{cavitator pitch})$ respectively.

A.5 Planing

Planing occurs when the vehicle afterbody slaps against the cavity wall. The vehicle-cavity interaction is among the major challenges associated with supercavitating vehicles. From a simulation standpoint, the cavity must be modeled such that such that planing can be detected and the planing forces and moments applied to the vehicle

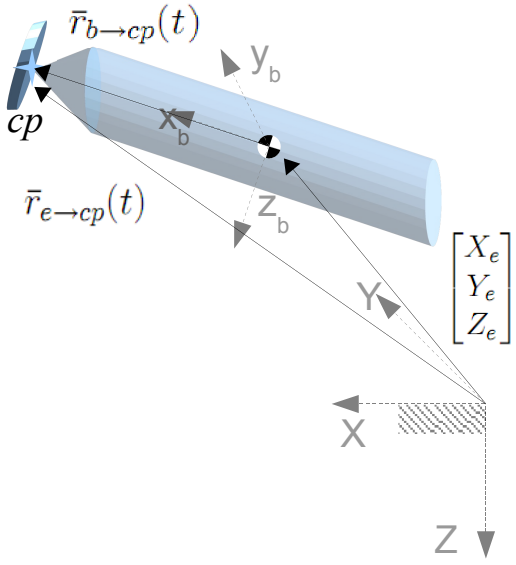

Figure A.9: Illustration of Equation (A.23), which will help determine the time history of the cavitator position.

when necessary.

Continuing with the intent to create a modular simulation, the varying components necessary to detect and account for planing are discussed next. The Logvinovich cavity model will be used in this simulation and the planing forces and moments will be implemented using the previously derived general component approach.

A.5.1 Cavity Memory Effects

The time history of the cavitator centerline is the line around which the cavity grows and collapses. Thus the cavity shape near the aft end of the vehicle, where planing is of interest, depends on the past location of the cavitator .

The position vector from the origin of the inertial frame (X, Y, Z) to the cavitator *cp* is defined in Equation (A.23) and illustrated in Figure A.9. Note the position vector $\bar{r}_{e\to cp}(t)$ is expressed in the earth frame as a function of time.

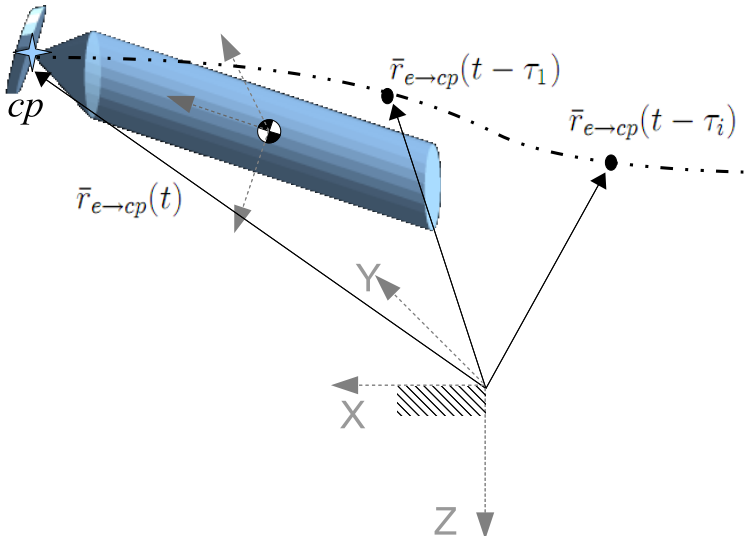

Figure A.10: Showing the delayed $\bar{r}_{e\to cp}$ vector.

$$\bar{r}_{b\to cp} = \bar{r}_{b\to g} + [DCM_{gb}]^T \bar{r}_{g\to cp} \tag{A.22}$$

$$\bar{r}_{e\to cp}(t) = DCM_{be}^T \bar{r}_{b\to cp} + [X_e, Y_e, Z_e]^T \tag{A.23}$$

Next $\bar{r}_{e\to cp}(t)$ is delayed to keep track of the delayed position vectors. This is illustrated in Figure A.10.

Thereafter the *current* vehicle position $[X_e, Y_e, Z_e]^T$ is subtracted from each of the delayed position vectors, $\bar{r}_{e\to cp}(t-\tau_i)$ and transformed back to the *b-frame*, as done in Equation (A.24). This gives a time history of the cavitator position expressed in the *b-frame*, as illustrated in Figure A.11.

$$\bar{r}_{b\to cp}(t-\tau_i) = DCM_{be}(\bar{r}_{e\to cp} - [X_e, Y_e, Z_e]^T) \tag{A.24}$$

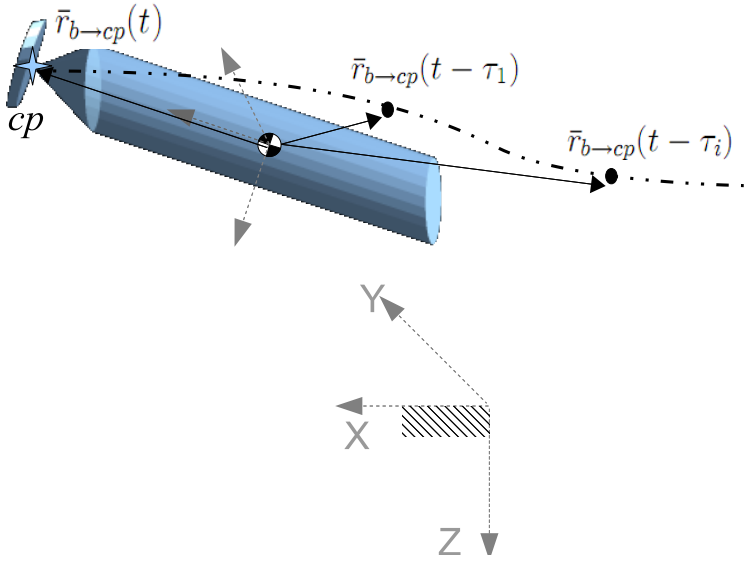

Figure A.11: Illustration of position vector between *b-frame* and past positions of the cavitator *cp*.

Thus the position vector of the cavitator *cp* for past and present times steps is obtained, all expressed in the *b-frame*. The vehicle geometry can be used to define the location of the vehicle tail. Using these two pieces of information along with the cavity radius as a function of the time that has passed since its inception, it can be determined if the vehicle tail has made contact with the cavity wall.

Simulink Implementation: Cavity Memory Effects

The forces and moment equations were implemented into Simulink and saved as a library block named `Delay_Position.mdl`, as shown in Figure A.12. Note the number of delayed position output vectors can be increased or decreased as necessary.

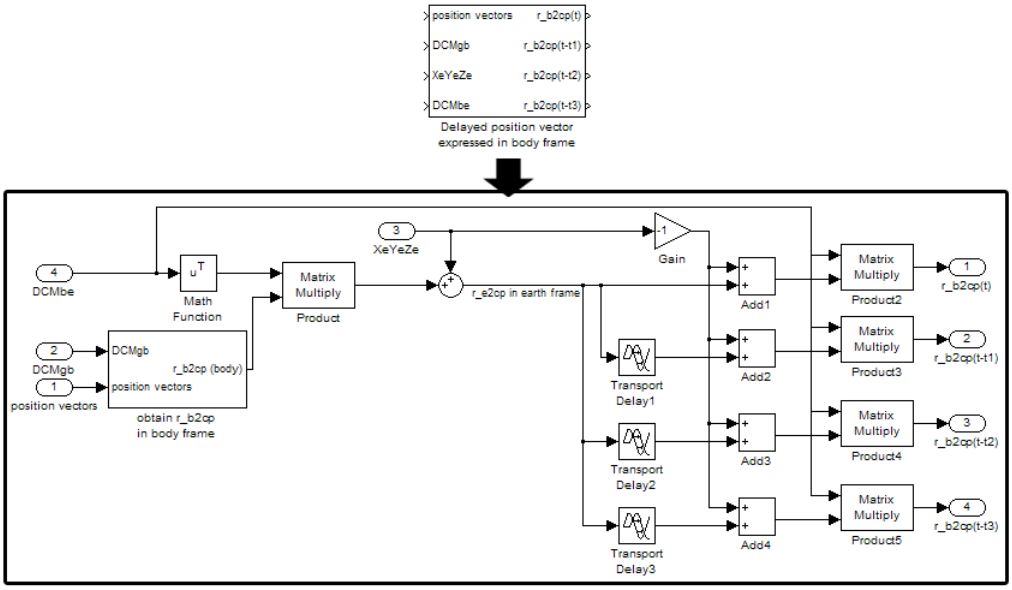

Figure A.12: Simulink implementation giving the time history of cavitator centerline.

A.5.2 Logvinovich Cavity Model

A model which adequately captures the cavity dynamics and lends itself well to numerical implementation was used. The initial model of choice is by Logvinovich which provides the radius of the cavity as a function of time since making contact with the cavitator. Logvinovich's model and the relevant equations are shown in Equation (2.38).

Simulink Implementation: Logvinovich Cavity Model

The cavity model presented by Logvinovich, namely Equation (2.38) was implemented into Simulink and saved as a library block named `Cavity_Radius.mdl`, as shown in Figure A.13.

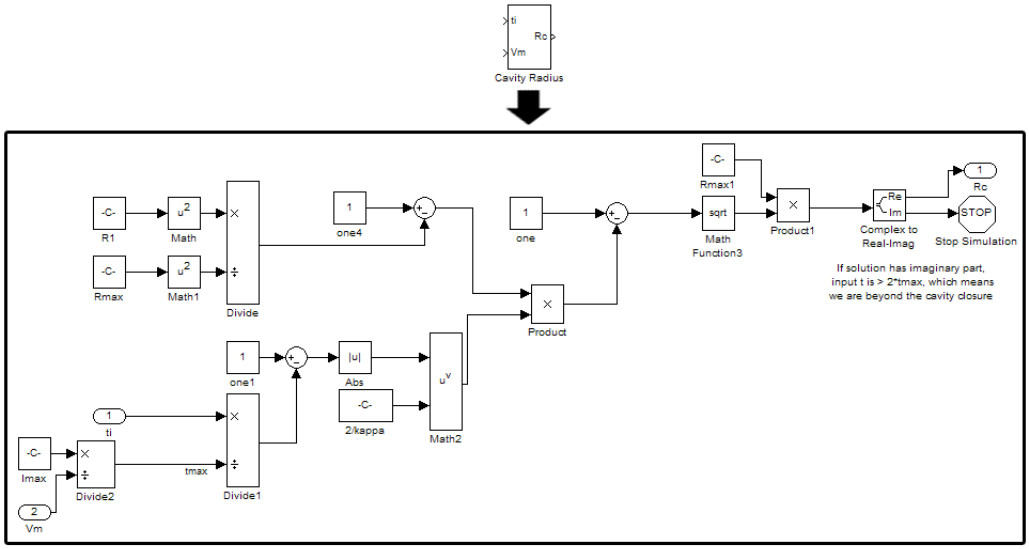

Figure A.13: Simulink implementation giving cavity radius as function of time since inception

A.5.3 Projected Cavity Radius

The goal in modeling the cavity is to detect planing. Once the radius of cavity has been determined as a function of time since making contact with the cavitator, the direction of the cavity radius vector must be determined. This is accomplished by always defining each radius vector perpendicular to the velocity vector of the cavitator at the instant of inception. This means the direction of the radius vector τ_i seconds after cavity inception is determined by the cavitator velocity vector at time $\bar{V}_{cav}(t - \tau_i)$. This is shown graphically in Figure A.14; note how each planar section is perpendicular to the cavitator velocity vector of interest. This is accomplished mathematically using the cross product operation as shown in Equation (A.25).

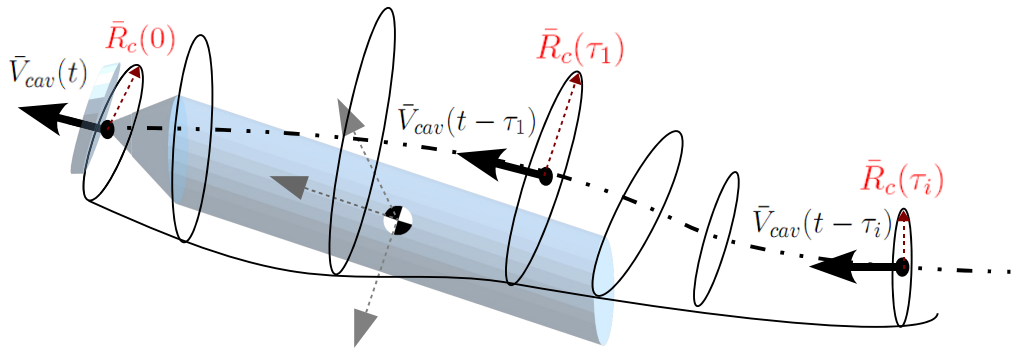

Figure A.14: Cavity planar section at each instant is perpendicular to the cavitator velocity vector that initiated that section.

$$\bar{V}_{\perp}(t-\tau_i) = \bar{V}_{cav}(t-\tau_i) \times [1\ 1\ 1]^T \tag{A.25}$$
$$\hat{V}_{\perp}(t-\tau_i) = \frac{\bar{V}_{\perp}(t-\tau_i)}{\left|\bar{V}_{\perp}(t-\tau_i)\right|}$$
$$\bar{R}_c(\tau_i) = R_c(\tau_i)\hat{V}_{\perp}(t-\tau_i)$$

The cross product between the delayed velocity vector and a non-coinciding arbitrary vector results in a third vector ($\bar{V}_{\perp}$) in the plane perpendicular to the original two. Next the obtained vector is normalized as a unit vector and thereafter multiplied by the cavity radius magnitude at that instant ($R(\tau_i)$). This results in a vector representation of the radius of the cavity in the planar section of interest.

The vector representation of the cavity radius is next projected into the body $y_b - z_b$ plane and the magnitude of the cavity radius in the body frame, $R_{proj}(\tau_i)$, is determined as shown in Equation (A.26).

$$\bar{R}_{proj}(\tau_i) = \begin{bmatrix} 0 \\ \bar{R}_c(\tau_i) \cdot [0\ 1\ 0]^T \\ \bar{R}_c(\tau_i) \cdot [0\ 0\ 1]^T \end{bmatrix} \tag{A.26}$$

$$R_{proj}(\tau_i) = \sqrt{\bar{R}_{proj}(\tau_i) \cdot \bar{R}_{proj}(\tau_i)} \tag{A.27}$$

The final necessary detail is where to check for planing - at which τ_i does planing occur? One may decide to use a range of discrete τ values and check for planing at each point. In the interest of computational ease and to minimize complexity, it was decided to check for planing at a single τ value near the end of the vehicle. This τ value is approximated from the level flight case where the time that passes to propagate from the nose to the tail of the vehicle is a function of the vehicle length and speed. This is shown in Equation (A.28) where τ_p denotes the time at which to check for planing, L_{body} the vehicle length, and V is the vehicle speed.

$$\tau_p = \frac{L_{body}}{V} \tag{A.28}$$

From the information derived, the angle between the cavity boundary and the vehicle wall, denoted α_{cb} must also be obtained. Using the definition of dot product, this is accomplished in Equation (A.29) where the angle between the radius vector ($\bar{R}_c(\tau_i)$) and the projected radius ($R_{proj}(\tau_i)$) is obtained.

$$\alpha_{cb} = cos^{-}1 \left(\frac{\bar{R}_c(\tau_i) \cdot R_{proj}(\tau_i)}{|\bar{R}_c(\tau_i)||R_{proj}(\tau_i)|} \right) \tag{A.29}$$

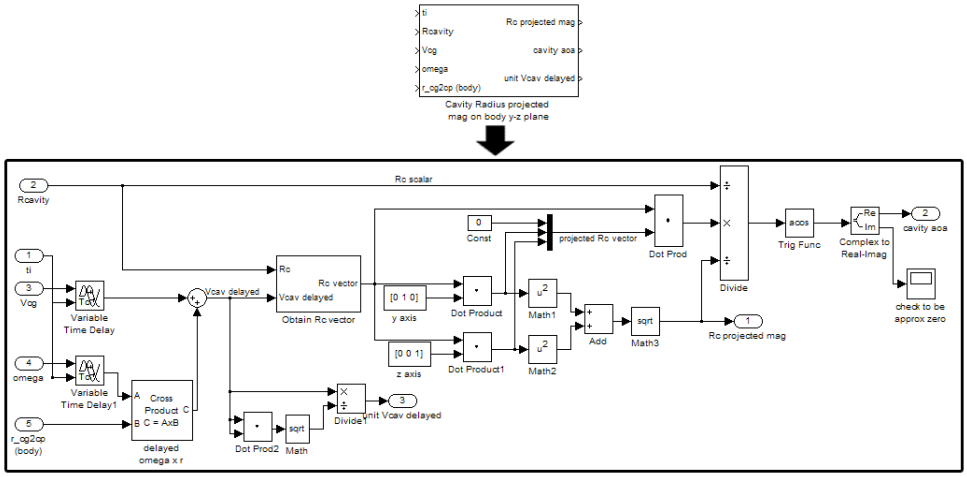

Figure A.15: Simulink implementation projecting the cavity radius into the body $y_b - z_b$ plane and determining its magnitude

This angle is used in the lookup tables for the planing hydrodynamic coefficients.

Simulink Implementation: Project Cavity Radius

The equations that project the cavity radius onto body frame were implemented into Simulink and saved as a library block named `Projected_Radius.mdl`, as shown in Figure A.15.

At this point the information necessary to check for planing in the vehicle $y_b - z_b$ plane is available:

- The vehicle tail position center position, $[0\ 0]^T$
- The vehicle radius, R_{body}
- The cavity centerline position, y and z coordinate of $\bar{r}_{b\to cp}(t - \tau_p)$
- The cavity radius projected magnitude, $R_{proj}(\tau_p)$

This information is displayed in Figure A.16.

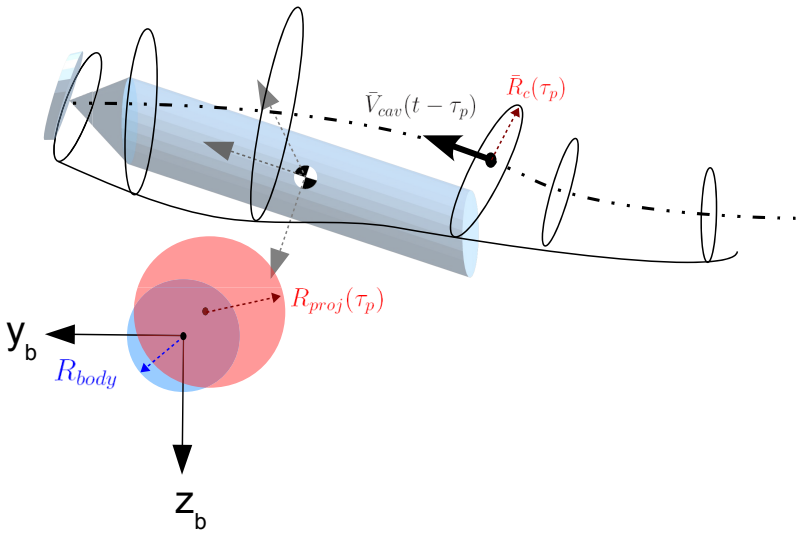

Figure A.16: Depicting the information obtained to check for planing on the vehicle.

A.5.4 Detecting Planing

The depth to which the vehicle body is submerged into the cavity wall is defined as the immersion depth, h. The planing detection is conducted in the $y_b - z_b$ plane. The immersion depth can be calculated as in Equation (A.30) and is shown graphically in Figure A.17.

$$h = \begin{cases} 0 & \text{if } d_c + R_{body} - R_{proj}(\tau_p) \leq 0 \\ d_c + R_{body} - R_{proj}(\tau_p) & otherwise \end{cases} \tag{A.30}$$

Here d_c is the distance between the vehicle center point and the cavity center point and should not be confused in the diameter of the cavitator. At this point the direction in which the planing force acts is determined.

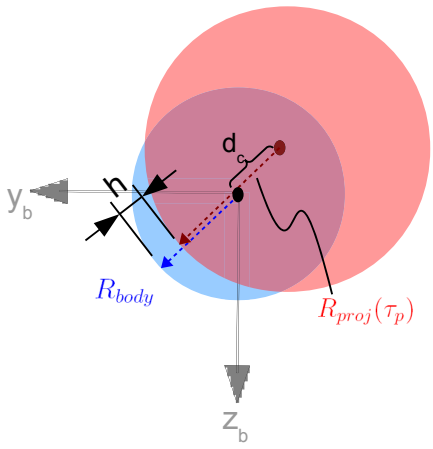

Figure A.17: The immersion depth (h) is the depth of the vehicle submerged into the cavity wall and is used to determine the planing force on the vehicle.

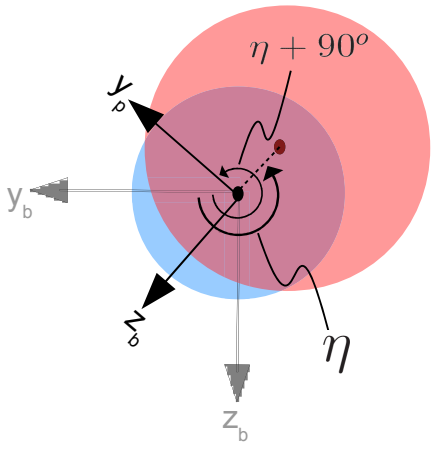

Figure A.18: The rotation of the planing general frame necessary to place the planing force in the correct direction.

Planing Frame and Force/Moment Direction

The planing force is determined using lookup tables. These lookup tables were generated by experiments done in the longitudinal plane. Thus the planing frame must be rotated such that each planing situation matches the conditions for planing in the experiment. For this purpose a general planing frame (denoted by subscript p) is defined which initially matches the body axis *b-frame*. Depending on the location of planing, this axis is rotated to match the experimental lookup table conditions. Expressed in the general planing frame, the planing force lift always maps to a force in the negative z_p direction and the drag force maps to the negative x_p direction. The the transformation matrix from the body frame to the planing frame can be determined from Equation (A.4). Among the three rotation angles, the only non-zero angle would be the rotation about the x_b axis and is denoted by the angle Φ. The determination of angle Φ is shown in Figure A.18. The position of the cavity center expressed in the body frame is determined from the delayed cavity position vector $\bar{r}_{b\to cp}(t-\tau_p)$ and was determined in Equation (A.24).

$$[x_c, y_c, z_c]^T = \bar{r}_{b\to cp}(t-\tau_p)$$

Knowing the position of the cavity center, the angle η between the y_b axis and the cavity center point (y_c, z_c) can be determined using the four-quadrant inverse tangent. The rotation angle Φ is determined by adding 90^o to η. The angle Φ rotates the planing axes such that the z_p axis is in line with the $x_p - z_p$ plane in which planing is occurring, as shown in Equations (A.31) and (A.32) respectively. Thus the planing lift contribution which maps to the negative z_p direction will create a restoring planing force pushing the vehicle back into the center of the cavity.

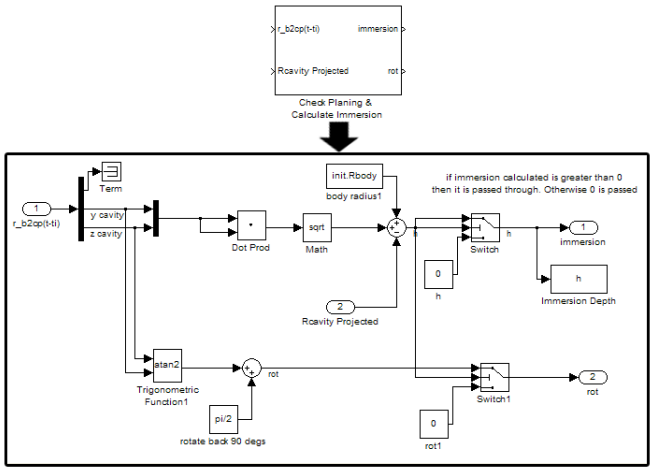

Figure A.19: Simulink implementation determining the planing immersion and the frame rotation angle which is used to determine the DCM for the planing frame

$$\eta = atan2\left(\frac{z_c}{y_c}\right) \tag{A.31}$$

$$\phi = \eta + \frac{\pi}{2} \tag{A.32}$$

The planing forces are therefore applied in the correct direction regardless of the location of planing on the body, .

Simulink Implementation: Planing Immersion and Frame Rotation

The planing immersion calculation and the rotation angle necessary to put the planing frame in the correct orientation were implemented into Simulink and saved as a library block named `Planing_Immersion.mdl`, as shown in Figure A.19.

A.6 Planing Component

The above planing details build the framework to implement the planing forces and moments as a general component.

A.6.1 Simulink Implementation: Planing Component

The planing implementation of the general component is shown in Figure A.20. The planing rotation angle determined in Equation (A.32) is used to determine the direction cosine matrix (the second and third two rotation angles are zero). Notice that non-dimensional immersion $\frac{h}{D_{body}}$ is necessary as the hydrodynamic lookup tables for planing depend on this parameter. The other noticeable change is that $\bar{r}_{b\to g}$ is determined using a lookup table since the center of pressure of planing varies with α_{cb} and $\frac{h}{D_{body}}$. This is accounted for by placing the general frame at the *cp* and then defining $\bar{r}_{g\to cp} = [0\,0\,0]^T$.

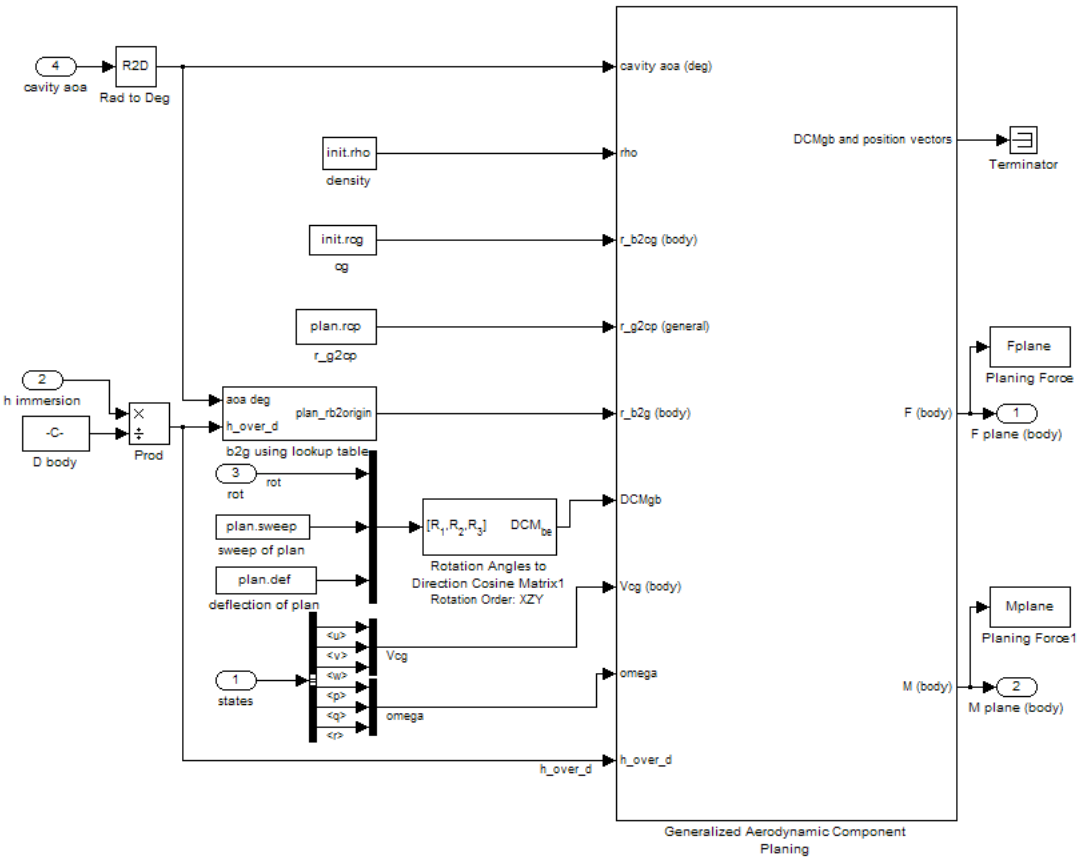

Figure A.20: Simulink implementation of planing component block.

Bibliography

[1] David R. Stinebring, Robert B. Cook, John E. Dzielski, and Robert F. Kunz. High-speed supercavitating vehicles. In *AIAA Guidance, Navigation, and Control Conference and Exhibit*, AIAA 2006-6441, August 2006.

[2] Robert T. Knapp, James W. Daily, and Frederick G. Hammitt. *Cavitation.* Institute of Hydraulic Research, 1979.

[3] Balint Vanek. *Control Methods for High-Speed Supercavitating Vehicles.* PhD thesis, University of Minnesota, 2008.

[4] Ivan N. Kirschner, David C. Kring, Ann W. Stokes, Neal E. Fine, and James S. Uhlman. Control strategies for supercavitating vehicles. *Journal of Vibration and Control*, 8:219, 2002.

[5] Albert May. Water entry and cavity-running behavior of missiles. Technical Report SEAHAC/TR 75-2, Naval Sea Systems Command, 1975.

[6] Taras Kiceniuk. An experimental study of the hydrodynamic forces acting on a family of cavity-producing conical bodies of revolution inclined to the flow. Technical Report Report N. E-12.17, California Institute of Technology Hydrodynamics Laboratory, June 1954.

[7] G. Logvinovich. *Hydrodynamics of Free-Boundary Flows.* NASA translation NASA-TT-F-658, U.S. Department of Commerce, Washington, D.C., 1972.

[8] G. Logvinovich. Some problems in planing surfaces. *Translated from: Nekotoryye voprosy glissirovaniya i kavitatsii [Some Problems in Planing and Cavitation]*, Trudy TsAGI, No. 2052, 1980.

[9] E. Paryshev. The plane problem of immersion of an expanding cylinder through a cylindrical free surface of variable radius. *International Summer School on High Speed Hydrodynamics*, Cheboksary, Russia, 2002.

[10] Robert L. Waid and Robert W. Kermeen. Forces on cylinders planing on flat and curved surfaces in cavitating and noncavitating flow. Technical Report Report N. E-73.5, Hydrodynamics Laboratory, California Institute of Technology, 1957.

[11] R. L. Waid. Water tunnel investigation of two-dimensional cavities. Technical Report Report No. E-73.6, California Institute of Technology Hydrodynamics Laboratory, 1957.

[12] R. L. Waid. Cavity shapes for circular disks at angles of attack. Technical Report Report No. E-73.4, California Institute of Technology Hydrodynamics Laboratory, 1957.

[13] Ivan N. Kirschner, Ryan E. Chamberlin, and Sevag H. Arzoumanian. A simple approach to estimating three-dimensional supercavitating flow fields. Number CAV2009 - Paper No. 145, Ann Arbor, Michigan, USA, August 2009. Proceedings of the 7th International Symposium on Cavitation.

[14] John H. Blakelock. *Automatic Control of Aircraft and Missiles.* Wiley-Interscience, 2nd edition, 1991.

[15] Robert Kuklinski, Albert Fredette, Charles Henoch, and John Castano. Experimental studies in the control of cavitating bodies. In *AIAA Guidance, Navi-*

gation, and Control Conference and Exhibit, number AIAA 2006-6443, August 2006.

[16] R. W. Kermeen. Experimental investigation of three-dimensional effects on cavitating hydrofoils. Technical Report Report No. 47-14, California Institute of Technology Hydrodynamics Laboratory, September 1960.